



Johanna Krainer, Dipl.-Ing.

**Fabrication of CMOS Integrated Gas Sensor Devices
Based on Tungsten Oxide Nanowires**

DISSERTATION

zur Erlangung des akademischen Grades
Doktorin der technischen Wissenschaften
eingereicht an der

Technischen Universität Graz

Betreuer

Assoc.-Prof. Dipl.-Ing. Dr.techn. Roland Fischer
Institut für Anorganische Chemie

und

Univ.-Doz. Mag. Dr. Anton Köck
Materials Center Leoben Forschung GmbH

Graz, Juni 2017

Eidesstattliche Erklärung

Ich erkläre an Eides statt, dass ich die vorliegende Arbeit selbstständig verfasst, andere als die angegebenen Quellen/Hilfsmittel nicht benutzt, und die den benutzten Quellen wörtlich und inhaltlich entnommenen Stellen als solche kenntlich gemacht habe. Das in TUGRAZonline hochgeladene Textdokument ist mit der vorliegenden Dissertation identisch.

Datum

Unterschrift

Abstract

The society's demands to monitor our environment encourages scientists to research and develop sensitive and reliable gas sensors. There is a great diversity of gas sensor applications reaching from large-area environmental monitoring, which could enable a global pollution mapping for a better understanding of atmospheric trends, to indoor air quality monitoring, which could be combined with ventilation systems to ensure a healthy atmosphere in offices and at home. Metal oxide gas sensors are developed to realise these applications. The detection principle of metal oxide gas sensors relies on the conductivity change of the gas sensitive material due to adsorption and desorption processes of the target gases at the materials surface. The advantage of conductometric metal oxide gas sensors over other gas sensor techniques is their simple and low-cost fabrication. Today, commercially available metal oxide gas sensors often consist of sensitive materials in form of thick films. Due to favourable material properties of nanowires, nanowire-based gas sensors are of high interest as potential next generation of gas sensor devices. In particular, the integration of nanowire materials in CMOS technology is key for the realisation of novel gas sensor devices: The nanowire material pushes the sensing performance, while CMOS fabricated microhotplates reduce the power consumption to lowest levels. Further, 3D-integration of CMOS gas sensors on microchips, containing the required circuitry, is a powerful approach for realising gas sensor systems for daily life applications.

In this thesis, CMOS based tungsten oxide nanowire gas sensors are fabricated. Therefore, tungsten oxide nanowires are synthesised by an economical and ecological hydrothermal synthesis. Subsequently, the nanowires are deposited on CMOS microhotplates by the use of an inkjet printer. The gas sensing properties of the fabricated CMOS nanowire gas sensors are characterised upon the exposure to hydrogen sulphide, carbon monoxide and carbon dioxide in humid synthetic air of different relative humidity levels. The sensors are operated in the temperature range of 250 °C to 400 °C. The obtained gas measurement results are evaluated and discussed in terms of sensor response, response and recovery times and the influencing factors like humidity and sensor operation temperature.

Acknowledgements

The presented work is conducted at the Materials Center Leoben Forschung GmbH (MCL, department Materials for Microelectronics). Financial support is acknowledged from the project "MSP - Multi Sensor Platform for Smart Building Management" (FP7-ICT-2013-10 Collaborative Project, Grant No. 611887) as well as from the project "RealNano - Industrielle Realisierung innovativer CMOS basierter Nanosensoren" (Austrian Research Promotion Agency, Grant No. 843598).

First of all, I would like to thank Anton Köck, who gave me the opportunity to work within the two above mentioned projects and to write this thesis. I would also like to thank him for his competent guidance and the dynamic and motivating work environment he created. Furthermore, I would like to thank my university supervisor Roland Fischer for fruitful discussions and the highly appreciated advices. I would also like to thank Ana Torvisco Gomez for supporting me in the writing process of this thesis.

I would like to thank my colleague Robert Wimmer-Teubenbacher for the scientific support, fruitful discussions and helpful advices. Special thanks goes to my dear colleague Eva Lackner for the stimulating but also relaxing work atmosphere as well as not just being a colleague but also a friend.

Moreover, I am very thankful to all other colleagues at the Materials for Microelectronics department at MCL for making the last three years a very enjoyable time, but especially I would like to show my gratitude to Elke Kraker, who always had motivating words ready. Furthermore, I am grateful to Marco Deluca for Raman characterisations and the competent support. I also would like to thank Katrin Fladischer, Bernhard Sartory and Walter Costin for the great support with SEM investigations.

In addition, I would like to thank Christian Gspan from the Institute for Electron Microscopy and Nanoanalysis at Graz University of Technology for TEM investigations and Birgit Kunert and Andrew Jones from the Institute of Solid State Chemistry at Graz University of Technology for providing the XRD measurements. I would also like to show my gratitude to Thomas Maier, Jörg Schotter, Stephan Steinhauer and Giorgio C. Mutinati from Austrian Institute of Technology for the scientific and technical support. Furthermore, I am grateful to the project partners for the good collaboration, in particular

Justyna Bekacz and Anneliese Pönniger from EVGroup for the inkjet printing process, Karl Rohrer, Martin Sagmeister and Ewald Wachmann from ams AG for the support regarding CMOS technology and Katharina Poulsen, Öznur Tokmak and Jan Niehaus from CAN GmbH for the collaborative synthesis of nanoparticle functionalised nanowires.

Finally, I am especially grateful to my family, my partner Christian and my friends, who constantly supported me throughout my university education.

Contents

Abstract	iii
Acknowledgements	iv
1. Introduction	1
2. Conductometric metal oxide gas sensors	4
2.1. Fundamentals of conductometric metal oxide gas sensors	4
2.2. Types of conductometric metal oxide gas sensors	7
2.2.1. Thick film metal oxide gas sensors	7
2.2.2. Thin film metal oxide gas sensors	8
2.2.3. Multi nanowire based metal oxide gas sensors	10
2.2.4. Single nanowire based metal oxide gas sensors	11
3. Tungsten oxide and its nanostructures	12
3.1. Material properties	12
3.2. Methods of tungsten oxide nanostructure growth	14
3.2.1. Vapour phase growth	15
3.2.2. Liquid phase growth	16
3.3. Applications apart from chemical gas sensing	19
4. Growth & characterisation of tungsten oxide nanowires	21
4.1. Nanowire growth	21
4.1.1. Motivation	21
4.1.2. Hydrothermal synthesis of tungsten oxide nanowires	21
4.2. Nanowire characterisation	24
4.2.1. Scanning electron microscopy (SEM)	24
4.2.2. Transmission electron microscopy (TEM)	25
4.2.3. Selected area diffraction (SAED)	27
4.2.4. Energy dispersive X-ray spectroscopy (EDX)	29
4.2.5. Raman spectroscopy	31
4.2.6. X-ray diffraction (XRD)	36

4.3. Discussion	37
5. Fabrication of nanowire gas sensors	41
5.1. Sensor types	41
5.1.1. Silicon based sensor	41
5.1.2. CMOS based sensors	41
5.2. Deposition methods & nanowire placement	48
5.3. Fabrication process	51
5.3.1. Sensor assembly of silicon based sensor	52
5.3.2. Sensor assembly of CMOS based sensors	54
5.3.3. Design of electrode structure	57
5.4. Discussion	59
5.4.1. Nanowire morphology change during sensor annealing	59
5.4.2. In situ Raman measurement of sensor annealing process	61
6. Characterisation of gas sensing properties	64
6.1. Gas reaction mechanisms	64
6.1.1. Oxygen O ₂ and humidity H ₂ O	64
6.1.2. Hydrogen sulphide H ₂ S	66
6.1.3. Carbon monoxide CO	67
6.1.4. Carbon dioxide CO ₂	68
6.2. Equipment & methods	69
6.2.1. Gas measurement setup	69
6.2.2. Measurement procedure	71
6.2.3. Data analysis	73
6.3. Gas measurement results	74
6.3.1. Description of nanowire gas sensors	74
6.3.2. Sensor response to H ₂ S	75
6.3.3. Sensor response to CO	84
6.3.4. Sensor response to CO ₂	90
6.3.5. Sensor response in nitrogen atmosphere	92

6.4. Discussion	97
6.4.1. Influence of sensor operation temperature	97
6.4.2. Influence of humidity	98
6.4.3. Influence of target gas concentration	99
6.4.4. Influence of background gas	102
6.5. Summary	103
7. Conclusion & Outlook	105
List of Abbreviations	109
Bibliography	111
List of Figures	129
List of Tables	133
Appendix	134
List of Publications	139
Curriculum Vitae	141

1. Introduction

The continuously increasing demand to monitor and control our environment intensively promotes the research on gas sensor devices. Therefore, the research on gas sensitive materials like metal oxide semiconductors and the thereof made gas sensors gains importance. The integration of these highly sensitive gas sensors into smart phones, watches, fitness bands or even smart rings also plays a great role and would open new markets. Miniaturised gas sensor systems could enable large-area urban pollution monitoring for better understanding of atmospheric trends to make advances in exposure evaluation for general population. The installation of toxic gas alarm systems in every household could prevent domestic accidents caused by carbon monoxide poisoning. The control of air conditioning systems in building complexes by carbon dioxide gas sensors could save around 40 % of required energy. All these applications are just examples of how the realisation of reliable, low-cost gas sensors could respond to society's demands. Gas sensor technology works with many different types of devices: Optical sensors, acoustic wave sensors, field effect transistors, electrochemical sensors, conductometric sensors and many more. The great interest in conductometric sensors like metal oxide gas sensors is caused by their high sensitivity to a broad range of different toxic and harmful gases and their often simple designs and low production costs. The detection principle of metal oxide gas sensors is based on a straightforward electrical measurement, where changes in the electrical conductivity of the material are monitored while gas exposure. The changes in electrical resistance are caused by adsorption and desorption processes of gas molecules at the metal oxide surface at elevated temperatures, usually between 200 °C and 400 °C. Typical commercial metal oxide gas sensors are often bulky devices based on thick films with a high power consumption, which are more applicable in industrial processes than in consumer market applications. Therefore, a great interest emerged in combining metal oxide materials with the so called complementary metal oxide semiconductor (CMOS) technology. The development of CMOS compatible gas sensors could pave the way for the realisation of the above mentioned applications. The continuously advancing demands on gas sensors and their performance shifts the focus on metal oxide nanostructures. Metal oxide nanostructures appear in many

different shapes - nanorods, nanotubes, nanowires or nanoparticles - which all show a high potential for the realisation of miniaturised high-performance devices. Metal oxide nanowires attracted a lot of attention and have been intensively investigated over the last decades with high expectations to usher in a new era of gas sensor devices. Metal oxide nanowire gas sensors entail different advantages: It is assumed that nanowires can provide a higher sensitivity than other structural forms like thin or thick films. This higher sensitivity may result from the effect of their large surface-to-volume ratio where already low gas levels have an influence on the electrical resistance of the nanowires. Metal oxide nanowires also provide good chemical and thermal stabilities under different operating conditions. The combination of metal oxide nanowires benefits and those of CMOS technology could lead to the desired high-performance gas sensor devices. However, no viable and cost-efficient metal oxide nanowire gas sensor could be successfully implemented in CMOS technology devices so far.

The objective of this thesis is the realisation of CMOS compatible metal oxide nanowire gas sensors, in particular gas sensors based on tungsten oxide nanowires. The technological challenges which arise by the integration of tungsten oxide nanowires in CMOS devices are discussed and a feasible, CMOS compatible integration is presented.

Among the variety of target gases three gas species are chosen to be focused on in this thesis: hydrogen sulphide (H_2S), carbon monoxide (CO) and carbon dioxide (CO_2). H_2S emerges in industrial areas, while CO and CO_2 are gases which can affect daily life. H_2S is a highly toxic and malodorous gas and its detection is of interest mainly in industrial environments. H_2S is used as a reaction gas in various technical areas or can be a by-product in several processes such as oil refining, natural gas manufacturing or fuel cells. It is also present in power generation systems like biogas plants, where maintenance work involves a potential risk for workers. The MAC (Maximum Allowable Concentration) value, which is the maximum permissible concentration of exposure for employees based on an eight hour time per day, maximum 40 hours per week, where no health effects are expected, is 5 ppm for H_2S [1]. In applications like fuel cells, it would be desirable to detect lowest concentrations of H_2S in the range of parts per billion (ppb) to prevent the fuel cell from poisoning [2]. In contrast to H_2S , CO is an odourless gas, but it is not less hazardous. It is hazardous and toxic because it binds to haemoglobin

and inhibits the oxygen transport in the blood, which can be fatal in a short time. The MAC value for CO is determined to 30 parts per million (ppm) [1]. Compared to CO, CO₂ is present in ambient atmosphere. Every year the growing CO₂ level in the earth's atmosphere is observed with unease. Where in 2012 the CO₂ level was at 393 ppm, beneath the 400 ppm limit, we already exceed this limit at the beginning of 2016 [3]. The detection of CO₂ levels will become more and more required in order to protect your own health, especially in large cities with high pollution levels.

This thesis is structured as follows:

- Chapter 2 gives a theoretical background of conductometric metal oxide gas sensors. Fundamental mechanisms and the types of metal oxide gas sensors are discussed, giving an insight into the different morphologies of metal oxide materials as gas sensors.
- Chapter 3 focuses on tungsten oxide. The material properties of tungsten oxide and various synthesis methods are presented with the possible application fields besides gas sensors.
- Chapter 4 provides the information about the synthesis of tungsten oxide nanowires used as gas sensor material in this work. The characterisation of the synthesised nanowire network is performed by different characterisation methods.
- Chapter 5 describes the two sensor types, silicon based (SB) and CMOS sensor, and their fabrication processes including inkjet printing as the used nanowire deposition method.
- Chapter 6 gives a summary of the sensor performance of the SB and CMOS tungsten oxide nanowire gas sensors for the selected target gases H₂S, CO and CO₂.
- Chapter 7 concludes the results obtained in this work and gives an outlook.

2. Conductometric metal oxide gas sensors

2.1. Fundamentals of conductometric metal oxide gas sensors

In 1962, Seiyama et al. [4] published the first work reporting on a metal oxide material, in this case a zinc oxide thin film, used as gas sensor because of the change in electrical conductivity caused by interactions with present gas species. The electrical conductivity of a metal oxide can be elucidated by the band theory. Metal oxides are semiconductors, where the valence band and the conduction band are separated by a band gap (see figure 2.1), typically in the range of 0.5 to 5 eV [5]. This band gap can be overcome when energy levels are above the Fermi level, so that electrons can reach the conduction band. The result is an increase of conductivity.

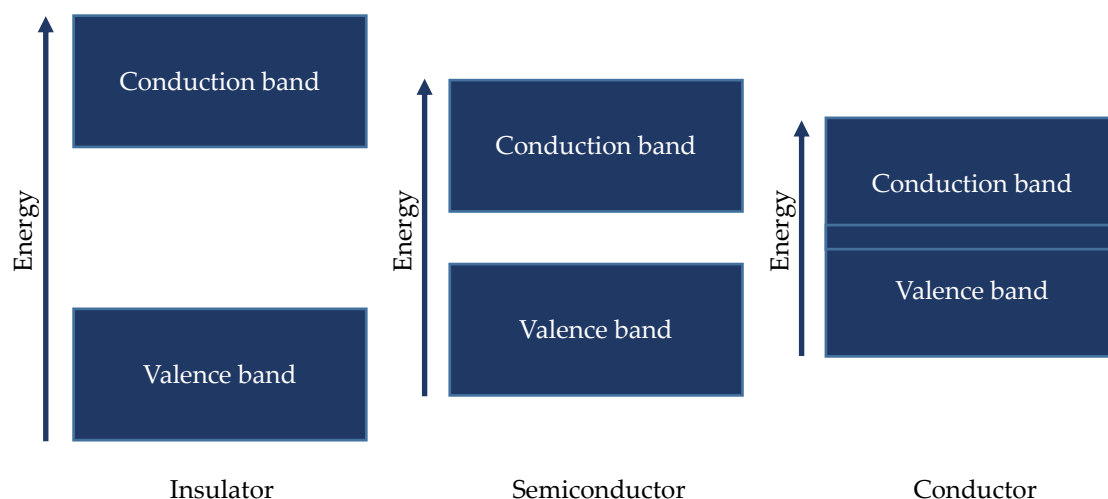


Figure 2.1.: Band model of insulator, semiconductor and conductor.

Metal oxides conductivity has been intensively studied over decades [6–9]. Metal oxides are classified into two types of semiconductor materials: n-type and p-type materials. N-type materials have a higher electron than hole (positive charge carrier) concentration, whereby in n-type materials the charge carrier transport is mainly done by electrons. P-type materials have a higher hole than electron concentration, thus in p-type materials

Table 2.1.: Examples for n-type and p-type metal oxide materials [10].

Conduction type	Metal oxide material
n-type	SnO ₂ , WO ₃ , ZnO, TiO ₂ , ZrO ₂ , In ₂ O ₃ , Fe ₂ O ₃ , La ₂ O ₃
p-type	CuO, NiO, Cr ₂ O ₃ , Co ₃ O ₄

holes are the major charge carrier. Some examples of n-type and p-type metal oxide semiconductors are given in table 2.1. The gas sensing mechanism of a conductometric gas sensor is based on the surface reactions, the consequential charge transfer processes and the transport of the charge carriers through the sensing material. According to literature, various models exist but the most common one is the ionosorption model, where oxygen species adsorbed at the metal oxide surface play a major role. Ambient oxygen molecules adsorb to the metal oxide surface and trap electrons from the conduction band, which induces a negative charged surface. The electron flow from the conduction band to the adsorbed layer of oxygen molecules forms a space charge layer between the bulk material and the surface of the metal oxide, called depletion layer. The width of the depletion layer can be evaluated by the Debye length [11]. The Debye length is influenced by material properties and sensor operation temperature, which is expressed in the equation 2.1 by temperature T , the relative permittivity ϵ_r and the density of the charge carriers N :

$$L_D = \sqrt{\frac{kT\epsilon_r\epsilon_0}{q^2N}} \quad (2.1)$$

By the formation of the space charge layer, the energy bands bend upwards. The band bending effect promotes the adsorption of oxygen species until a steady state is reached [12]. In n-type materials the charge carriers of the conduction band and the electron transport from the bulk to the surface are reduced. In p-type materials captured electrons from the valence band lead to accumulation of charge carriers (see figure 2.2). The adsorbed oxygen occurs in molecular (O_2^-) and atomic (O^- , O^{2-}) form. Up to around 200 °C, the molecular form O_2^- is dominating because of the lower activation energy. Above 200 °C, the atomic forms O^- and O^{2-} are mainly present [12]. Charge transfer and

transport processes are very influenced by the geometry and the structure of the metal oxide [13], which will be discussed in section 2.2 for each type of conductometric metal oxide gas sensor.

The gas sensing mechanism [13] itself relies on the interaction of the present gas species with the oxygen species adsorbed at the metal oxide surface, mainly with the more reactive atomic forms, O^- and O^{2-} , than with the molecular ions O_2^- (explained in detail for each target gas in chapter 6). This interaction results in a change of charge carrier density and influences the band bending, which causes a change in the material's conductivity. In the case of an n-type material and a reducing gas present, the conductivity increases because of the increase in electron density, whereas the interaction of an n-type material with an oxidising gas causes a decrease in conductivity. A p-type material shows the opposite effects, where an oxidising gas increases the concentration of positive charge carriers (holes) and a reducing gas decreases conductivity, because of the reduction of positive charge carrier concentration by the brought in negative charge.

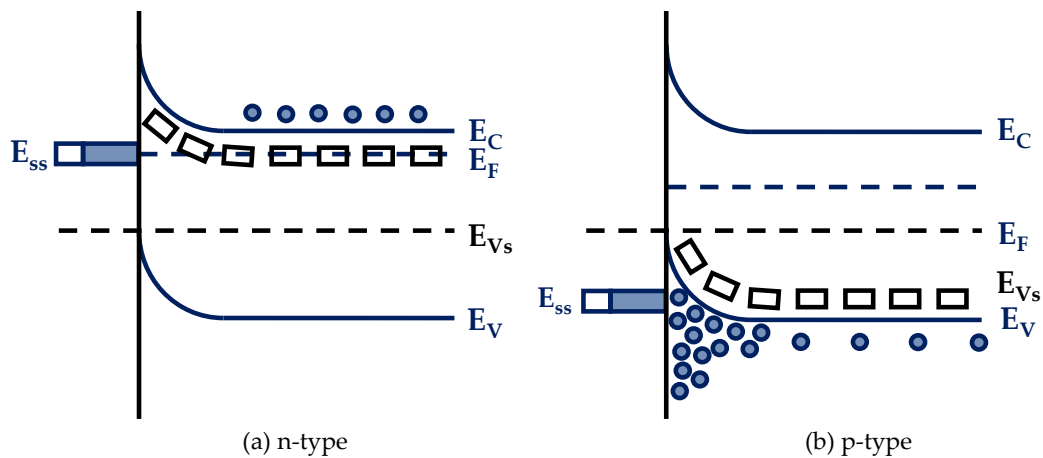


Figure 2.2.: Energy bands of n-type and p-type semiconducting metal oxides [14].

2.2. Types of conductometric metal oxide gas sensors

Conductometric metal oxide gas sensors take advantage of the conductivity change while gas molecules react with the oxygen adsorbed at the metal oxide surface. This conductivity change is read out by a simple electrical measurement: A constant current is applied to the sensing material and the voltage is measured. The resistance is presented as a measurement signal, which is calculated from current and voltage by Ohm's law.

A metal oxide gas sensor normally consists of the following parts [13]:

- Gas sensitive metal oxide material
- Electrode system (appropriate electrodes to ensure a good electrical contact of the sensor material with the electrical circuit)
- Substrate (often silicon based isolating substrate)
- Heater (Interactions between the gas species and the metal oxide material occur at elevated temperatures, usually between 200 °C and 400 °C)

The electrical properties, thus also the gas sensing properties of the conductive metal oxide material, strongly depend on the fabrication process and the consequential morphology of the metal oxide material [13]. Even for the identical surface reactions with certain gas molecules, the change in sensor resistance can be different for metal oxide materials with different morphologies [15].

In the next sections, the focus will be on the different types of conductive metal oxide gas sensors, where also differences and influences in the material morphology will be discussed.

2.2.1. Thick film metal oxide gas sensors

Thick film metal oxide gas sensors are based on a sensitive layer with a thickness in the micrometre range. Thick films are porous films and consist of grains with a certain grain size adjacent to one another. In thick films, the conduction mechanism typically follows the grain boundary controlled mechanism, which means that the free charge carriers

(electrons) have to overcome the energy barriers at the interfaces of the grains, at the interface of the metal contact and the metal oxide and the metal oxide grains themselves, as shown in figure 2.3 [13].

Thick film gas sensors are usually fabricated by screen printing of a viscous paste on alumina substrates, which provide electrodes and a heater. The metal oxide material is mixed with organic additives to achieve the required viscosity and after the thick film is printed, the sensor is dried at around 200 °C and fired between 650 °C and 850 °C to obtain the desired structural and electrical properties [16]. The disadvantage of this thick film metal oxide gas sensors is the often high power consumption (0.5–1 W) [17]. To reduce the power consumption, special fabrication methods can be used to deposit thick films on micro-machined substrates [18].

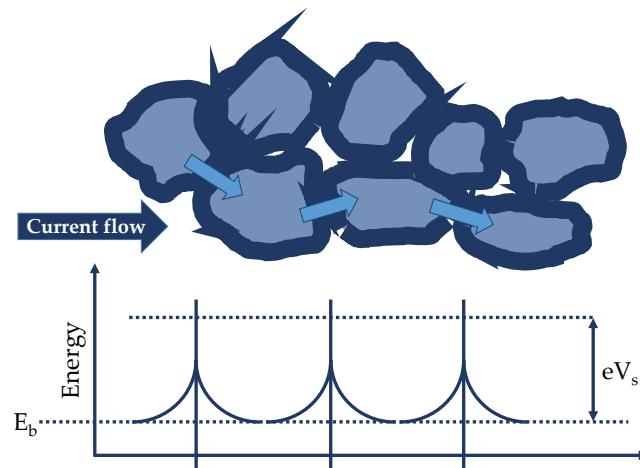


Figure 2.3.: Schematic of conduction mechanism in a porous metal oxide thick film gas sensor. Adapted from [18].

2.2.2. Thin film metal oxide gas sensors

Conductometric metal oxide thin films are promising materials for gas sensor applications [19,20]. Due to their small dimensions, low power consumption and the compatibility with many microelectronic processes, thin films are in common use. Metal oxide thin film gas sensors usually have a film thickness in the range of 50–500 nm with a compact film structure. In contrast to thick films, typical conduction mechanisms in thin films are

surface controlled as shown in figure 2.4. The fabrication of thin films can be classified into two main deposition techniques: vapour and liquid phase based. Typical vapour phase techniques include well-known deposition methods like atomic layer deposition (ALD), chemical vapour deposition (CVD) and physical vapour deposition (PVD), which further includes evaporation, sputtering and molecular beam epitaxy (MBE). The most common liquid based techniques are represented mostly by electrochemical deposition, self-assembled monolayers (SAM) and Langmuir-Blodgett fabricated films [21].

In the last years our research group gained expertise in the deposition of tin oxide (SnO_2) thin films by spray pyrolysis, which is used as gas sensitive material [15, 22–25]. Spray pyrolysis of SnO_2 layers with nanometre thickness, is already known since the middle of the 20th century [26]. Since the first report of spray pyrolysis [27] a lot of different materials have been developed to be deposited for a variety of applications [28, 29]. Spray pyrolysis of metal oxide thin films does not require expensive equipment or high temperatures (100 °C to 700 °C), therefore, it is a good alternative to the cost intensive and complex techniques mentioned before.

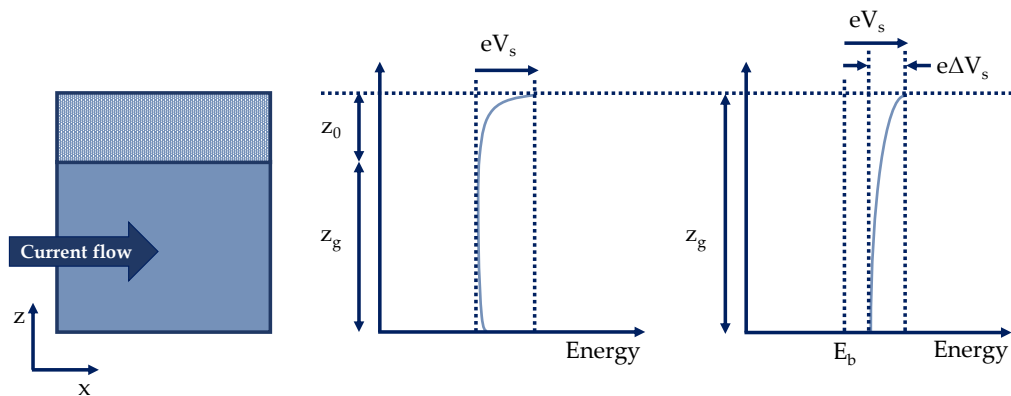


Figure 2.4.: Schematic of conduction mechanism in a compact thin film metal oxide gas sensor. Adapted from [18].

2.2.3. Multi nanowire based metal oxide gas sensors

Gas sensors of multiple metal oxide nanowires consist of controlled or randomly oriented nanowires, which form a conductive network. Nanowires are usually single crystalline, thus no grain boundaries are present along the individual nanowires [30]. The conduction takes place over the nanowire network, where electrons have to overcome the energy barriers at the interfaces of the adjacent nanowires like in metal oxide thick films, where micro- or nanoparticles are linked (see figure 2.5) [31]. More specifically, several energy barriers are present: at the interface of the metal contact and the nanowire network, at the nanowire interfaces and at the nanowires themselves [30].

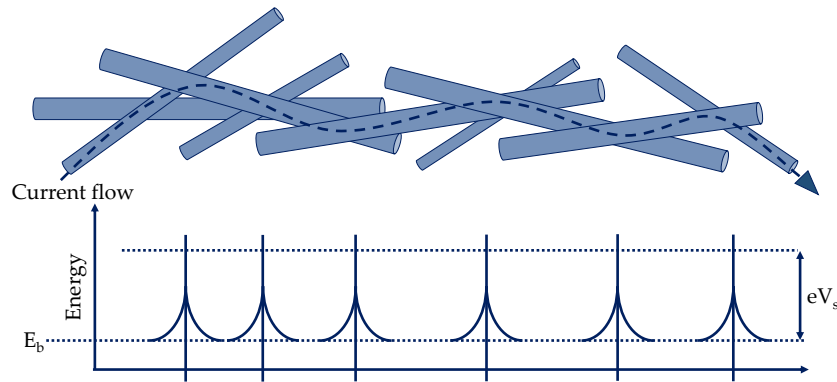


Figure 2.5.: Schematic of conduction mechanism in multi nanowire metal oxide gas sensor. Adapted from [31].

Nanowires in general can be synthesised in many ways. The synthesis techniques can be classified into bottom-up and top-down approaches [32] : Bottom-up techniques can be described as additive procedures, where nanowires are assembled by their molecular building blocks. These techniques feature high crystallinity and purity of the produced metal oxide nanowires and low equipment costs. The main disadvantage of bottom-up techniques is the challenge of controlled integration of the metal oxide nanowires onto devices. Top-down techniques are based on standard micro fabrication processes, like optical, e-beam or ion-beam lithography, where processes like etching are used to pattern larger areas of a metal oxide material in a subtractive manner. The main advantage over

bottom-up techniques is the full compatibility with semiconductor processes, but the used technological equipment entails high costs and long fabrication times. Some of the synthesis techniques will be discussed in detail for tungsten oxide nanowires in section 4.1.

The synthesised nanowires are mounted on the appropriate gas sensor substrate in various techniques, e.g. contact printing or alignment by dielectrophoresis. The techniques will be elucidated in the section 5.2

2.2.4. Single nanowire based metal oxide gas sensors

Single metal oxide nanowire gas sensors consist, like the name already indicates, of a single nanowire. The conduction mechanism is defined by the electrical properties of the contacted nanowire. No grain boundaries have to be considered, so the conduction channel is basically situated along the axis of the nanowire. By using a four-point contact configuration, energy barriers at the contact-nanowire interfaces can be overcome [30]. The fabrication processes of single metal oxide nanowire gas sensors are challenging and cost intensive. The most common way to realise single nanowire devices involves a bottom-up synthesis of metal oxide nanowires, where a single nanowire is then placed in the required position. This placement of the nanowire is a critical process step, because of a lack of precise techniques to realise the nanowire positioning. An often used procedure is the random deposition of nanowires on a plain substrate, where a single nanowire is selected and electrodes are individually patterned [15, 33–35]. An alternative procedure provides the use of a micromanipulator in combination with an electron microscope, which makes the exact placement feasible but extremely time consuming [36].

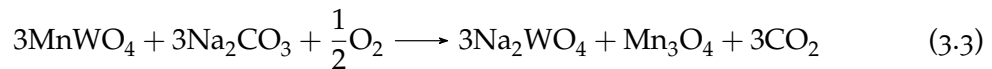
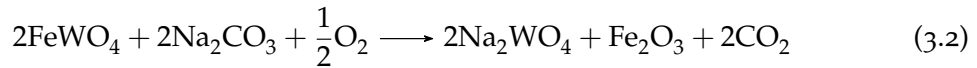
For the practical use single nanowire devices are not suitable, because of the costly fabrication process on one hand, and on the other hand because of the poor reproducibility. The synthesis of nanowires with identical geometric dimensions is not easy to realise, and therefore each single nanowire gas sensor is a unique device.

3. Tungsten oxide and its nanostructures

3.1. Material properties

Tungsten can form various oxides with oxidation states from +6 to +4. The most stable tungsten oxide is WO_3 with the oxidation number +6. Between the oxidation numbers +6 and +5 there exist several non-stoichiometric tungsten oxides ($\text{W}_{40}\text{O}_{119}$, $\text{W}_{50}\text{O}_{148}$, $\text{W}_{20}\text{O}_{58}$ and $\text{W}_{18}\text{O}_{49}$) and for the oxidation number +4, WO_2 is the known compound. No oxides with an oxidation number below +4 are noted [37].

WO_3 can be found naturally as hydrates in the minerals tungstite ($\text{WO}_3 \cdot \text{H}_2\text{O}$), hydroknoelsmoreite ($\text{WO}_3 \cdot 0.5\text{H}_2\text{O}$) and meymacite ($\text{WO}_3 \cdot 2\text{H}_2\text{O}$) [38]. It can be synthesised by various ore digestion methods. The mineral scheelite can be digested with concentrated hydrochloric acid according to 3.1. Wolframite is brought to reaction with Na_2CO_3 at about 900°C at ambient atmosphere according to 3.2 and 3.3. Na_2WO_4 can be separated, and by the addition of concentrated hydrochloric acid, tungsten(VI) oxyhydrate is precipitated and can be converted into WO_3 [37].



WO_3 is crystalline and yellow at temperatures between -40°C and 17°C . It is insoluble in water or acids, but in alkaline solutions, it dissolves under the formation of WO_4^{2-} . WO_3 crystallises in a distorted ReO_3 type (see figure 3.1), where WO_6 octahedra share corners [37]. It has a temperature dependent crystal structure: for bulk WO_3 the crystal structure appears in a monoclinic form below -40°C , triclinic from -40°C to 17°C , monoclinic from 17°C to 320°C , orthorhombic from 320°C to 720°C and tetragonal at temperatures above 720°C [40]. According to in situ Raman spectroscopy studies of tungsten oxide nanostructures [41, 42], lower temperatures are needed to induce the crystal phase transition for nanostructures as needed for bulk material, due to their enhanced surface energy. The non-stoichiometric tungsten oxides are reddish violet or

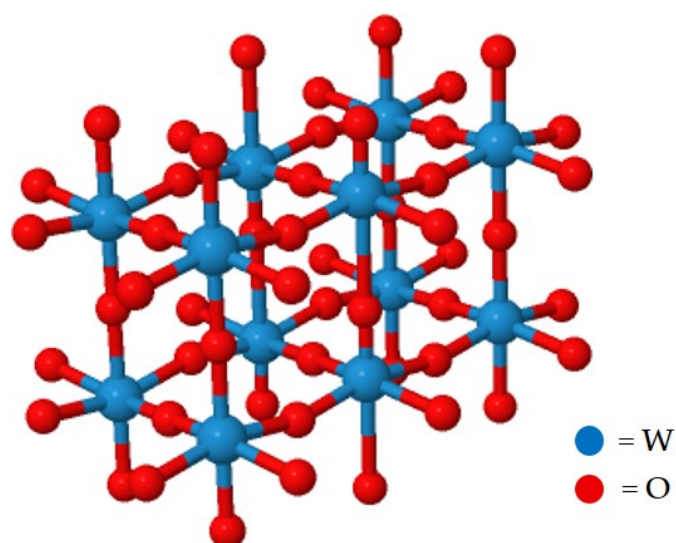


Figure 3.1.: Crystal structure of WO_3 [39].

blue coloured and have complex crystal structures, where the WO_6 octahedra not only share corners like in the WO_3 crystal but also share edges. They are so called shear structures. These shear structures result from accumulated oxygen vacancies along a certain crystal plane, which disappear when connections of edges are formed along this crystal plane. The progressive removal of oxygen vacancies leads to a series of shear structures [37]. WO_2 is a brown diamagnetic compound and crystallises in the distorted rutile TiO_2 type, where metal-metal bonds are formed due to the distortion (see figure 3.2) [37].

Pure stoichiometric WO_3 is an electrical insulator due to its wide direct electronic band gap (E_g) of 3.52 eV [43], which corresponds to the transitions between the energy levels of the valence band (2p orbitals of the oxygen) and the conduction band (5d orbitals of the tungsten) [44]. The phase transitions for bulk and nanostructured material mentioned above can also contribute to a shift of E_g , which means that WO_3 structures of different sizes have different band gaps (smaller grains lead to higher band gaps) [45].

The presence of intrinsic oxygen vacancies in the WO_3 structure increases the conductivity [40] and is responsible for the n-type semiconductor properties. With the decrease of oxygen (from WO_3 to WO_2), the tungsten oxide carries out a semiconductor-metal transition [46], where an increasing occupation of the conduction band can be observed by X-ray photoelectron spectroscopy (XPS) [47]. Thus, WO_2 is metallically conductive [37].

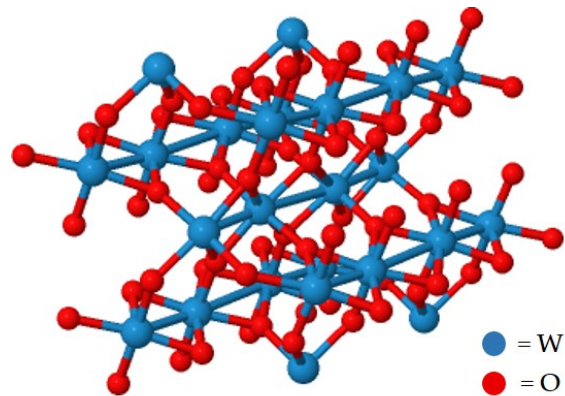


Figure 3.2.: Crystal structure of WO_2 [39].

Furthermore, tungsten oxides have remarkable optical properties. Thin films of stoichiometric WO_3 are essentially transparent to the visible wavelengths. This transmittance can be modulated, which means that the colour of WO_3 can be switched from the initial transparent state to dark blue, by a change of the electron states in the WO_3 molecule. The effect can result from an applied voltage (electrochromism), a reducing gas (gasochromism) or heat treatment (thermochromism) [48].

3.2. Methods of tungsten oxide nanostructure growth

Tungsten oxide nanostructures can be found in many different shapes: particles, sheets, wires, tubes, trees, flowers or even hollow spheres (see table 4.1). Various synthesis methods were developed to prepare tungsten oxide nanostructures, which can be divided into bottom-up and top-down methods (discussed in detail earlier in section 2.2.3). The more common types of growth are based on bottom-up techniques, which can be classified into two types according to their physical conditions: vapour and liquid phase growth. The vapour phase growth benefits from the high crystal quality of the produced nanostructures, but involves high investment costs for the required equipment. The liquid phase growth is disadvantaged by a poorer crystal quality, but the better morphology control of nanostructures and relatively low reaction temperatures compared to the vapour phase growth are more attractive [49,50].

3.2.1. Vapour phase growth

Vapour phase growth includes a wide range of different synthesis techniques, but they all have one thing in common, the evaporated source material. The energy input to evaporate the source material mainly originates from thermal treatment, electron beam, laser emission, or ion bombardment. Two mechanisms for vapour phase growth are suggested: the vapour solid (VS) and the vapour liquid solid mechanism (VLS) [50].

- The VS mechanism is proposed to be governed by the minimisation of surface free energy. The evaporation of the source material at high temperatures and the condensation of the material directly on the substrate at the low temperature region, without any catalyst present, results in seed crystals, which serve as nucleation sites and facilitate the directional growth to minimise the surface free energy [51].
- In the VLS mechanism three phases are involved: the vapour phase of the source material, the liquid catalyst droplet and the solid product. This mechanism could be confirmed in 2001 by Wu et al. [52], who reported on real-time observation of nanowire growth by an in situ high temperature transmission electron microscope. The required catalysts usually are metal particles, which can be prepared by various deposition techniques, e.g. sputtering [53–55]. The role of the catalyst is to lower the activation energy of the nucleation, which is reported in detail by [56].

The most common synthesis technique used for tungsten oxide nanostructures, which include vapour phase growth, is thermal evaporation, but sputtering is also an effective way to achieve the desired nanostructures.

Thermal evaporation

Thermal evaporation uses heat as the driving force to achieve the vaporisation of the solid source material. The process takes place either in vacuum or in a controlled gas environment at low pressure. The source material, mainly tungsten metal (W) or tungsten oxide (WO_3), is evaporated and transported by the gas stream to the substrate located at a certain distance from the heated source material, where it is condensed. By adjusting

the process parameters including evaporation temperature, gas environment or substrate temperature, the desired tungsten oxide nanostructures can be achieved. Thangala et al. [57] reported about the vapour solid growth of tungsten oxide WO_x nanowires, where the condensed WO_x vapour forms WO_x clusters on the substrate, which oxidise and form nanocrystalline seeds. Depending on the crystallinity of these WO_x seeds, the nanostructures will grow in the vertical direction forming one dimensional nanowires or in both vertical and lateral direction forming nanoparticles by using an elevated substrate temperature.

Sputtering

Sputtering is a well established technique [58], where a solid target material is ablated by the bombardment with highly energetic ions, such as Ar^+ . The process parameters can be precisely tuned, which leads to a controlled growth of the material on the substrate. In general, sputtering is used to deposit films and not one dimensional nanostructures, but these films can be used as material source for the nanostructure growth. By adjusting the parameters during the sputter process, the surface morphology of the grown nanostructures can be controlled, as shown by Chen et al. in 2006 for the synthesis of tungsten oxide nanowires [59].

3.2.2. Liquid phase growth

Liquid phase growth includes various techniques to synthesise tungsten oxide nanostructures: the most common ones are hydrothermal technique, sol-gel method, template assisted growth and electrospinning. The techniques entail relatively low temperatures compared to vapour phase based techniques, therefore the compatibility with low-temperature-tolerant substrates is given. The chemical reactions mainly involved in these techniques are hydrolysis, condensation, etching and oxidation [49].

Hydrothermal growth

Hydrothermal growth of tungsten oxide nanostructures is a well known and cost effective synthesis technique [60]. The synthesis starts with an aqueous solution of a tungsten compound, which is transferred to an autoclave and kept at elevated temperatures (between 150 °C and 400 °C) for several hours (see table 4.1). During the process, temperature and relatively high pressure conditions force the nucleation of crystallites followed by the growth, which often leads to planar two-dimensional nanostructures like sheets or flakes [61]. According to [62] the addition of structure-directing agents, like alkali salts, leads to one dimensional nanostructures like nanowires. The exact role of the added agents in the reaction mechanism is still unclear but Gu et al. [63] and Rajagopal et al. [64] suggest that ions originating from the agents adsorb onto the surface of the nucleation crystallites and hence locally decrease the surface energy and affect the growth mechanism.

Sol-gel growth

The sol-gel process consists of two main steps: the fabrication of the sol and gelation. The main precursor molecules used for the formation of the sol are tungsten alkoxides. In 1997, Lee [65] reported on a sol-gel process using a tungsten alkoxide ($W(OEt)_6$) as precursor material, which is unfortunately quite expensive. Other precursor molecules known from literature are tungsten chlorides [66,67], tungsten oxychloroalkoxides [68] or peroxotungstic acid [69]. The hydrolysis of precursor molecules results in reactive species, which condense and finally form a network of sol particles. This sol-gel can be deposited by spinning, dip- or drop-coating onto substrates, where an annealing step of the deposited material follows. The resulting film consists of tungsten oxide nanostructures [70].

Template assisted growth

The template assisted method is a modified sol-gel process, where either "hard" or "soft" templates are used. "Hard" templates, such as an anodic aluminium membrane (AAM) [71] or a porous silica substrate [72], are immersed into the tungsten precursor solution. The precursor solution infiltrates the template and is brought to gelation. The tungsten oxide gel is annealed within the template structures and afterwards the "hard" template is removed by chemical etching [73]. Most common "soft" templates are carbon-based like carbon microspheres [74] or polymer-based like polyethylene glycol (PEG) [75] or polymethyl methacrylate (PMMA) [76]. The template materials are dissolved or dispersed in solutions and added to the tungsten precursor solution. The mixture is brought to gelation and afterwards annealed in a specific environment to remove the "soft" template.

Electrospinning

Electrospinning is a technique which was originally developed for the fabrication of ultra thin polymer fibres [77,78]. Electrical forces at the surface of the precursor solution overcome the surface tension and an electrically charged jet is formed. A solid fibre is generated as the electrically charged jet is stretched by electrostatic repulsions of the surface charges and the evaporation of the solvent [51]. The precursor solution consists of a polymer like polyvinylpyrrolidone (PVP) [79,80] or polyvinyl acetate (PVAc) [81] and a tungsten compound like tungsten isopropoxide ($W(iPr)_6$) [81], tungsten hexachloride (WCl_6) [82] or metallic tungsten in combination with hydrogen peroxide [79].

3.3. Applications apart from chemical gas sensing

3.3.1. Electrochromic applications

Tungsten oxide represents a common electrochromic material and has been intensively studied over the past decades [83,84]. With its various oxidation states, it is one of the most efficient electrochromic metal oxides also due to its fast optical response time, reversible colour change and high colouration efficiency [82,85].

Electrochromic devices consist of transparent electrodes, a layer of electrochromic material and an electrolyte. When a certain voltage is applied to the system, the ions diffuse from the electrolyte into the material, where they intercalate and cause the chromic effect. Typically used electrolytes are sulphuric acid or perchloric acid to supply H^+ ions, and lithium perchlorate to supply Li^+ ions [49].

One dimensional tungsten oxide nanostructures have gained importance due to their enhanced optical and electrical properties resulting from their nanostructure [86]. Tungsten oxide nanostructures are applicable to various technical fields which benefit from their electrochromic properties. For example, smart windows use tungsten oxide nanostructures to reversibly change the optical properties of the glass depending on the environmental conditions for better building energy management [87,88]. Smart mirrors in cars prevent the driver from being blinded from other cars light by an automatically regulated glare protection [89].

3.3.2. Photocatalytic applications

Since 1969, when Fujishima and Honda [90] reported of the photoelectrolysis of water by the use of a titanium oxide catalyst, metal oxide materials, including tungsten oxide, have been studied intensively [91,92]. Tungsten oxide nanostructures are reported to have enhanced photocatalytic abilities, compared to tungsten oxide films, because of their high surface-to-volume ratio and the therefore resulting larger effective surface area [93]. Although tungsten oxide has good photocatalytic abilities, the most attractive chemical reaction of reducing water to produce hydrogen is thermodynamically unfavourable [49].

This problem can be overcome by mixing tungsten oxide with other metal oxides to form an overall complementary band structure as first reported in 2001 by Sayama et al. [94], where water was split stoichiometrically into hydrogen and oxygen by a Pt-WO₃ and Cr-Ta-doped Pt-SrTiO₃ catalyst.

4. Growth & characterisation of tungsten oxide nanowires

4.1. Nanowire growth

4.1.1. Motivation

The fabrication of tungsten oxide nanostructures is well-known and can be realised in many synthesis ways, as discussed in section 3.2. In general, a low-cost synthesis producing a high amount of nanowires is preferred, which can be easily upscaled to an industrial high-volume production. The hydrothermal growth represents such an economic method to produce nanostructures in a large yield and is therefore our choice of synthesis. The hydrothermal synthesis requires no vacuum or other expensive equipment, just the cheap educts and an autoclave as reaction vessel. Additionally, the reaction involves no toxic or environmentally harmful educts and produces no harmful products or by-products, hence the reaction can be classified as an ecofriendly synthesis.

4.1.2. Hydrothermal synthesis of tungsten oxide nanowires

The hydrothermal synthesis of tungsten oxide nanostructures can lead to many differently shaped products. Depending on the precursor material and the additives used in the synthesis, tungsten oxide nanoplates, nanobelts, nanowires or even hollow nanostructures can be produced (see table 4.1).

The tungsten oxide nanowires, used for the metal oxide gas sensor production, are synthesised by hydrothermal growth using tungstic acid as tungsten precursor and potassium sulphate as additive [95]. Tungstic acid (H_2WO_4 , 0.85 g, Sigma Aldrich, 99 % purity) is stirred in 30 ml of deionised water until a homogeneous dispersion results. Potassium sulphate (K_2SO_4 , 40 g, Sigma Aldrich, ≥ 99 % purity) is gradually added to the dispersion and stirred until a paste-like mixture is formed. The mixture is transferred to the autoclave 4744 from Parr Instruments Company [96] (figure 4.1 (left)) with a volume

of 45 ml. The autoclave is temperature treated at 180 °C for 12 h in an universal oven UNB200 from memmert GmbH + Co.KG [97]. After the reaction time, the autoclave was naturally cooled down to room temperature. The light green reaction product (figure 4.1 (right)) is washed and centrifuged several times with deionised water and ethanol to remove potassium sulphate, and subsequently dried overnight at 80 °C.

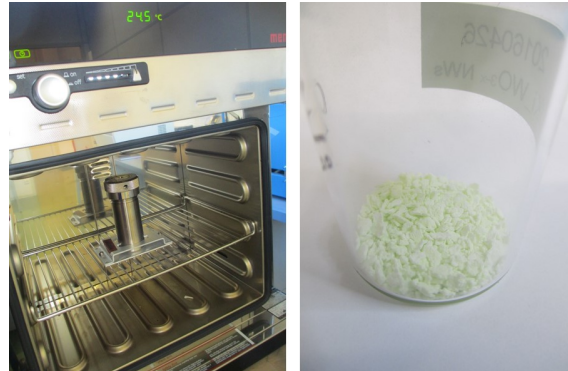
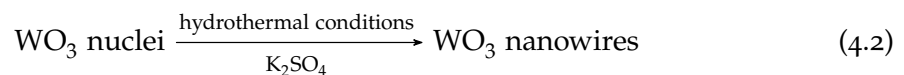
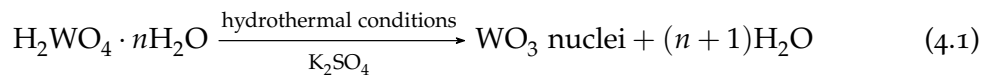


Figure 4.1.: Autoclave for hydrothermal synthesis in the used universal oven (left) and dried nanowire powder (right).

The hydrothermal synthesis is suggested to happen by the following reaction mechanism [98,99]:



When the reaction temperature exceeds the decomposition temperature of tungstic acid, tungsten oxide nuclei are formed. The potassium sulphate acts as an additive, which its effect on the formation of tungsten oxide nanostructures could not be completely clarified up to now. It is assumed that the anisotropic growth, which leads to tungsten oxide nanowires, is caused by the adsorption of ions to specific crystal surfaces, lowering the surface energy and hence suppressing the growth of these faces [99]. Depending on the involved ions, different influences on the shape and crystal structure of nanostructures are observed [64,99].

Table 4.1.: Summary of WO_x nanostructures synthesised by hydrothermal method.

Morphology	Dimensions (nm)	Precursor	Additives	Temperature (°C)	Duration	Ref.
nanowires	D: 25 – 50 L: several μm	Li ₂ WO ₄	Li ₂ SO ₄	180	12 – 48	[99]
nanobelts	L: 1000 – 3000 W: 30 – 100 D: 15	H ₂ WO ₄	CTAB	180	12	[100]
hollow spheres, hollow boxes, nanotubes	various	WCl ₆	urea	180	12	[101]
nanoplates, nanorods	nanoplates L: 500 – 1000 W: 100 – 200 nanorods D: 8 – 10 L: 50 – 200	Na ₂ WO ₄ · 2 H ₂ O	NH ₄ NO ₃ PEG	200	24	[102]
microflowers	L: 2000 – 3000 W: 100–300 H: 100–300	(NH ₄) ₆ H ₂ W ₁₂ O ₄₀ · xH ₂ O	CTAB	200	24	[103]

4.2. Nanowire characterisation

4.2.1. Scanning electron microscopy (SEM)

The reaction product of the hydrothermal synthesis is characterised by SEM using a Zeiss Supra 40, at Austrian Institute of Technology (AIT). In figures 4.2 and 4.3, two SEM images are shown, where a dense network of nanowires can be identified. A nanowire length of 1–10 μm can be estimated. More precise geometric information will be given by transmission electron microscopy (TEM) characterisation.

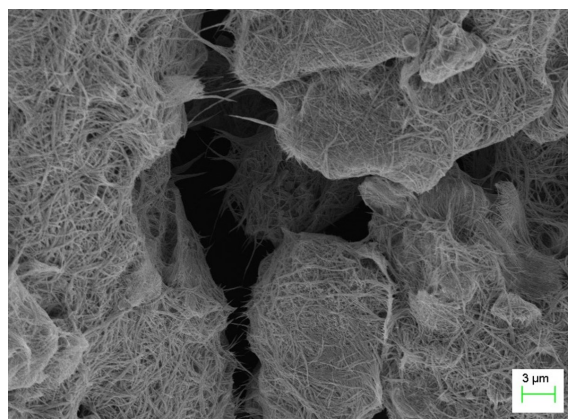


Figure 4.2.: SEM image of tungsten oxide nanowires.

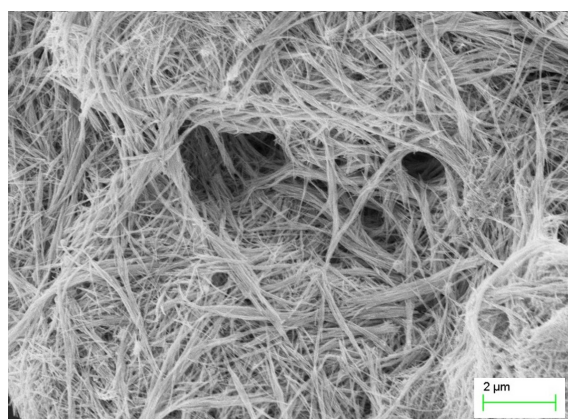


Figure 4.3.: SEM image of tungsten oxide nanowires (higher magnification).

4.2.2. Transmission electron microscopy (TEM)

The synthesised nanowires are characterised by TEM using a FEI Tecnai F20 (figure 4.4) and a FEI Titan³ G2 60 – 300 for higher resolution images (figure 4.5), at the Institute for Electron Microscopy and Nanoanalysis, Graz University of Technology. The tungsten oxide nanowire network powder is dispersed in propan-2-ol and subsequently dropped on a TEM grid made of copper. The solvent is evaporated for one hour before the TEM characterisation is started.

Figure 4.4 shows a TEM image, which confirms the dense nanowire network already observed at the SEM characterisation. The TEM image in figure 4.5 displays a magnification, where a single tungsten oxide nanowire with a diameter around 20 nm can be seen. The average nanowire diameter in the tungsten oxide nanowire network is between 10 and 30 nm. Due to this nanowire diameters and the length of 1–10 μm , high aspect ratios up to 1000 can be achieved. The single nanowire in figure 4.5 shows a crystalline structure, but seems to have a fibrous texture in the growth direction of the nanowire. The material surrounding the nanowire results from the deposition of carbon inside the electron microscope when focusing the electron beam on the nanowire.

The inset in figure 4.5 shows the fast Fourier transformation (FFT). From the FFT a lattice plane constant of 4.1 \AA can be determined, in growth direction of the nanowire.

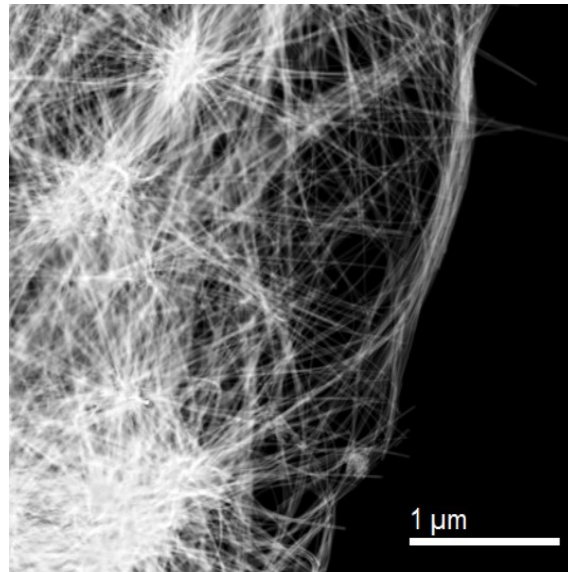


Figure 4.4.: TEM image of tungsten oxide nanowires.

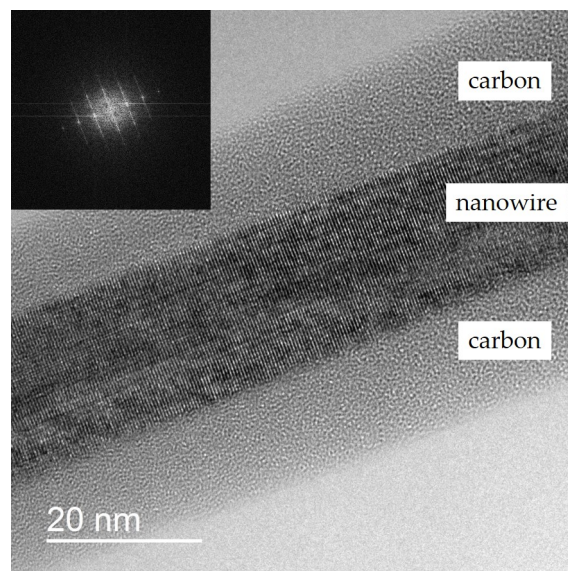


Figure 4.5.: High resolution TEM image of an individual tungsten oxide nanowire (surrounded by carbon due to electron beam induced deposition) with FFT in the inset.

4.2.3. Selected area diffraction (SAED)

The SAED pattern shown in figure 4.6 is taken by a TEM FEI Tecnai F20 at the Institute for Electron Microscopy and Nanoanalysis, Graz University of Technology. Depending on the crystal structure of the tungsten oxide nanowires the electrons of the electron beam in the TEM are diffracted at the present atoms and scattered to specific angles. The SAED is taken of several nanowires in the dense nanowire network, showing the same result. The SAED pattern is representing multiple nanowires, therefore the pattern appears in ring shape, but consists of single reflexes of single crystal nanowires (figure 4.5). The reflection distances in reciprocal space are determined by the resulting peak profile shown in figure 4.7 (in detail in section A in the appendix). The distances in reciprocal space are transformed to direct space (table 4.2) and lead to characteristic spacing values (in nm).

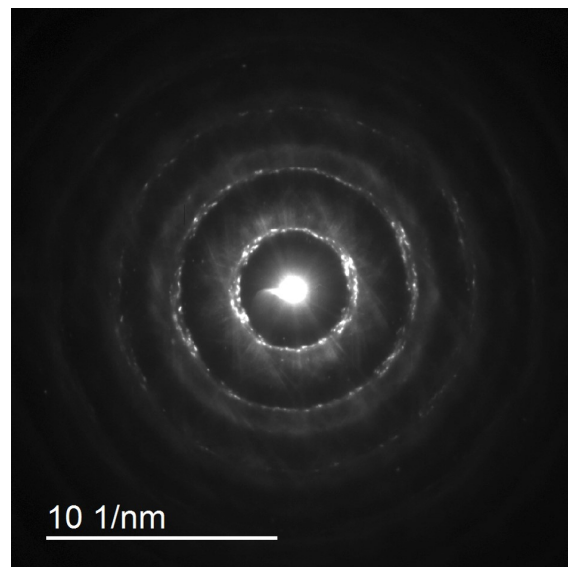


Figure 4.6.: Selected area diffraction (SAED) pattern.

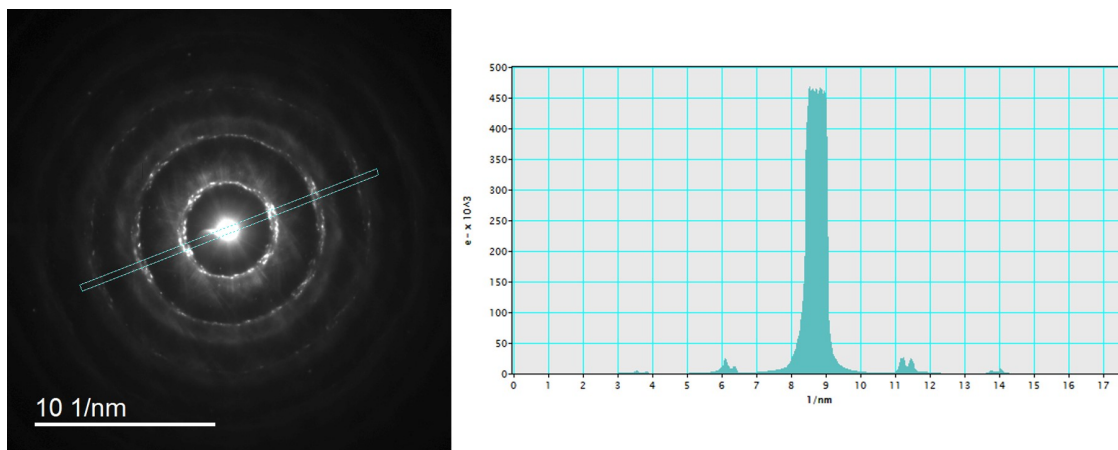


Figure 4.7.: SAED pattern (left) with peak profile of reflections (right).

Table 4.2.: Evaluation of SAED pattern.

Distances in reciprocal space (nm^{-1})	Distances in direct space (nm)
2.469 (figure A.2)	0.4050223
2.757 (figure A.3)	0.3627131
5.058 (figure A.4)	0.1977066
5.321 (figure A.5)	0.1879346
7.598 (figure A.6)	0.1316136
7.838 (figure A.7)	0.1275836

4.2.4. Energy dispersive X-ray spectroscopy (EDX)

The EDX spectrum in figure 4.8 is examined by FEI ChemiSTEM technology with Super-X detector (from Bruker) in the TEM FEI Titan³ G2 60 – 300 at the Institute for Electron Microscopy and Nanoanalysis, Graz University of Technology. The measurement is performed at several different nanowires showing the same result. The spectrum proves the chemical composition of tungsten (W) and oxygen (O) of the tungsten oxide nanowires but also potassium (K) is present. Tungsten shows the M line at 1.774 keV and the L α line at 8.396 keV, oxygen is represented by the K α line at 0.525 keV and potassium by the K α line at 3.312 keV. The peaks at 0.930 keV and 8.040 keV result from the TEM grid made of copper. The remaining smaller peaks at 1.383 keV, 7.388 keV, 8.724 keV, 9.672 keV, 9.960 keV and 11.286 keV are all related to tungsten lines.

An approximated calculation of the materials composition (shown in table 4.3) indicates a certain amount of potassium but no sulphur can be found in the EDX spectrum, so residual potassium sulphate (used in the nanowire synthesis) can be excluded as cause of the potassium peak. Potassium sulphate is very sensitive to the electron beam [104], so that the sulphur peak could disappear while taking the EDX measurement because of evaporation of the sulphate. Therefore the EDX spectrum is also analysed in the very first seconds of the measurement, but no sulphur can be detected, which would show its K α at 2.307 keV.

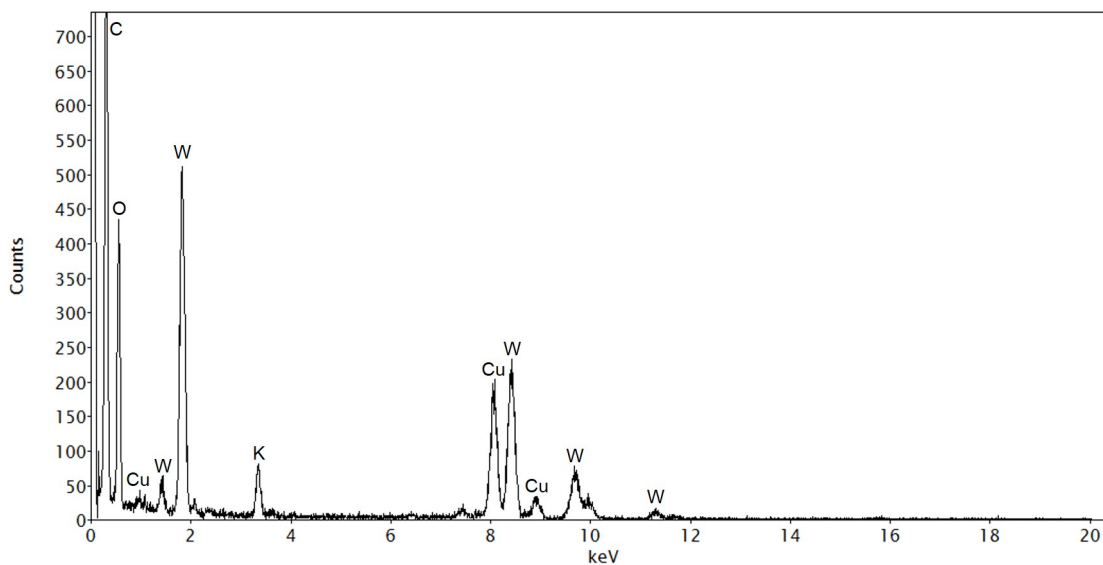


Figure 4.8.: EDX spectrum of tungsten oxide nanowires.

Table 4.3.: Composition of tungsten oxide nanowires - approximated calculation of atomic percentage of oxygen (O), potassium (K) and tungsten (W).

Element	Shell	Signal (Counts)	Composition (Atomic %)	k-factor	Det.Corr.
O	K	5772.1 ± 3.0	67.2	1.1	0.99
K	K	1729.8 ± 4.1	7.8	1.0	1.0
W	L	$1.3e^4 \pm 8.1$	25.0	2.1	1.0

4.2.5. Raman spectroscopy

The tungsten oxide nanowires are investigated by Raman spectroscopy at room temperature using a Horiba Jobin Yvon, LabRAM HR800 with two different laser types: a green Ar laser (514.5 nm) with a laser power up to 2.54 mW and a red He-Ne laser (633 nm) up to 8.63 mW. First of all the as synthesised nanowires are investigated at 0.02 mW using the green laser (see figure 4.9) The spectrum shows three characteristic features. The broad feature at 200–380 cm^{-1} results from O-W-O bending modes in the WO_6 octahedra, which are associated to long O-W-O bonds and the broad feature at 620–860 cm^{-1} refers to O-W-O stretching modes of shorter bonds in the WO_6 octahedra [105, 106]. The broad appearance of these modes could be explained by disorder in crystal structure (broad dispersion of crystal sizes) [105]. The band at 930 cm^{-1} results from vibrations of terminal WO_2 units [106] and the band at 960 cm^{-1} from vibrations of terminal oxygen atoms [41, 107], which is often associated to nanocrystalline structures [105] or could also be caused by symmetric stretching mode of this terminal bond related to hydrated WO_3 [108]. By increasing the laser power of the green laser up to 2.54 mW, and therefore also increasing the temperature in the nanowire material induced by the laser power, the broad bands become sharper and the band of vibrations of terminal oxygen atoms at 960 cm^{-1} disappears (figure 4.10). The spectrum which appears closely resembles the spectrum of WO_3 [109]. In figure 4.11 Raman spectra with increasing laser power are shown. For this investigation, the red laser is used due to a higher range of laser power up to 8.63 mW. At 0.07 mW a Raman spectrum of broad peaks appears. With increasing laser power bands, which could be related to WO_3 , as already discussed above, appear until it finally shows sharp peaks at the laser power of 8.63 mW. To verify the irreversibility of the change in the Raman spectrum of the nanowires, a Raman spectrum is recorded at low laser power of 0.07 mW after the high laser power of 8.63 mW (figure 4.12).

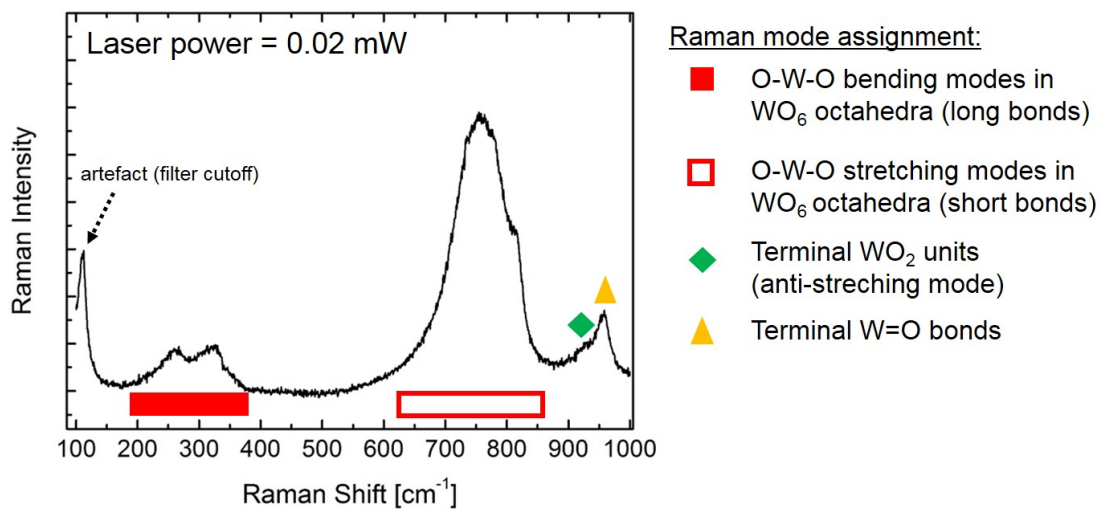


Figure 4.9.: Raman spectra of tungsten oxide nanowires (laser: 514.5 nm Ar; green).

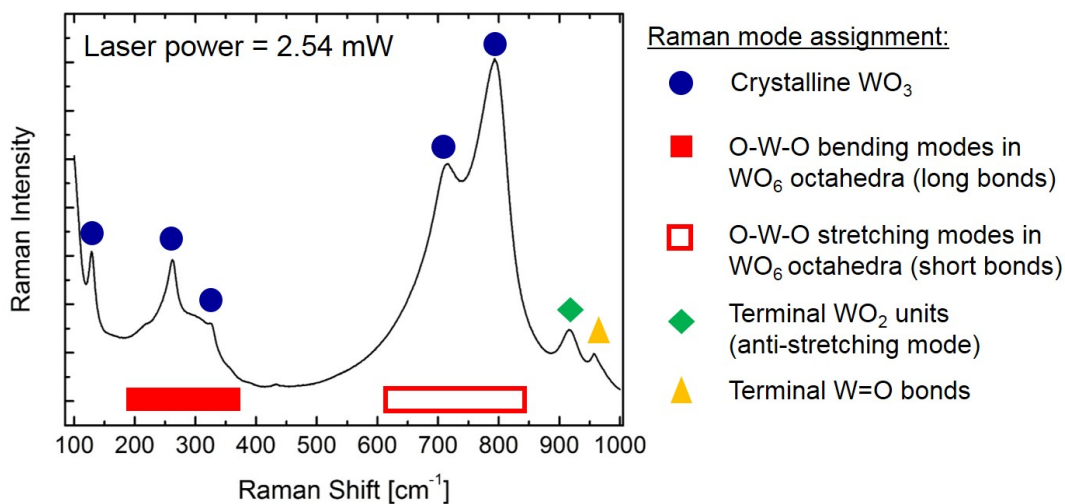


Figure 4.10.: Raman spectra of tungsten oxide nanowires with increased laser power (laser: 514.5 nm Ar; green).

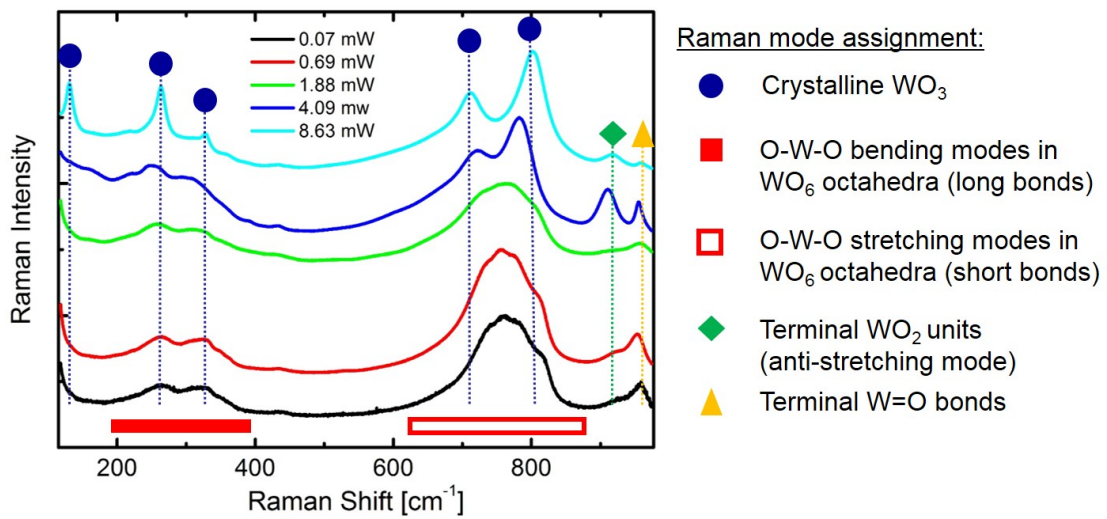


Figure 4.11.: Raman spectra of tungsten oxide nanowires with increasing laser power (laser: 633 nm He-Ne; red).

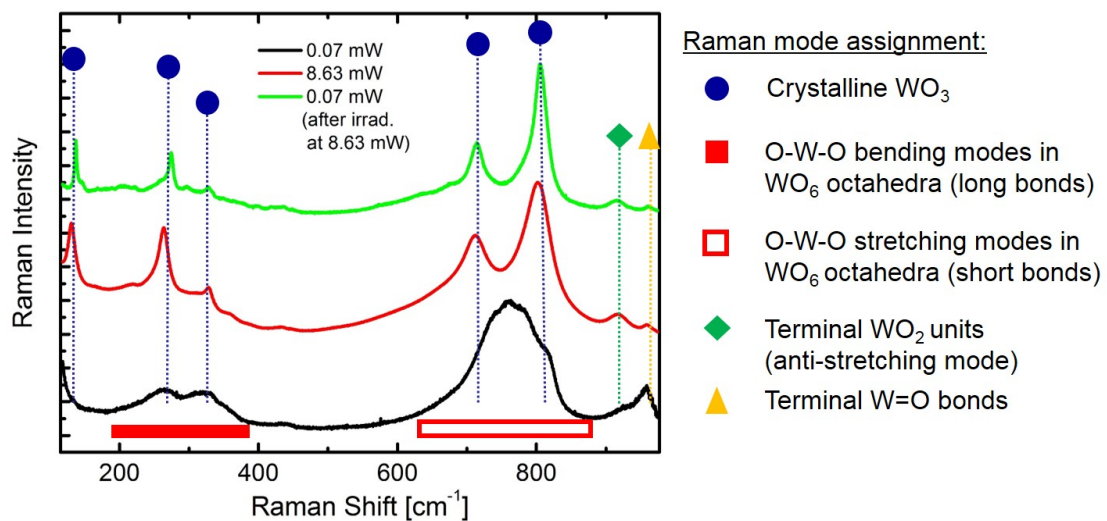


Figure 4.12.: Raman spectra of tungsten oxide nanowires with alternating laser power (0.07 mW / 8.63 mW / 0.07 mW)(laser: 633 nm He-Ne; red).

To investigate the influence of laser induced heating effects, the nanowires are treated at 400 °C in a tube furnace for 12 h in ambient atmosphere and characterised by Raman spectroscopy (figure 4.13) at a laser power of 0.07 mW. The same observations as in figure 4.11 and 4.12 can be made. The annealed tungsten oxide nanowires show more defined peaks. SEM images of the two nanowire samples, not annealed and annealed at 400 °C, are presented in the figures 4.14 and 4.15. The annealed nanowires are larger in size and changed morphology compared to the not annealed nanowires.

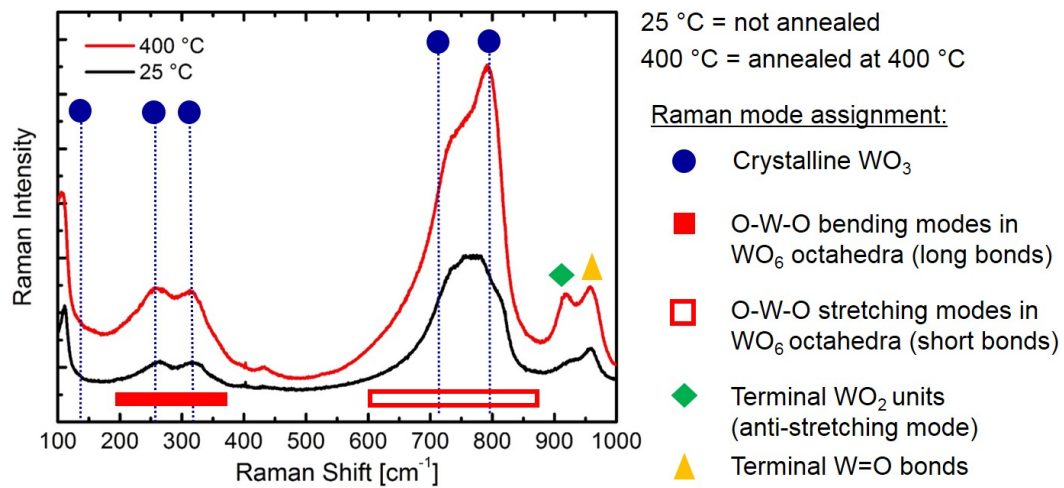


Figure 4.13.: Raman spectra of tungsten oxide nanowires after thermal treatment of 400 °C for 12 h.

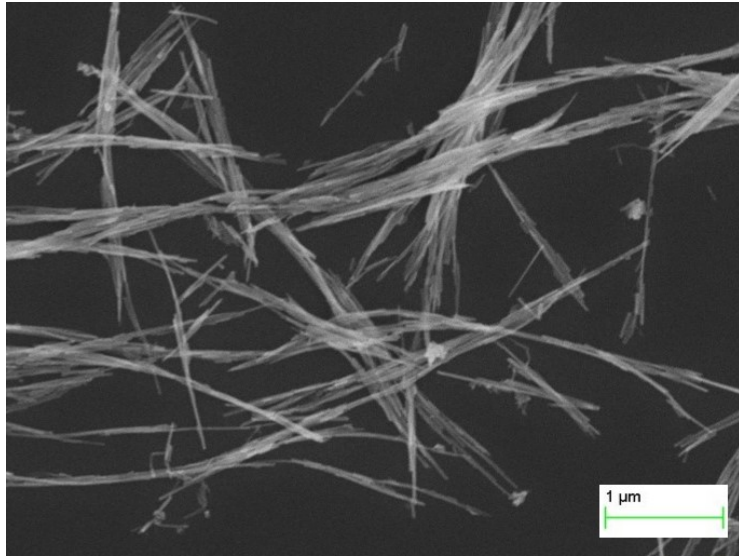


Figure 4.14.: SEM image of tungsten oxide nanowires without temperature treatment.

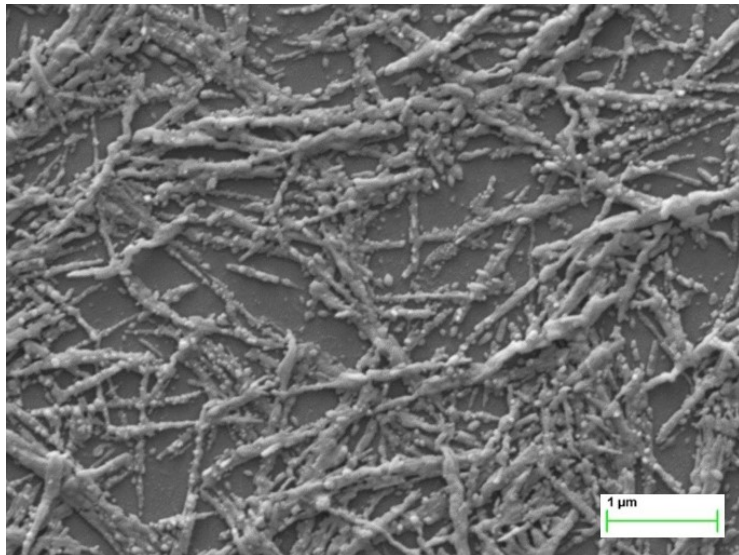


Figure 4.15.: SEM image of annealed tungsten oxide nanowires.

4.2.6. X-ray diffraction (XRD)

The tungsten oxide nanowires are investigated by powder X-ray diffraction using a PANalytical EMPYREAN diffractometer with Cu K_{α} radiation ($\lambda = 1.54 \text{ \AA}$) in a flat plate setup at the Institute of Solid State Physics, Graz University of Technology. On the primary side, a 1/8 divergence slit and a 0.02 rad Soller slit are used. On the secondary side, an anti-scatter slit and 0.02 rad Soller slit are used with a PANalytical PIXcel^{3D} detector to record the diffracted intensities. The measurement is performed at room temperature.

Figure 4.16 shows the XRD spectrum with a sharp and intense peak at $2\theta=23.2^{\circ}$ and a lot of less intense broad peaks. The peak positions are in best agreement with hexagonal WO_3 from [110], identified by the ICSD database [111] (see appendix figure B.1). This would indicate a space group of $P6_3/mcm$ with the cell parameters $a=b=7.3244 \text{ \AA}$ and $c=7.6628 \text{ \AA}$.

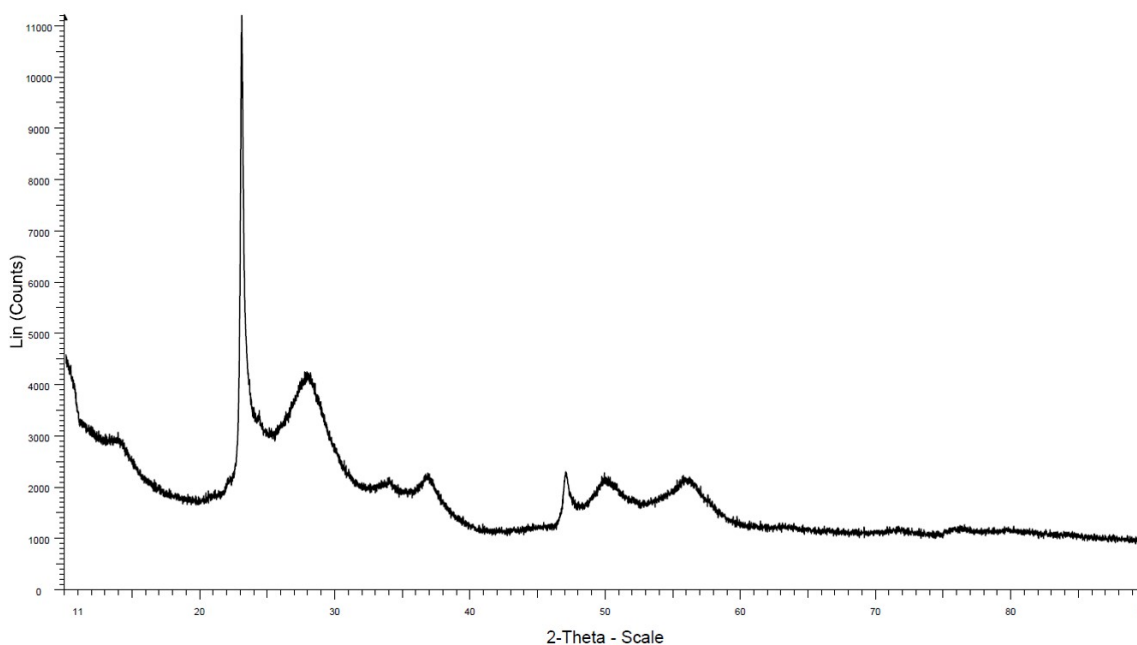


Figure 4.16.: XRD spectrum of tungsten oxide nanowires.

4.3. Discussion

The different characterisation methods provide a lot of information about the tungsten oxide nanowires, which is discussed in the following sections:

TEM

In the HR-TEM image in figure 4.5 the nanowire shows a fibrous structure in growth direction of the nanowire. The fibrous appearance of the nanowire could be explained by an effect like crystal twinning along the growth direction of the nanowire.

The FFT, obtained from HR-TEM image, shows a lattice plane constant of 4.1 Å in the growth direction of the nanowire (inset in figure 4.5). The lattice plane constant for WO_3 is defined as 3.8 Å, whereas the constant for WO_{3-x} is larger, e.g. 4.2 Å for $\text{W}_{18}\text{O}_{49}$ [111]. According to the lattice plane constant the nanowire consists of non-stoichiometric tungsten oxide.

EDX

The EDX analysis shows a certain amount of potassium in the tungsten oxide nanowires, which could lead to the assumption, that potassium cations are incorporated into the crystal lattice. Tungsten oxides are well known to form tunnels with a rather large diameter, where alkali metals can be located [112, 113]. The alkali metal ions can be stabilised either by the tungsten atoms present in 6+ and 5+ state [114] or by excess oxygen atoms [113, 115]. With respect to table 4.3, a rough estimation can be made for a material compositions like $\text{K}_{0.3}\text{WO}_3$ or rather $\text{K}_{0.3}\text{WO}_{3+x/2}$.

XRD

The XRD investigation identifies the nanowire network as hexagonal tungsten oxide WO_3 [110] with lattice parameters of $a=b=7.324 \text{ \AA}$ and $c=7.662 \text{ \AA}$. The sharp peak at $2\theta=23.2^\circ$ indicates a preferential growth in (001) direction. The layers of corner-sharing WO_6 octahedra are stacked along this direction and form hexagonal tunnels [110,112]. Kudo et al. [115] reports on a potassium intercalated hexagonal tungsten oxide compound with almost same cell parameters ($a=b=7.31 \text{ \AA}$ and $c=7.65 \text{ \AA}$) like Oi et al. [110] for hexagonal WO_3 without alkali metal intercalation. Guo et al. [113] reports on the reduction of $\text{K}_x\text{WO}_{3-x/2}$ to K_xWO_3 , where an intermediate of $x < 0.33$ shows a XRD spectrum, matching with the result in this work. According to these references, the nanowire network has a tungsten oxide framework, with a possible potassium intercalation or even potassium being part of the lattice. When the interpretation of XRD is done, it has to be taken in account, that this characterisation technique is a bulk analysis.

SAED

The evaluation of the SAED pattern (table 4.2) shows specific lattice distances, which can be compared to database values of tungsten oxides (with and without taking potassium into account) [111]. Most lattice distances can be roughly assigned to WO_3 as well as WO_{3-x} . Also the database values of the hexagonal WO_3 with intercalated potassium cations are in high agreement with the determined values of this work [115]. But the high value of 0.4050223 nm is the crucial reason, which rather indicates a non-stoichiometric tungsten oxide.

Raman spectroscopy

The Raman spectra in figure 4.11 show the tungsten oxide nanowire network from initial state to a laser induced heated state. The induced temperature causes an irreversible change in the material, as proven by the spectra in figure 4.12.

The peak evolution by increasing the laser power can be interpreted in different ways:

1. The initial state is representing hydrated WO_3 nanowires, which undergo a dehydration process, when temperature increases at higher laser power or rather when the nanowire material is annealed at high temperatures [108].
2. The initial state is representing non-stoichiometric WO_{3-x} nanowires, which become oxidised at ambient air due to the induced temperature change [116].
3. The initial nanowires (no matter which stoichiometry is present) grow in crystal size with the increasing temperature [41].

Focusing on the peak at 960 cm^{-1} , which represents terminal $\text{W}=\text{O}$ bonds, it is decreasing with increasing laser power. As already mentioned above, this peak can be an indication for a nanocrystalline structure with high surface-to-volume ratio [105], but also for crystal water incorporated in the material structure. This peak can not be found in the non-stoichiometric reference [116], where the oxidation of non-stoichiometric to stoichiometric tungsten oxide nanowires is reported, but Liu et al. reported on $\text{WO}_{2.72}$ nanowires, where an intense peak at 960 cm^{-1} appears in the Raman spectrum [117]. Therefore, a clear identification of the nanowire stoichiometry can not be given by Raman spectroscopy. The most probable explanation for the evolution of the Raman spectra is the crystal growth, where nano crystals gain size, which is indicated by the splitting of the broad band at around 800 cm^{-1} and the disappearance of the band at 960 cm^{-1} [41].

Conclusion of nanowire characterisation

The composition of the present nanowire network can be interpreted by comparing the different results. First of all, the probability of hydrated WO_3 nanowires being mainly present in the nanowire network is disproved by the XRD spectrum. If there would be hydrated WO_3 present, an intense peak at $2\theta=18^\circ$ would have to be part of the peak profile. The HR-TEM with a lattice plane constant of 4.1 \AA and the evaluation of the SAED pattern indicates a non-stoichiometric tungsten oxide. On the other side, the XRD characterisation shows with high probability the presence of WO_3 . The analysis of Raman spectroscopy leaves room for interpretation, but the most probably explanation is a crystal growth induced by increasing the temperature in the nanowire network. Concerning

the stoichiometry of the nanowire network, Raman is not the appropriate investigation method to make a clear statement on that. An additional factor is the presence of potassium in the EDX measurement of several nanowires in the nanowire network. Usually the colour of tungsten oxides gives indication for the present stoichiometry, because pure WO_3 shows an intense yellow colouration and non-stoichiometric compounds range from violet to dark blue. The nanowire powder synthesised in this work shows a light greenish, turquoise colour, which could be an indication for a mixture of nanowires with different stoichiometry. Therefore, the coloration of the nanowire powder can not contribute significantly to the identification of the nanowire composition. In table 4.4, the indications for each suggested tungsten oxide nanowire composition are summarised.

Table 4.4.: Indications for suggested tungsten oxide nanowire compositions.

$(\text{K}_x)\text{WO}_3$	WO_{3-x}	$\text{K}_x\text{WO}_{3+x/2}$
XRD spectrum fits best to hexagonal WO_3 with a preferential growth in (001) direction	Evaluation of the HR-TEM image by FFT shows a lattice plane constant of 4.1 \AA , which matches best WO_{3-x}	EDX analysis that the nanowire network contains a certain amount of potassium
EDX shows potassium being part of the nanowire network composition, which could be intercalated without a severe influence on the lattice parameters [112]	Data evolved from SAED are in better agreement with non-stoichiometric than with stoichiometric tungsten oxide	XRD of reduced potassium tungsten oxide compound in [113] suggests that the nanowire network in this thesis consists of $x < 0.33$

The conclusion can be drawn, that by the use of the available investigation methods, no clear statement about the nanowire composition can be given. Due to the fact, that the tungsten oxide nanowire gas sensor is used at elevated sensor operation temperatures, the temperature induced morphology change, already indicated by Raman spectrometry, is investigated in more detail in section 5.4.

5. Fabrication of nanowire gas sensors

5.1. Sensor types

5.1.1. Silicon based sensor

The silicon based sensor has a simple assembly design. The used heater and temperature sensor are commercially available components and easy to handle. The substrate consists of a standard silicon wafer with 300 nm thermal silicon oxide as insulating layer. The electrode system, which is used for the resistance measurement of the sensor material, and the sensor material deposition can be realised in cleanroom facilities at Austrian Institute of Technology (AIT) and at EVGroup. The silicon based sensor is designed as an economical test sensor, where developed sensor materials can be investigated without any advanced technologies from semiconductor industry.

5.1.2. CMOS based sensors

Complementary metal oxide semiconductor (CMOS) is a technology which is used to construct integrated circuits. The "complementary" in CMOS results from the use of n-type/p-type pairs of metal oxide semiconductor field effect transistors. With this technology ams AG fabricates CMOS microhotplate chips within the projects "MSP - Multi Sensor Platform for Smart Building Management" (Grant No. 611887) and "RealNano - Industrielle Realisierung innovativer CMOS basierter Nanosensoren" (Grant No. 843598), which are used as substrates for CMOS based sensors in this work.

A standard 0.35 μm CMOS technology is used to fabricate the CMOS microhotplate chips. The CMOS microhotplates consist of a poly-silicon heater in a standard CMOS layer stack (figure 5.1), which allows us to heat up the microhotplate to 400 °C. The straightforward microhotplate design represents a suspended membrane as shown in figure 5.2, where silicon is removed beneath the CMOS stack to isolate it from the bulk silicon and prevent thermal losses. The thermal isolation of the CMOS microhotplate therefore minimizes the power consumption while heating.

In this work, a more sophisticated CMOS microhotplate design is presented. The CMOS hotplate, with an area of $72\ \mu\text{m} \times 72\ \mu\text{m}$, is connected to the rest of the silicon chip by four arms in a spider-like structure. It is isolated from the bulk silicon from below by a post process MEMS etching step, more specifically a front side XeF_2 isotropic silicon dry etching step. It is expected that this spider-like structure contributes to the lowering of power consumption due to less thermal loss compared to membrane-like microhotplate structures. Another benefit of this structure is, that the surrounding of the microhotplate stays at room temperature. The hotplate temperature can be measured by integrated thermocouples. In the progress of the projects, various microhotplate chip modifications have been developed. Two modifications are used in this work: the modifications are called MPW3mod and MPW4.

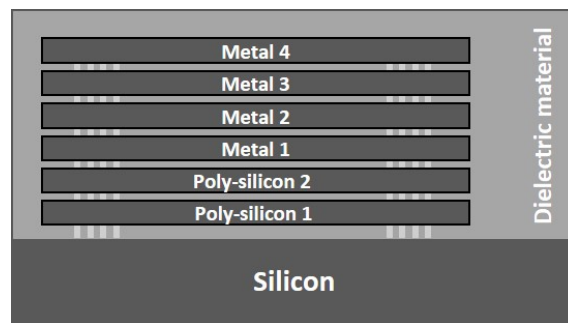


Figure 5.1.: CMOS microhotplate stack with silicon basis and multiple poly-silicon and metal layers.

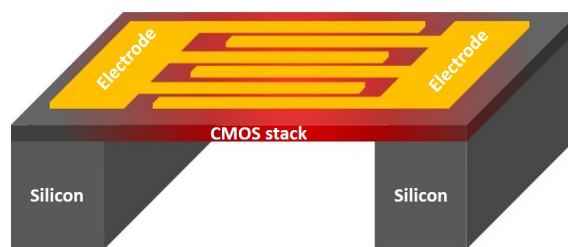


Figure 5.2.: Straightforward microhotplate with heated suspended membrane.

MPW3mod

The MPW3mod microhotplate chip consists of two microhotplates. Both microhotplates have an area of $72\ \mu\text{m} \times 72\ \mu\text{m}$, but they differ in the length of the four arms (figure 5.4). The microhotplate with the longer arms (left structure in figure 5.4) has an arm length of $147\ \mu\text{m}$ and the one with the shorter arms (right structure in figure 5.4) has an arm length of $47\ \mu\text{m}$. For the fabrication of the CMOS tungsten oxide nanowire gas sensor, the microhotplate configuration with the longer arms is used (figure 5.5). The electrical connections (bright strips shown in figures 5.6 and 5.7) are metal contacts made of tungsten, which protrude out of the microhotplate surface and contact the gas sensitive nanowire network from the CMOS side. These so-called tungsten plugs are fabricated within the CMOS process at ams AG. However, the tungsten plugs result in severe reliability issues, because of the poor thermal stability. A thermally induced oxidation of the tungsten metal even leads to a microhotplate breakage.

The resistive heater of the microhotplate consists, as mentioned above, of poly-silicon. The power-temperature profile of the heater is shown in figure 5.3 for the applied sensor operation temperatures in this work. Only $13.5\ \text{mW}$ are required to heat up the microhotplate to $400\ ^\circ\text{C}$.

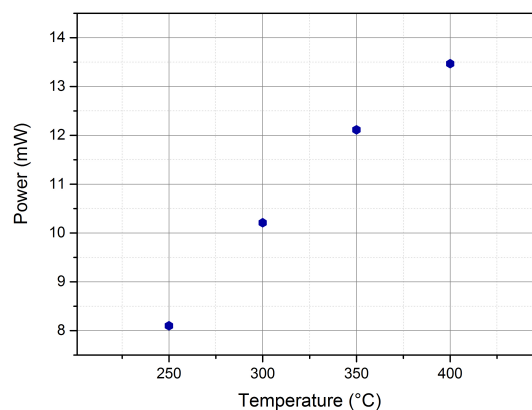


Figure 5.3.: Power consumption vs. temperature of CMOS MPW3mod microhotplate.

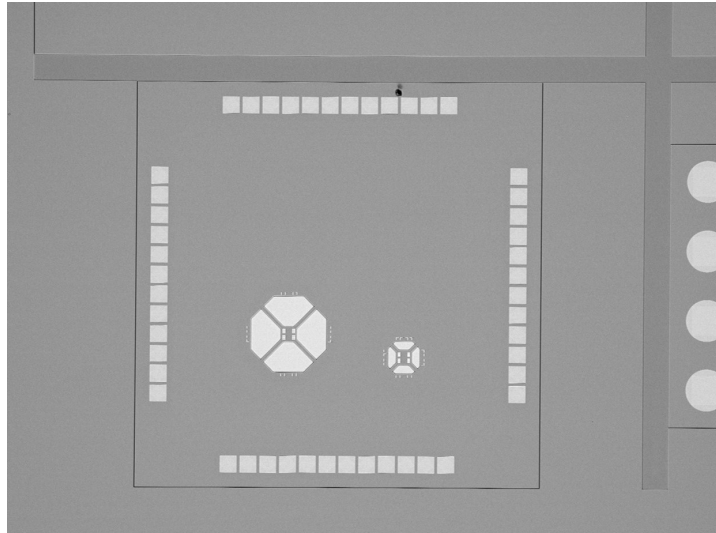


Figure 5.4.: CMOS MPW3mod microhotplate chip with two microhotplates.

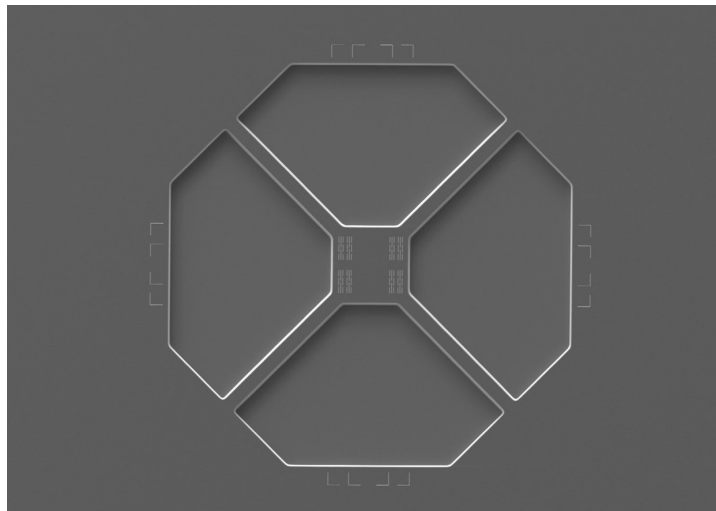


Figure 5.5.: CMOS MPW3mod microhotplate with an arm length of $147\ \mu\text{m}$.

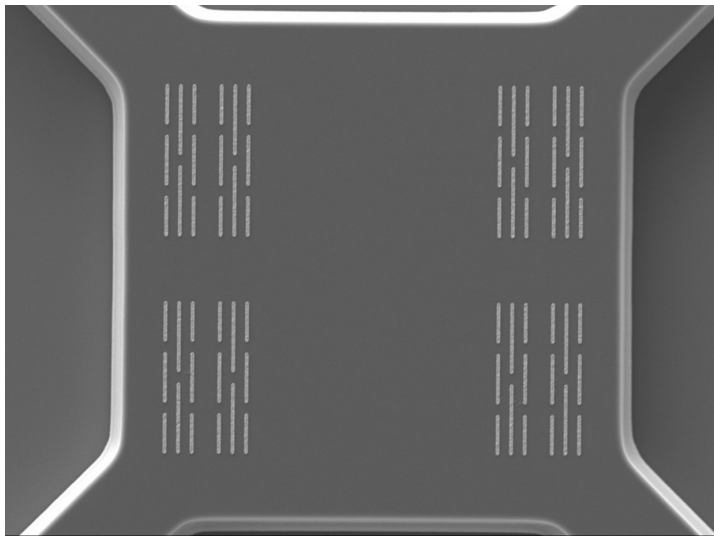


Figure 5.6.: MPW3mod CMOS microhotplate with tungsten plugs.

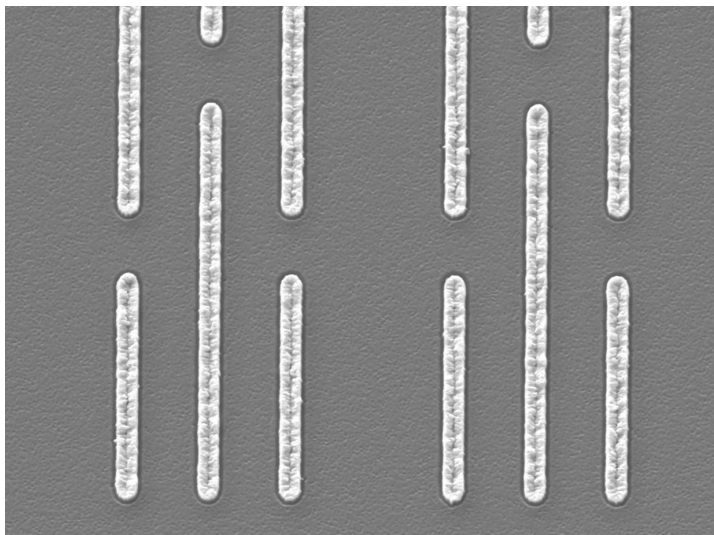


Figure 5.7.: Tungsten plugs on CMOS MPW3mod microhotplate.

MPW4

The MPW4 microhotplate chip consist of eight microhotplates of the same configuration (figure 5.9) with an area of $72\ \mu\text{m} \times 72\ \mu\text{m}$. This chip design with eight equal microhotplates emerges from the concept of a multi sensor chip, where various gas sensitive materials can be deposited on the microhotplates. This concept can lead to a single chip, which provides multiple gas sensing features. All eight microhotplates can be used to fabricate the CMOS tungsten oxide nanowire gas sensor. The electrodes (bright lines in figures 5.9 and 5.10) are patterned in a post-CMOS optical lithography step with a titanium/gold layer deposition performed by Siemens AG in Munich. The electrodes are connected to metal pads embedded in the CMOS chip, which provide electrical connections to bond pads. This chip is also combined with TSV-technology to enable 3D-integration.

The heater design is different to that of MPW3mod and therefore the heater profile slightly differs (figure 5.8).

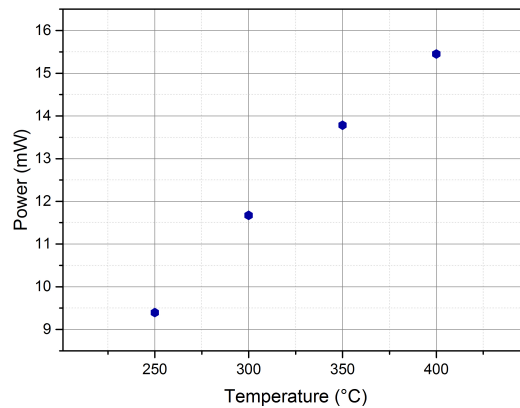


Figure 5.8.: Power consumption vs. temperature of CMOS MPW4 microhotplate.

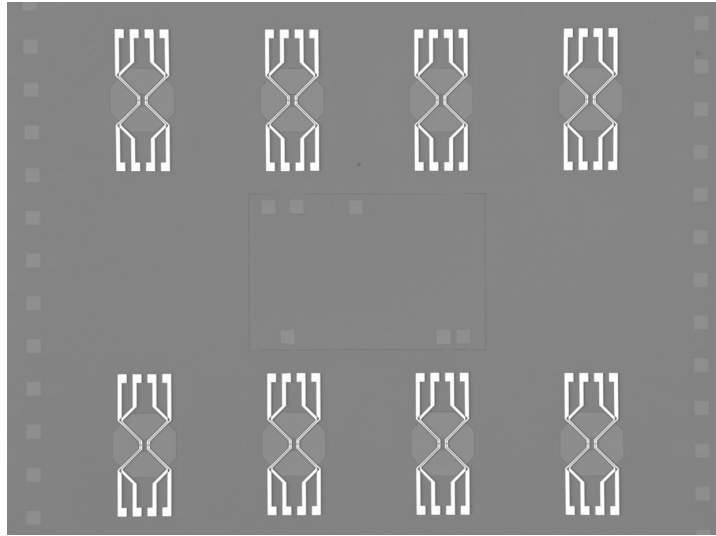


Figure 5.9.: CMOS MPW4 microhotplate chip with eight microhotplates.

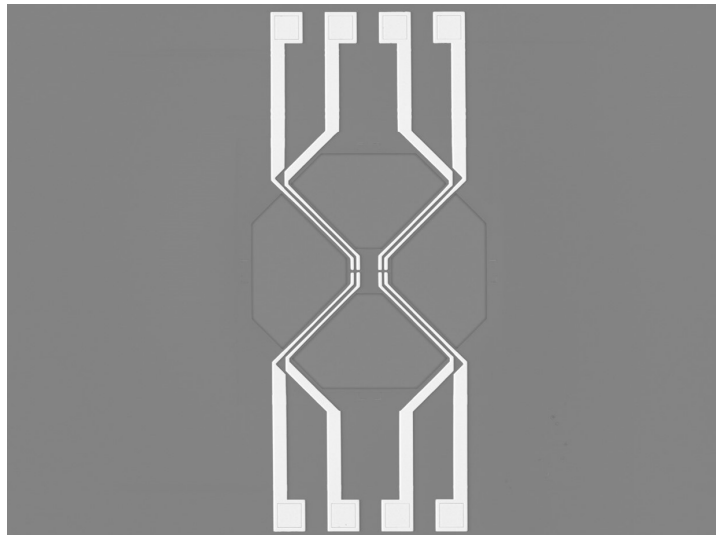


Figure 5.10.: CMOS MPW4 microhotplate with gold electrodes.

5.2. Deposition methods & nanowire placement

The transfer of nanowires on the specific position of the substrate is the crucial step in the nanowire gas sensor production. Metal oxide nanowires can be placed in the favoured substrate position by many different methods. Contact printing, Langmuir-Blodgett technique or dielectrophoresis are some of the often used placement methods [118]. In this work, inkjet printing is introduced as an unconventional but effective nanowire deposition method.

Inkjet printing

Inkjet printing allows the deposition of fluids by piezo-driven jetting [119]. The fluids can be water or solvent based, acidic or basic, but they have to have a high fluidity. A certain voltage is applied to a piezoelectric element placed in the print head of the inkjet printer, which changes the shape and generates a pressure pulse in the fluid. In this way, a droplet of the fluid (nanowire suspension) is forced through the nozzle at the print head. By a precise xyz stage and a well aligned camera system, the droplets can be placed at the required position on the substrate.

The inkjet printing has a variety of applications, from the production of light-emitting diodes (LEDs) and solar cells to printed biological and pharmaceutical devices [120].

Contact printing

Contact printing is a transfer technique where nanowires are physically removed from the donor substrate by shear forces and attached to the receiver substrate by van der Waals interactions. In practice, this means that the donor substrate, loaded with nanowires, is placed on the receiver substrate and by a directional sliding movement the nanowires are transferred to the receiver substrate and simultaneously combed, which leads to aligned nanowires [121]. The donor substrate can be the growth substrate itself or can be a transfer stamp, by which the nanowires are lifted up from their growth substrate.

The receiver substrate can be made of silicon, glass or even flexible plastic. It can be bare or can have a chemically modified surface, which leads to a higher nanowire density after the transfer process [122]. It can also be patterned to provide the aligned nanowires to particular areas on the receiver substrate, whereby after the printing transfer the patterned resist has to be removed by a common lift-off process. The transfer can take place in a dry mode or lubricants like octane and mineral oil are added, which act as a spacer between donor and receiver substrate and therefore reduce the nanowire damage during the transfer process [122].

The contact printing is a transfer technique, which can be applied to a wide range of materials like indium arsenide (InAs) [123] or germanium (Ge) nanowires [124] with the application as field effect transistors. Also the special form of contact printing called roll printing attracts attention, where the donor substrate with a cylindrical form is rolled over the receiver substrate with a certain pressure [125].

Langmuir-Blodgett

Langmuir-Blodgett technique was designed to use compression to form a layer of molecules like stearic acid on the surface of a given subphase, most commonly water, to subsequently deposit this layer on a substrate by dip-coating. To apply this technique to metal oxide nanostructures like nanowires, it is necessary that the nanowires are available in a hydrophobic state and monodispersed in an organic solvent [126–128]. Therefore, the surface of metal oxide nanowires is modified with molecules like stearic acid combined with cetyltrimethylammonium bromide (CTAB) [126], which act as surfactants. Surface modified nanowires can then be monodispersed in an highly volatile organic solvent (chloroform [126] or 2,2,4-trimethylpentane/2-propanol mixture [129]) and this solution is spread on the subphase, where the organic solvent is evaporated. During the compression process, the nanowires become aligned along their axes and form the dense nanowire layer. The substrate is dipped beneath the nanowire layer into the subphase and is withdrawn, while the surface pressure is kept constant [130]. The nanowires are transferred onto the substrate in an aligned form.

Corresponding to literature various nanostructures have already been deposited by

Langmuir-Blodgett technique, such as silicon nanowires [131], germanium nanowires [132], vanadium oxide nanowire [126] and barium chromate nanorods [133].

Dielectrophoresis

Dielectrophoresis uses an electrical field to align nanowires between electrodes. First, a suspension of the grown nanowires is prepared. Secondly, this suspension is brought into contact with the substrate by drop-coating of the suspension on the substrate [134] or by preparing a flow channel, where the nanowire suspension is continuously pumped over the substrate with a certain flow rate [135]. And finally the nanowires in the suspension are aligned by applying an electrical field. An alternating (AC) voltage of 5–10 V peak to peak is applied to the electrodes on the substrate and depending on the nanowires nature and the nanowire dimensions, frequencies of 1 kHz up to 10 MHz are applied [134, 136–138]. The nanowires are aligned mainly parallel to the direction of the electric field. Nanowire alignment by the use of dielectrophoresis is reported for many metal oxide nanowire materials like tin oxide, zinc oxide or titanium oxide [134].

5.3. Fabrication process

The fabrication process of the tungsten oxide nanowire gas sensors (see figure 5.18 for process parameters and equipment specifications) starts with the fabrication of the required electrodes, so that a measurement of the electrical resistance of the nanowire network during the exposure to a target gas is enabled.

For the silicon based sensor, optical lithography is used to pattern the metallic electrodes. The process steps take place in the following order: spin-coating of the photoresist, exposure by a mask aligner, development of the resist, deposition of the metallic layers (5 nm titanium and 200 nm gold) and the lift-off process.

For the CMOS based sensors, electron beam (ebeam) lithography is used to adapt the already existing electrode systems on the CMOS microhotplates (shown in the figures 5.6 and 5.10). Similar to the process steps of the silicon based sensors, the following steps take place for the CMOS based sensors: spin-coating of the ebeam resist, exposure by an ebeam lithography tool, development of the resist, deposition of the metallic layers (5 nm titanium and 200 nm gold) and the lift-off process. Optical lithography is a simple and common technique compared to ebeam lithography, which is more sophisticated and time consuming. In the case of the CMOS based sensors, ebeam lithography is used, because of the higher flexibility in terms of pattern design.

The used electrode designs for optical and ebeam lithography are shown in figure 5.13 for the silicon based sensor and in figure 5.14 and 5.15 for the CMOS based sensors. The electrode designs are so called IDES (interdigitated electrode system) electrodes. In the silicon based sensor design, the size of the bond pad is $1\text{ mm} \times 1\text{ mm}$ to ensure enough space for manual wire bonding, the IDES contact lines have a length of $500\text{ }\mu\text{m}$ and are $10\text{ }\mu\text{m}$ broad. The spacing between the contact lines is also $10\text{ }\mu\text{m}$. In the CMOS based sensor design, used for MPW3mod and for MPW4, the dimensions of the IDES contact lines are reduced to a length of $32\text{ }\mu\text{m}$ with $2\text{ }\mu\text{m}$ width and a spacing of $2\text{ }\mu\text{m}$ between the contact lines. No bond pads are needed for the CMOS based sensors. The next process step consists of the sensor assembly, which will be explained in detail in the sections 5.3.1 and 5.3.2 for each sensor type.

Finally, the nanowire network is transferred to the fabricated sensor substrates. Therefore,

the preparation of a tungsten oxide nanowire suspension in water is performed: 10 mg of the dry tungsten oxide nanowire powder are suspended in 3 ml deionised water to get a nanowire suspension with a concentration of 3.3 g/l. The nanowire suspension is treated by ultrasonication for 3 min to disperse the nanowires as homogeneously as possible. This nanowire suspension is transferred to an inkjet printer cartridge, which is mounted on the printer (DMP-2831 from FUJIFILM [139]). With a precisely adjustable stage and the fiducial camera of the printer, the nanowire suspension can be deposited on the designated substrate positions.

The final step of sensor fabrication consists of a sensor annealing for 12 h at 400 °C conducted by the integrated heaters of the sensor devices and the applied constant current of 10 nA at the tungsten oxide nanowire network.



Figure 5.11.: Inkjet printer DMP-2831 from FUJIFILM [139].

5.3.1. Sensor assembly of silicon based sensor

The silicon based sensor with typical dimensions of 10x8 mm is glued onto two 10x2 Pt6.8 microheaters (from Delta-R GmbH [140]) and a temperature sensor 4x1 Pt100 temperature sensor (from Delta-R GmbH [140]). The wires of the microheaters and the temperature sensor are soldered onto the appropriate carrier (LxWxH 4.4x3.0x0.8 mm;

designed by mb-Technologies GmbH [141]) to provide the electrical connections and mechanical support for the assembled sensor. The sensor itself is electrically connected to the carrier by wedge-bonding of gold wires (figure 5.12) by the use of a manual wire bonder type 5550 (from F&K DELVOTEC Bondtechnik GmbH [142]) at Austira Institute of Technology (AIT).

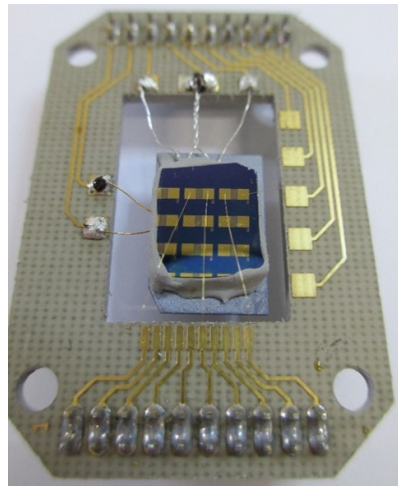


Figure 5.12.: Silicon based sensor assembled on carrier .

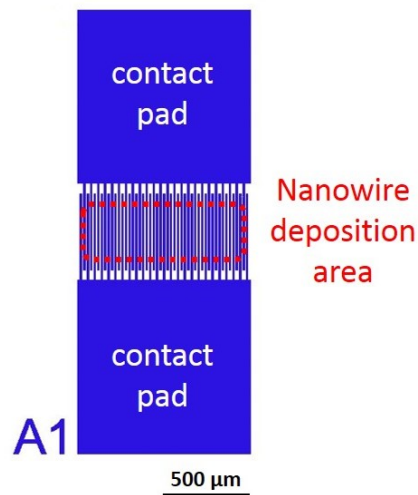


Figure 5.13.: IDES electrode design used for silicon based sensor.

5.3.2. Sensor assembly of CMOS based sensors

The CMOS based sensors are mounted on the appropriate carrier (LxWxH 4.4x3.0x0.8 mm; designed by mb-Technologies GmbH [141]) and bonded by wedge-bonding of aluminium wires by the use of the bonder Bondjet 810 from Hesse GmbH [143] at ams AG (figure 5.16 and 5.17). This assembly is applied to both types of CMOS sensors, MPW3mod and MPW4.

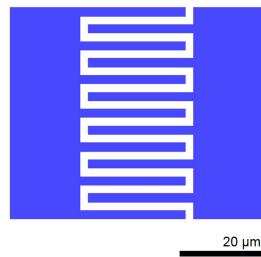


Figure 5.14.: IDES electrode design used for MPW3mod and MPW4.

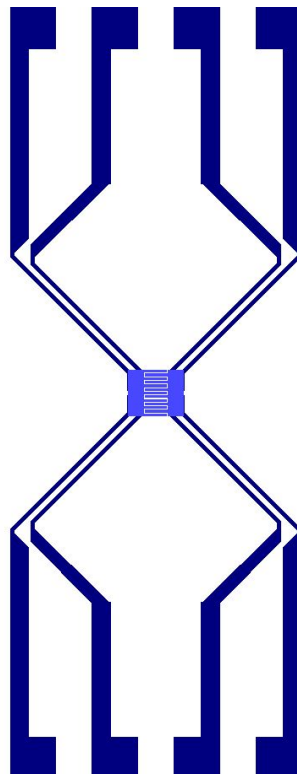


Figure 5.15.: MPW4 electrodes with IDES electrodes made by ebeam lithography.

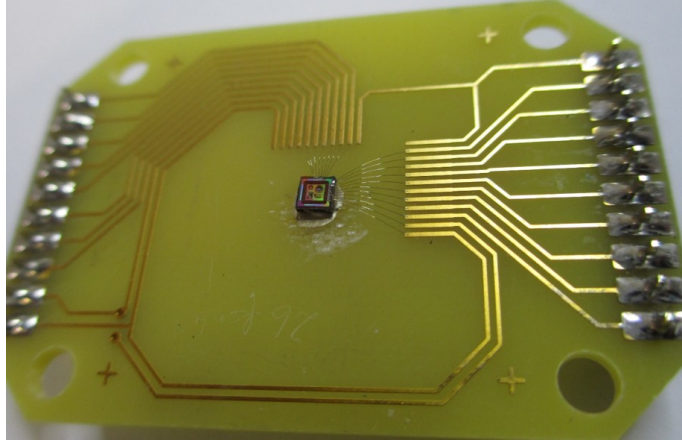


Figure 5.16.: CMOS MPW3mod microhotplate chip wire bonded on carrier.

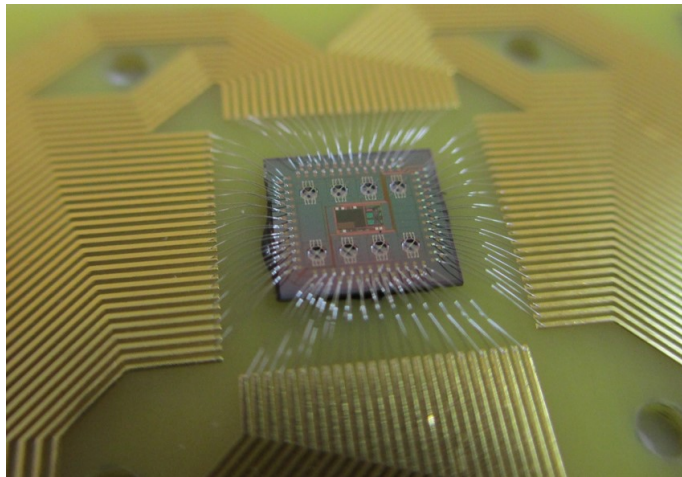


Figure 5.17.: CMOS MPW4 microhotplate chip wire bonded on carrier.

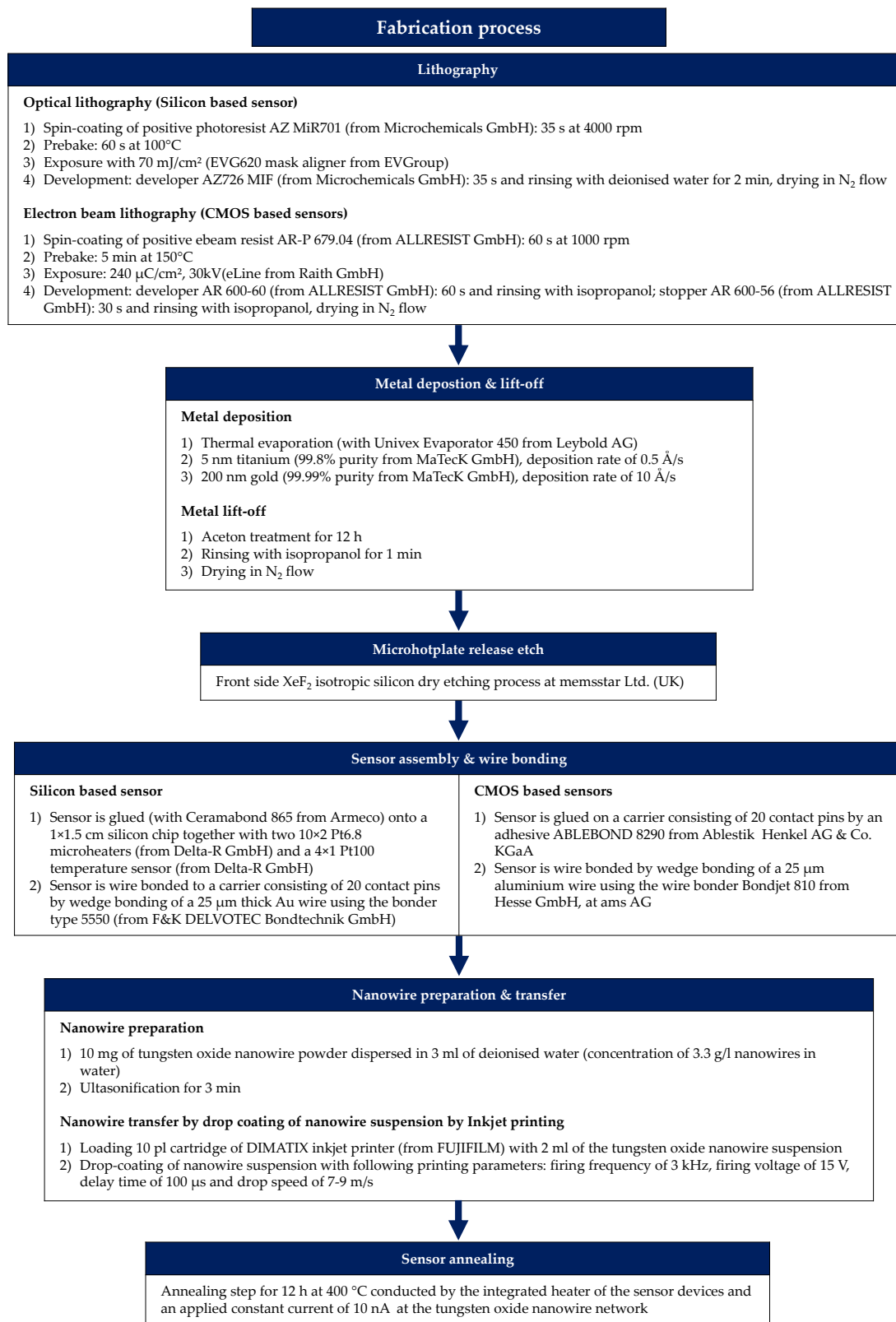


Figure 5.18.: Fabrication process of tungsten oxide nanowire gas sensors.

5.3.3. Design of electrode structure

Electrode material

Various studies concerning electrode materials for metal oxide gas sensors can be found in literature [13, 144]. Noble metals are the preferential choice because of their high stability which is the most important requirement for an application as electrode material. Noble metals like silver (Ag), platinum (Pt) or gold (Au) have been intensively studied over decades. Silver is well known for degradation effects because it easily moves in an electric field applied to the electrodes at elevated temperatures [144]. Platinum is the most stable of the three above mentioned metals [145]. It has a low affinity towards diffusion and even at high temperatures it is not likely to oxidise. It is also stable against corrosive gases [146]. But platinum also has drawbacks like the bad adhesion and the resulting necessity of an adhesion layer like titanium or chromium. Gold shows diffusion effects but is a quite stable electrode material compared to diffusion effects of silver.

Using noble metals as electrode materials, the chemical effects caused by the metal at the electrode/sensing material interface have to be taken into account. Platinum and gold are well known for their catalytic nature and can therefore affect the sensor response of a metal oxide gas sensor [13].

The choice of titanium/gold electrodes for the tungsten oxide nanowire network gas sensor results from empirical values of former work [147] and the common use of this metal combination in commercially available microhotplates.

Electrode geometry

Interdigitated electrodes are chosen as the appropriate electrode structure for the nanowire network gas sensor to ensure a good electrical connection between the randomly placed nanowires and the electrical circuit. Numerous parallel connections are formed between the nanowires and the electrodes. The spacing between the contact lines of the interdigitated electrodes has an influence on the sensor performance as Tamaki et al. [148] has reported in 2005. Therefore, the size of the spacing has to be considered

carefully with respect to the nanowire dimensions. The tungsten oxide nanowires synthesised in this work show a length of 1–10 μm . The spacing is chosen to be 10 μm for the design of the silicon based sensor, which is accurately feasible with the available photo-lithography tool, so that even one or two nanowires could bridge the gap. As already discussed in chapter 2.2.3, the resistance of the nanowire network results, besides the nanowire resistance itself, from various interfaces: the electrode/nanowire, the nanowire/nanowire and the nanowire/electrode interfaces. This leads to the conclusion that a smaller spacing between the electrodes causes a lower sensor resistance because of less nanowire/nanowire interfaces [149]. Therefore, the spacing is chosen to be even smaller for the CMOS based sensors (2 μm), which is not feasible by the used optical lithography tool but ebeam lithography can handle these dimensions with ease.

5.4. Discussion

5.4.1. Nanowire morphology change during sensor annealing

After the last sensor process step, the sensor annealing, the tungsten oxide nanowires appear in a different morphology. Figure 5.19 shows the nanowire network before and figure 5.20 after this process step on the CMOS MPW4 sensor. The tungsten oxide nanowires morphology clearly changes during the process step, from a dense network of short nanowires with diameters in the range of 10 to 30 nm to more or less oriented large nanowires with diameters up to 100 nm, looking like needles. The applied electric field seems to cause the orientation of the nanowires, which mainly organise themselves at the positive electrode.

The observations of the morphology change are in good agreement with the findings of the Raman measurements (section 4.2.5), where the change in the Raman spectra is suggested to be due to a crystal growth effected by the laser induced temperature. Therefore, an additional CMOS MPW4 tungsten oxide nanowire gas sensor is fabricated and used for an in situ Raman measurement during the sensor annealing process. This investigation is explained in detail in the next section.

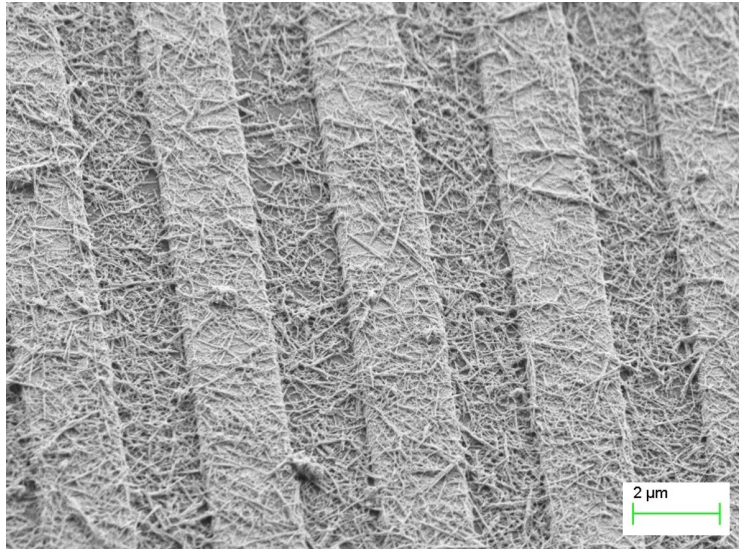


Figure 5.19.: CMOS MPW4 tungsten oxide nanowire sensor before sensor annealing.

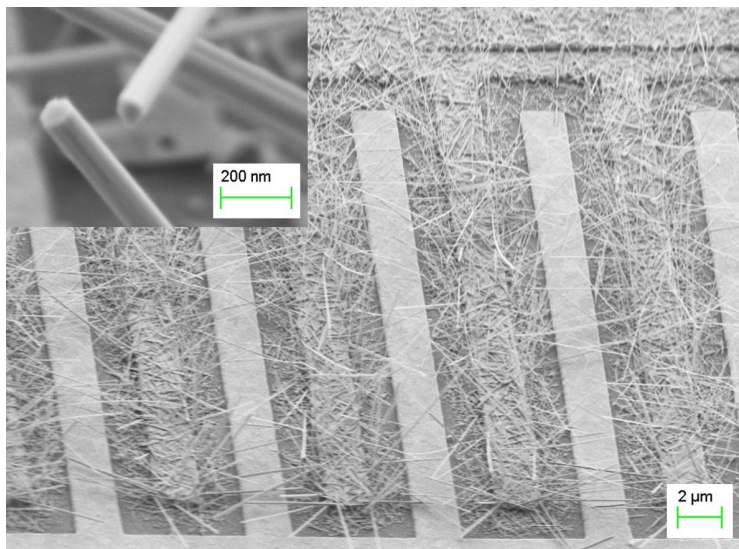


Figure 5.20.: CMOS MPW4 tungsten oxide nanowire sensor after sensor annealing at 400 °C and an applied current of 10 nA for 12 h.

5.4.2. In situ Raman measurement of sensor annealing process

The Raman measurements are conducted in ambient air (laser: 633 nm He-Ne; red), while the CMOS MPW4 tungsten oxide nanowire sensor undergoes the sensor annealing at 400 °C with an applied constant current of 10 nA at the nanowire network for 12 h. As current sources for the CMOS microhotplate heater and the nanowire sensor material, source measure units (2400 SourceMeter, from Keithley) are used. The measurements are taken with a laser power of 0.65 mW before the sensor annealing starts (0 h), 1 h, 2 h, 3 h, 4 h, 5 h after the start and at the end of the annealing process at 12 h.

The resulting Raman spectra (figure 5.21) show the development of peak profile as expected from the Raman investigations in section 4.2.5. The broad peaks measured at the initial state of the nanowires become sharpened and reach the defined peak profile after 12 h of sensor annealing. In figure 5.23 (left), the image of the CMOS MPW4 microhotplate, covered with the nanowires, is shown in the initial state. A dense nanowire network layer can be seen on top of and in between the IDES gold electrodes. After 3 h of sensor annealing, a change in the morphology of the nanowires can be seen: large nanowires (highlighted in red in figure 5.23 (right)) are already oriented on the positive electrode, the one to the right side of the image. In figure 5.22, the Raman spectra at 0 h, 1 h, 2 h, 3 h and 4 h are zoomed out. The peak at 960 cm^{-1} is decreasing from 0 h to 4 h. Already in the spectrum at 3 h, the peak is not significantly assignable any more. As already discussed in the section 4.3, the decrease or rather disappearance of this peak at 960 cm^{-1} , which represents terminal W=O bonds, is indicated as a crystal growth process [41]. This is in good agreement with the observations in figure 5.23 (right), where the grown nanowires can be seen. After 12 h, the complete nanowire network is transformed into even larger nanowires (figure 5.24). At this point, the Raman spectrum (black line in figure 5.21) shows a clear peak profile with sharp peaks. The peaks and their positions can not be used to absolutely identify the stoichiometry of the tungsten oxide nanowires, but the crystal growth during the sensor annealing process can be confirmed by the findings of the in situ Raman measurement.

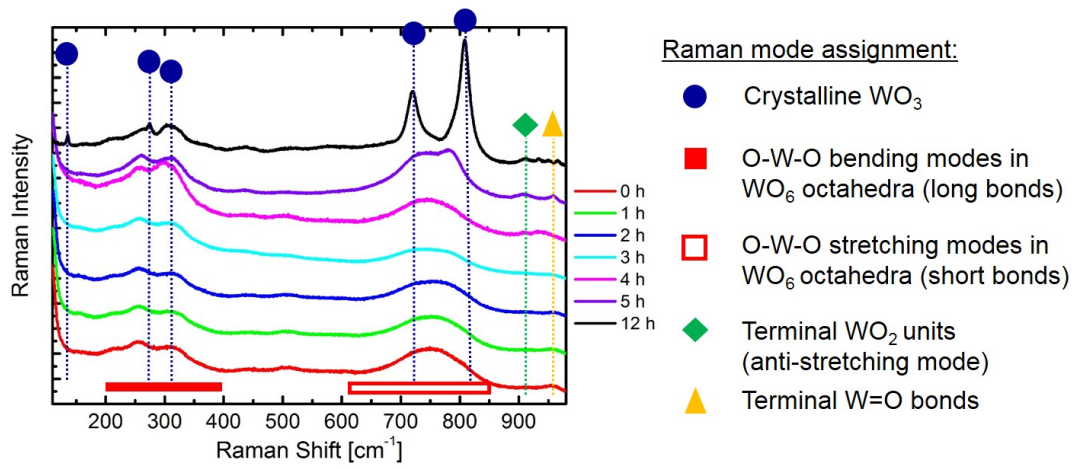


Figure 5.21.: Raman spectra during sensor annealing with several measurements, when the sensor annealing starts (0h) and within the 12h.

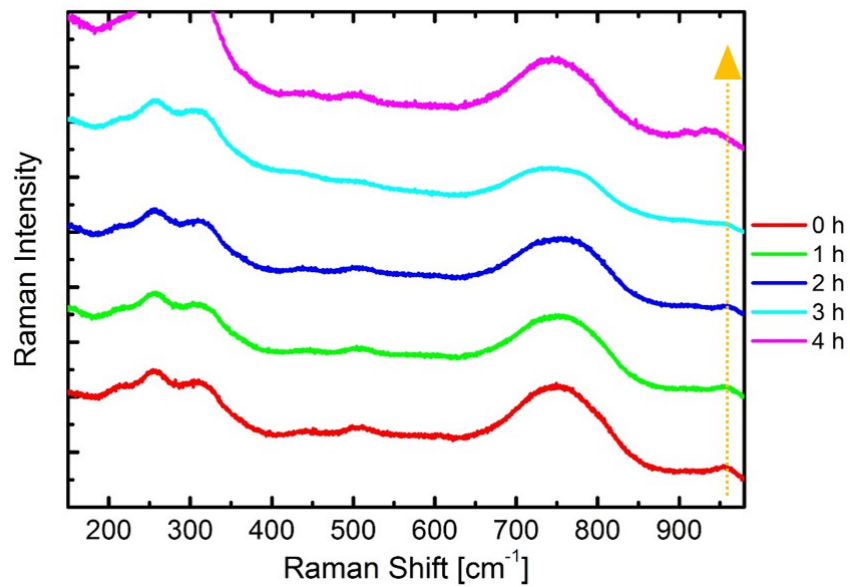


Figure 5.22.: Raman spectra during sensor annealing with measurements at 0h, 1h, 2h, 3h and 4h.

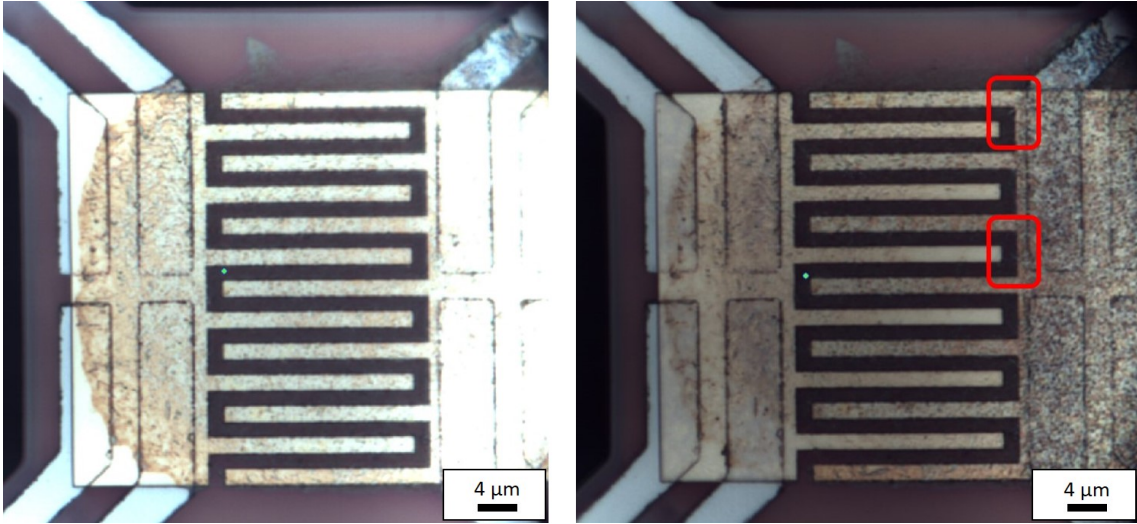


Figure 5.23.: Microscope image at Raman measurement setup at the start of sensor annealing (left) and after 3 h (right).

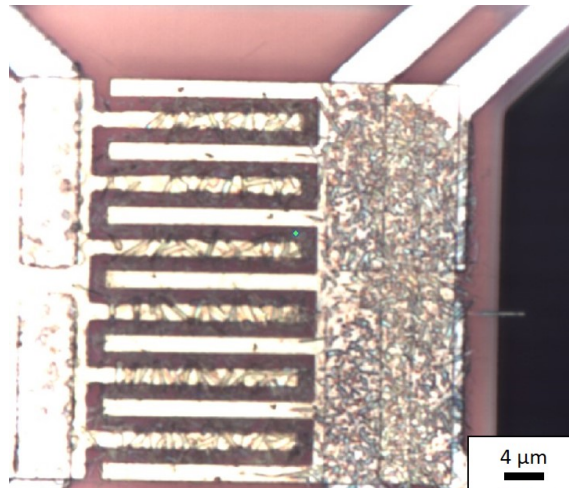


Figure 5.24.: Microscope image at Raman measurement setup after 12 h of sensor annealing.

6. Characterisation of gas sensing properties

6.1. Gas reaction mechanisms

The understanding of the gas reaction mechanisms of target gas molecules with the tungsten oxide nanowire surface is crucial for a reliable gas sensor system. Therefore, reaction mechanisms are discussed in this section for the target gases used in this work. In literature, no detailed reports about reaction mechanisms of target gases with tungsten oxides can be found and thus, it is assumed that similar reaction processes take place as reported for the most commonly studied semiconductor tin oxide (SnO₂).

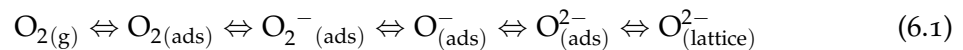
In this work, the tungsten oxide nanowire gas sensors are tested for three target gases:

- hydrogen sulphide H₂S
- carbon monoxide CO
- carbon dioxide CO₂

Prior to the above mentioned target gas reactions, reactions with ambient oxygen and humidity are considered and discussed.

6.1.1. Oxygen O₂ and humidity H₂O

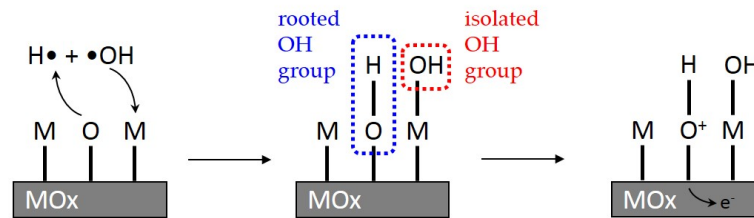
As already discussed in section 2.1, according to the ionosorption model, oxygen molecules ionosorb to the metal oxide surface. Oxygen is a strong electron acceptor and therefore it can be reduced by the metal oxide surface in various species (equation 6.1). Below 200 °C, the molecular form (O₂⁻_(ads)) and above 200 °C, the atomic forms (O⁻_(ads) and O²⁻_(ads)) of oxygen are present at the metal oxide surface [12].



In more detail, the ambient oxygen molecules physisorb at the tungsten oxide surface and electrons from the conduction band are trapped by the oxygen molecules. The formed space charge layer (depletion layer) causes an upward band bending in the tungsten oxide, which results in a decreased conductivity [150].

Humidity is a crucial factor influencing metal oxide gas sensor measurements. In most gas sensor applications, humidity is present in the tested atmosphere, where water molecules react with the metal oxide surface. The appearance of water on metal oxide surfaces is directed by the applied sensor temperature. Water molecules physisorb at the metal oxide surface or adsorb by hydrogen bonding on oxygen species (present at the surface; ionosorbed oxygen species or lattice oxygen) below 200 °C. At temperatures higher than 200 °C the water molecules are dissociated and form chemisorbed hydroxy groups at the metal oxide surface [151–153]. For the formation of the hydroxy groups, two mechanisms are suggested (figure 6.1) [153–155].

Mechanism A



Mechanism B

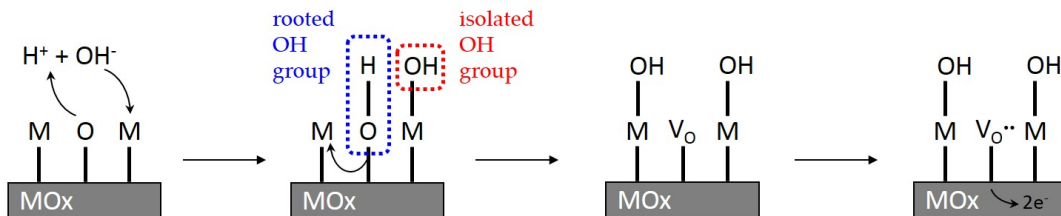
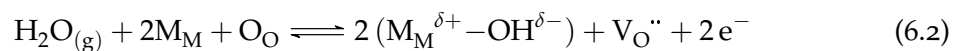
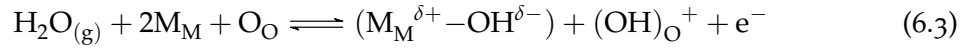


Figure 6.1.: Scheme of water adsorption mechanism on metal oxide (MOx) surfaces [153].

Mechanism A represents the heterolytic dissociation of water molecules, where the formed hydroxy group reacts with the metal atom (isolated OH group) and the proton reacts with a lattice oxygen at the metal oxide surface and forms the rooted hydroxy group. Subsequently, this rooted hydroxy group binds to a metal atom and generates an oxygen vacancy. The oxygen vacancy can be ionised releasing two electrons into the conduction band (equation 6.2).



Mechanism B suggests the homolytic dissociation of water molecules and the following chemisorption of hydroxy group to a metal atom. The hydrogen reacts with a lattice oxygen at the metal oxide surface and forms the rooted OH group. This OH group can be ionised and therefore it releases one electron to the conduction band (equation 6.3).

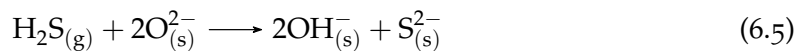
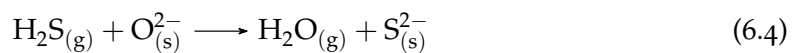


The suggested mechanisms assume the adsorption of water molecules on a metal oxide surface without the influence of other molecules but the consideration of ionosorbed oxygen species at the metal oxide surface is essential. Morrison [156] suggested the neutralisation of the attractive sites (H^+ and OH^- groups) at the surface by physisorption of water molecules which is inhibiting the formation of ionosorbed oxygen species. Caldararu et al. [152] reported on a similar assumption that water molecules stabilise anionic vacancies by coordinatively adsorbed water molecules and surface hydroxy groups and therefore block these oxygen adsorption sites. What emerges from the comprehensive reports on the interaction of oxygen and water molecules with metal oxides is the understanding of the major role of these molecules in the gas sensing processes.

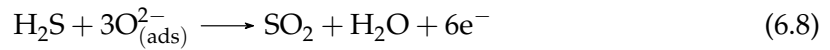
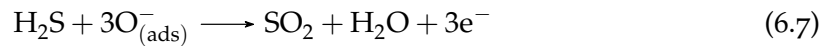
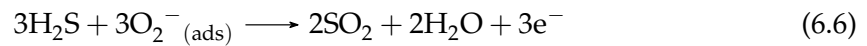
6.1.2. Hydrogen sulphide H_2S

Hydrogen sulphide has a similar molecular structure to water, but its chemical properties are different. Compared to water, it forms no strong hydrogen bonds because of its lower polarity. Hydrogen sulphide also differs regarding the reactivity. Due to the lower bond strength of S–H bonds compared to O–H bonds, the dissociation energy of hydrogen sulphide is lower than for water.

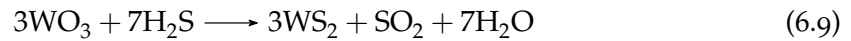
Different reaction mechanisms are reported for the reaction of hydrogen sulphide with metal oxide surfaces. Without oxygen species being present, it is suggested that hydrogen sulphide reacts with lattice oxygen according to the equations 6.4 and 6.5.



In the presence of oxygen, hydrogen sulphide is assumed to react with the ionosorbed oxygen species at the tungsten oxide surface. The reactions shown in the equations 6.6, 6.7 and 6.8 lead to the release of electrons into conduction band and hence to a decrease in resistance of the tungsten oxide material. As already discussed in section 6.1.1 the molecular form of ionosorbed oxygen is present at the metal oxide surface at temperatures lower than 200 °C (equation 6.6) and the atomic forms exist at higher temperatures (equations 6.7 and 6.8) [157].



At higher temperatures (above 250 °C) reactions of hydrogen sulphide with the metal oxide can also occur by reducing the tungsten atom from W^{6+} to W^{4+} following equation 6.9 [158–161].



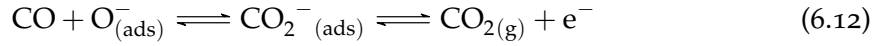
6.1.3. Carbon monoxide CO

Carbon monoxide consists of a triple bond ($\text{C}\equiv\text{O}$) with a relatively high dissociation energy value. In literature, different reaction mechanisms are assumed for the reaction of carbon monoxide with metal oxide surfaces. In an oxygen-free environment, the carbon monoxide molecules directly adsorb to the lattice oxygen and form CO^+ groups at the metal oxide surface (equation 6.10) or react with lattice oxygen species and form oxygen vacancies, which serve as donors 6.11 [162].



In the presence of oxygen, the direct adsorption to the lattice oxygen is hindered and therefore the carbon monoxide molecules react with the ionosorbed oxygen species.

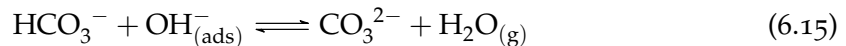
Carbon dioxide is formed whereby electrons are released into the conduction band (equation 6.12) [162].



Carbon monoxide is a well studied target gas and therefore also reaction mechanisms in the presence of humidity are reported, where carbon monoxide reacts with ionosorbed oxygen species and the hydroxy groups on the surface in parallel. Carbon monoxide is oxidised by the oxygen of the isolated hydroxy group and a carbon dioxide molecule is formed whereas the hydrogen atom forms a rooted hydroxy group with a lattice oxygen which can become ionised and electrons are released into the conduction band.

6.1.4. Carbon dioxide CO₂

Carbon dioxide is a linear molecule with two double bonds (O=C=O). It is a stable molecule, which can only be decomposed at very high temperatures (above 1000 °C). Although the detection of CO₂ is crucial for gas sensor systems, there are few reports on CO₂ metal oxide gas sensors [163–166]. No detailed literature about the reaction of CO₂ and metal oxide gas sensors in oxygen-free atmosphere can be found. The equations beneath show the assumed reaction mechanisms, which take place at the metal oxide surface when exposed to carbon dioxide at elevated temperatures (equation 6.13) [167] and at low temperatures (<100 °C) (equations 6.14 and 6.15) [164] in humid air atmosphere.



By the formation of the carbonate, a negative charge can be released into the conduction band, which decreases the materials resistance. It seems, that the reaction mechanism relies on the equilibrium of carbon dioxide and the metal hydrogen carbonate/carbonate.

6.2. Equipment & methods

6.2.1. Gas measurement setup

The developed tungsten oxide nanowire gas sensors are tested in the gas measurement setup, which is shown in the figures 6.2 and 6.3. The gas measurement setup consists of mass flow controllers (MFC, F-201CV from Bronkhorst) to regulate the gas supply, a current source to apply the required current to the heater (PL330P, from Thurlby Thandar Instruments for silicon based sensor and 2400 SourceMeter, from Keithley for the CMOS sensor), a source measure unit (2400 SourceMeter, from Keithley) to perform the resistance measurement of the sensor material and a multimeter (34401A, from Agilent Technologies) to read out the sensor's thermocouple.

The used background gas is synthetic air (80 % nitrogen, 20 % oxygen from Linde Gas GmbH), unless noted differently. As shown in figure 6.3, the background gas flow is controlled by two MFCs: one gas stream is bubbled through a water reservoir to provide humidity, the other one represents the dry background gas flow. The relative humidity in the background gas flow is measured by a commercial humidity sensor (rh sensor, AFK-E from Kobold). The target gas flow is controlled by three MFCs. Each MFC is calibrated for a specific flow range and therefore low, medium and high concentrations can be precisely adjusted by using the MFC with the appropriate flow range. All MFCs are controlled by a computer using a LabView application. The total gas flow (background gas flow + target gas flow) fed to the gas chamber is kept constant at 1000 sccm for all gas measurements presented in this work.



Figure 6.2.: Gas measurement setup in the laboratory.

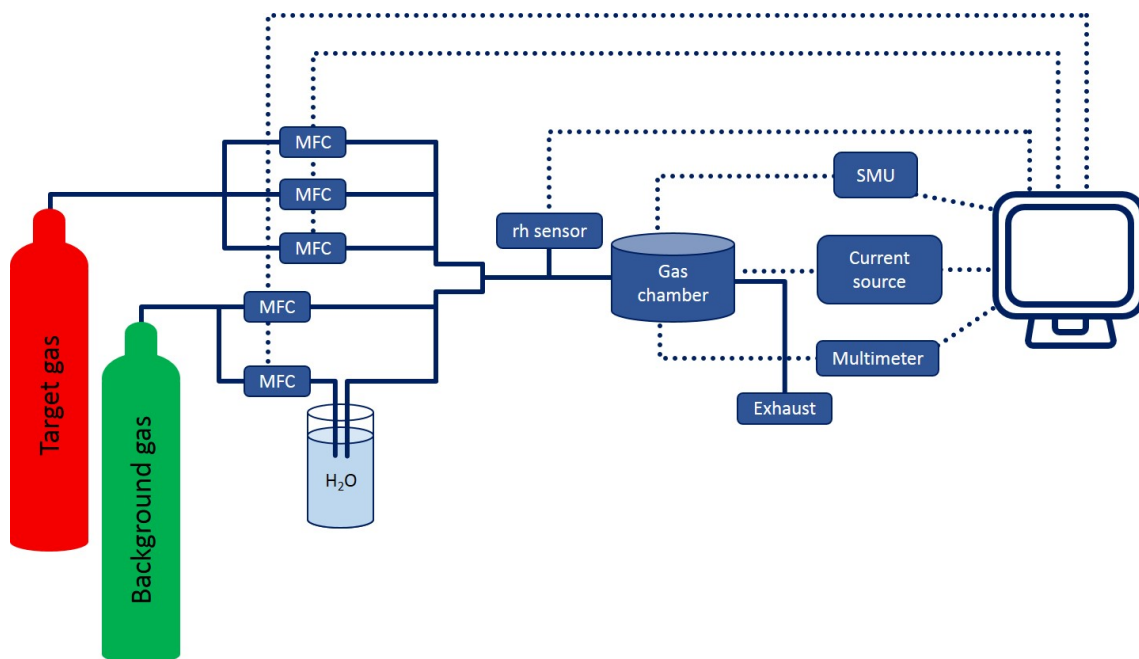


Figure 6.3.: Scheme of gas measurement setup; MFC (mass flow controller), rh sensor (relative humidity sensor), SMU (source measure unit).

6.2.2. Measurement procedure

The tungsten oxide nanowire sensors are operated in a constant current mode and the voltage is read out for the resistance measurement.

- At the beginning of each measurement, a 30 min time period is set, where background gas is conducted through the gas chamber to ensure the required atmospheric conditions and flush out any residuals of other gas species.
- Measurement programs are constituted, so that the sensor is tested in different operation temperatures.
- While keeping the sensor on a certain temperature, humidity changes are applied to the system (see figure 6.4).
- Three humidity levels (25 %, 50 % and 75 % relative humidity at 20 °C) are chosen to represent humidity conditions in real environment.
- The target gas is induced into the gas chamber in the chosen concentrations, whereas the overall flow stays constant at 1000 sccm (reducing the background gas flow by the target gas flow). The constant overall gas flow is a crucial factor, because changing flow rates can cause flow turbulences in the gas chamber.
- The different gas pulses are set for 5 min with breaks of 15 min in between (see figure 6.5).

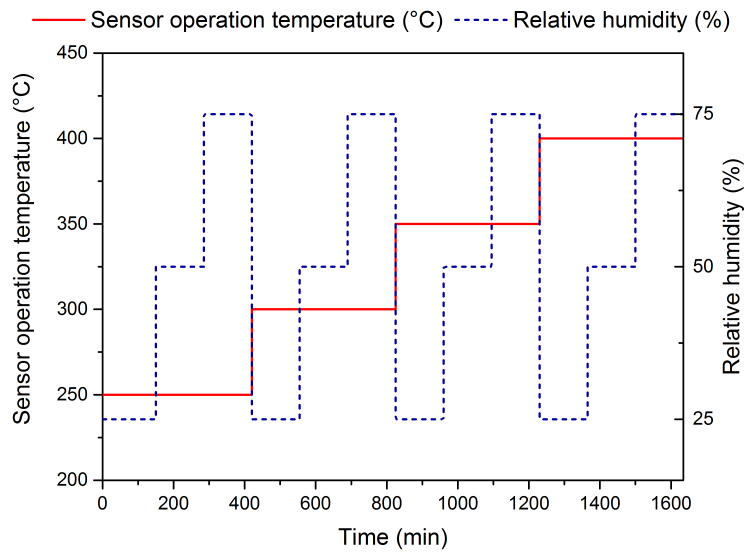


Figure 6.4.: Scheme of gas measurement with stepwise increasing temperature and varying humidity levels.

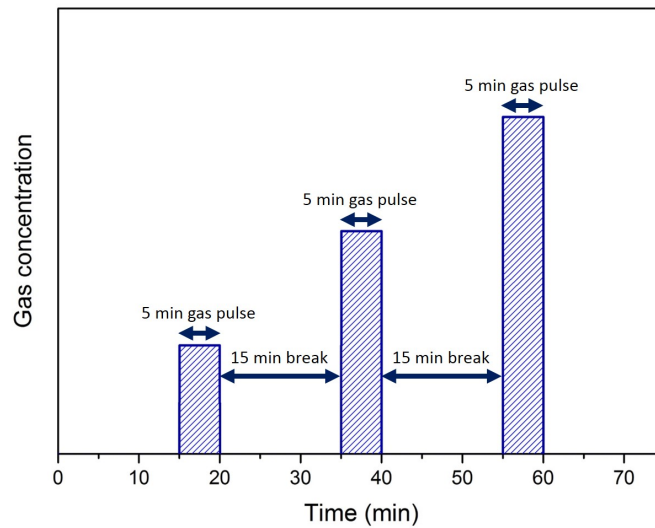


Figure 6.5.: Scheme of gas pulse configuration.

6.2.3. Data analysis

The data obtained from tungsten oxide nanowire gas sensing measurements is analysed in terms of sensor response (S), which is defined as the relative difference between the resistance value in the background gas (R_{air}) before the gas pulse and the resistance value during the gas pulse (R_{gas}) expressed in percentage (equation 6.16).

$$S[\%] = \frac{|R_{gas} - R_{air}|}{R_{air}} \times 100 \quad (6.16)$$

Further essential parameters of gas sensors are the response time t_{resp} and the recovery time t_{recov} . The response time is defined as the time the sensor resistance takes to reach 90% of its saturation value during the gas pulse, whereas the recovery time is defined as the time the sensor resistance takes to reach the resistance value 10% below the initial resistance (see figure 6.6).

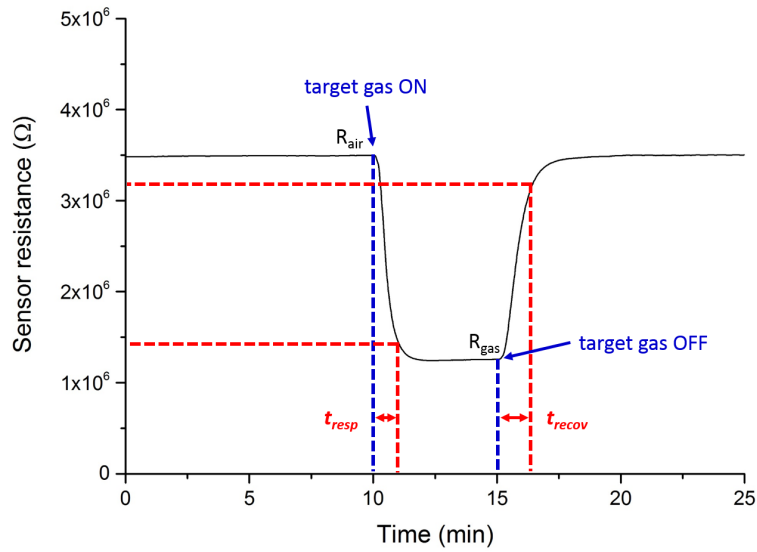


Figure 6.6.: Scheme of response and recovery time definition.

6.3. Gas measurement results

6.3.1. Description of nanowire gas sensors

The presented gas measurements are performed with different sensor devices shown in table 6.1:

- The silicon based (SB) sensor is mainly used to pretest the sensing abilities of the tungsten oxide nanowire material. This device consists of two sensors (sensor 1 and 2) on the same silicon chip. The same amount of nanowire suspension is deposited onto these two sensors, so that the sensors should show the same sensitivity, when exposed to a certain target gas.
- The same amount of nanowire material is deposited on the CMOS MPW3mod microhotplate. This sensor is specified as MPW3mod in table 6.1.
- The CMOS MPW4 sensor is fabricated with twice the amount of nanowire material to investigate the influence of nanowire density and the thereof potential improvement of gas sensor sensitivity.
- The SB sensor is also used to analyse the reaction mechanisms of H₂S and CO with the tungsten oxide material in nitrogen atmosphere at the lowest possible humidity level of 3 %, limited by the gas measurement setup.

Table 6.1.: Sensor assignment for specific target gases.

Target gas	Carrier gas	Concentration	Relative humidity (%)	Temperature range (°C)	Investigated sensors
H ₂ S	SA	100–1000 ppb	25 – 75	250 – 400	SB, MPW3mod
H ₂ S	SA	10–60 ppb	50	250	MPW3mod
CO	SA	10–200 ppm	25 – 75	250 – 350	SB, MPW4
CO ₂	SA	500–2000 ppm	25 – 75	300 – 400	SB, MPW3mod
H ₂ S	N ₂	1000 ppb	3	250	SB
CO	N ₂	200 ppm	3	350	SB

6.3.2. Sensor response to H₂S

An initial test program is applied to the silicon based tungsten oxide nanowire gas sensor (SB), where the sensor is exposed to various ppb-levels of H₂S between 100 ppb and 1000 ppb in three relative humidity levels (25 %, 50 % and 75 % at 20 °C) to determine if the sensor is sensitive to H₂S in general. The sensor shows a decrease in the sensor resistance while being exposed to H₂S, which means the sensor is sensitive to this highly toxic target gas. According to the evaluation of the complete test gas measurement with sensor operation temperatures between 250 °C and 400 °C in 50 °C steps, the sensitivity of the sensor reaches its maximum at an operation temperature of 300 °C, which is presented in terms of sensor response (described in chapter 6.2.3) in figure 6.7.

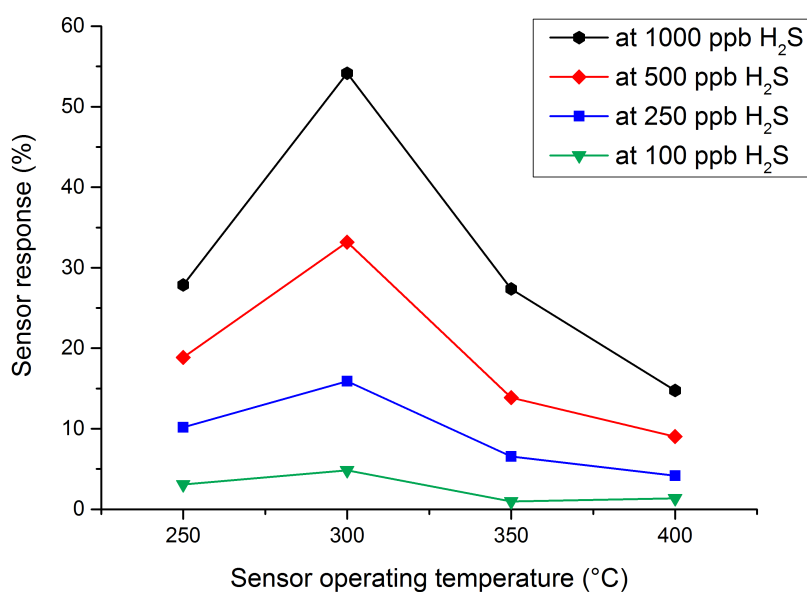


Figure 6.7.: Sensor response (sensor 1) vs. sensor operation temperature at 100 ppb, 250 ppb, 500 ppb and 1000 ppb H₂S.

The sensitivity of the tungsten oxide nanowire material to H₂S is proven by the SB sensor and is transferred to CMOS technology. The CMOS based tungsten oxide nanowire sensor MPW3mod is exposed to 100 ppb, 250 ppb, 500 ppb and 1000 ppb H₂S at the three relative humidity levels at the operation temperature of 300 °C. The sensor resistance at the three humidity levels is shown in figure 6.8. The resistance decreases as expected for the reaction of an n-type semiconductor material with a reducing gas like H₂S and increases again, when the flow of H₂S is switched off. The resistance change increases with increasing concentration of the H₂S gas pulses. The measurement shown in figure 6.8 is evaluated in terms of sensor response. The sensor response to H₂S at the sensor operation temperature of 300 °C is presented in figure 6.9. The sensor shows the highest sensitivity at the lowest humidity level of 25 % relative humidity. With the increasing humidity level the sensor response decreases from 55 % at 25 % relative humidity to 47 % at 75 % relative humidity. It can therefore be concluded that the sensor is not just sensitive to H₂S, but also to humidity at the operation temperature of 300 °C.

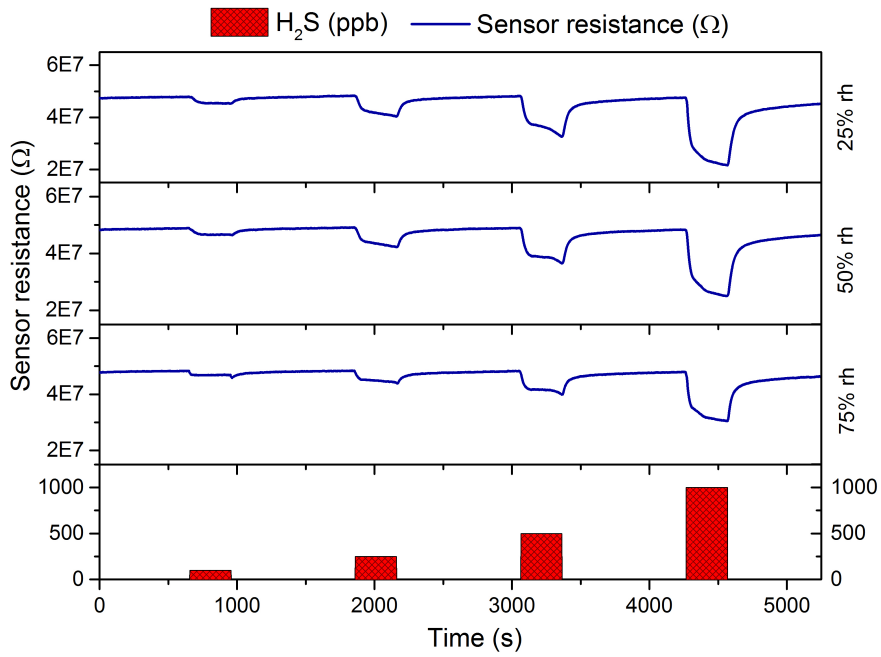


Figure 6.8.: H₂S gas measurement at 300 °C and three relative humidity levels exposed to 100 ppb, 250 ppb, 500 ppb and 1000 ppb H₂S.

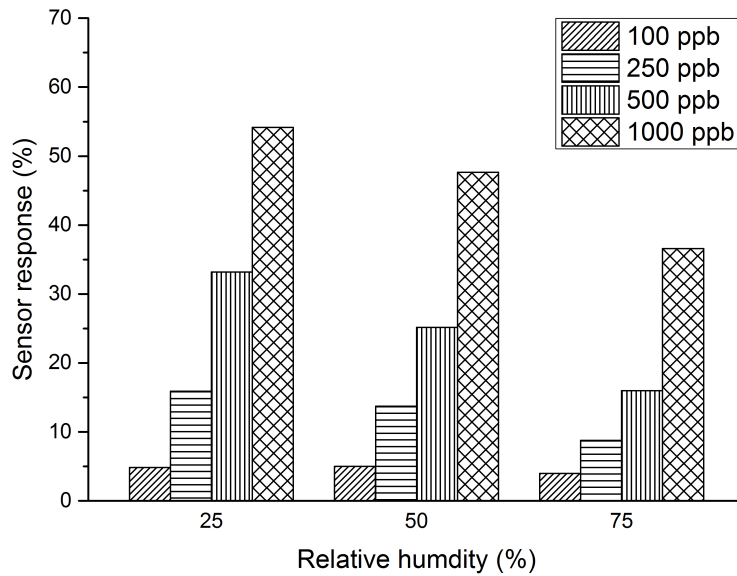


Figure 6.9.: H₂S gas response in (%) at 300 °C at three relative humidity levels.

According to the evaluation of the initial test gas measurement shown in figure 6.7, the sensor response at the operation temperature of 250 °C is less than at the operation temperature of 300 °C but the sensor shows still an acceptable performance. At higher temperatures (350 °C and 400 °C), the sensor response decreases significantly. At 350 °C sensor operation temperature the sensor shows a similar sensor response, but still less than at 250 °C and at 400 °C the sensor response drops down to less than 20 % even at the exposure of 1000 ppb H₂S. Therefore, the CMOS based sensor MPW3mod is tested at the operation temperature of 250 °C as an alternative to 300 °C. The sensor is exposed to the same H₂S levels of 100 ppb, 250 ppb, 500 ppb and 1000 ppb H₂S at the three relative humidity levels. The sensor signal is shown in figure 6.10. The change in the sensor resistance is less intense as at the operation temperature of 300 °C, but the humidity influence is negligibly low, which is a remarkable advantage. The sensor response shown in figure 6.11 illustrates the humidity independence of H₂S sensing of the CMOS tungsten oxide nanowire sensor at 250 °C operation temperature.

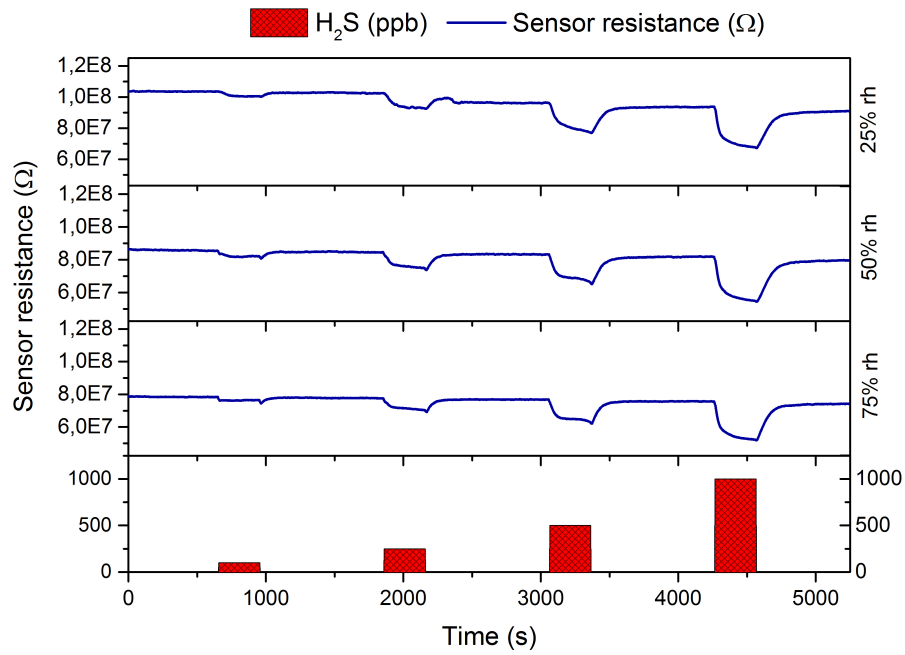


Figure 6.10.: H₂S gas measurement at 250 °C and three relative humidity levels exposed to 100 ppb, 250 ppb, 500 ppb and 1000 ppb H₂S.

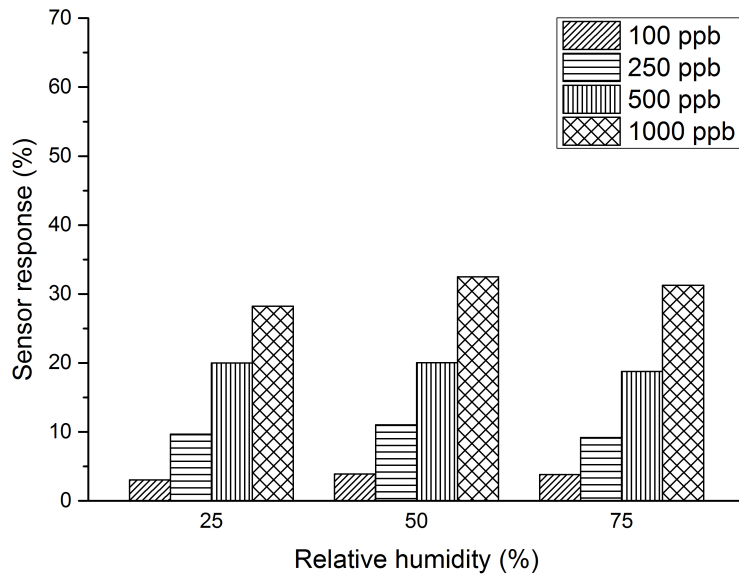


Figure 6.11.: H₂S gas response in (%) at 250 °C at three relative humidity levels.

The sensor response times of the H₂S gas measurements are evaluated as described in section 6.2.3. The normalised sensor resistance at the exposure to 1000 ppb H₂S at 250 °C and 300 °C at 50% relative humidity are shown in figure 6.12. The already seen lower sensor response at 250 °C is once again obvious. No great influence of the two different sensor operation temperatures on the response and recovery times can be identified, but what draws attention, are the very high response and recovery times presented here.

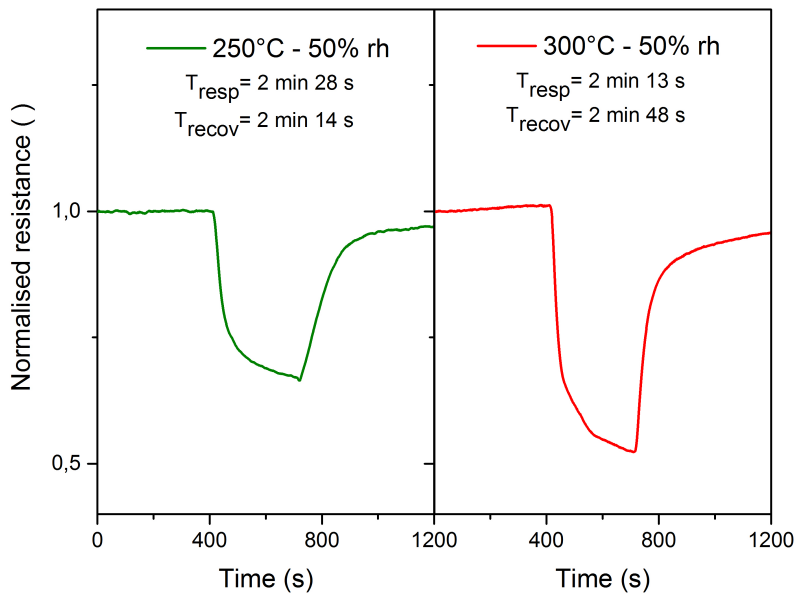


Figure 6.12.: Normalised sensor resistance for the exposure to 1000 ppb H₂S at 250 °C and 300 °C at 50% relative humidity with calculated response and recovery times.

To provide a realistic gas environment, CO₂ is added to the background gas of synthetic air (80% N₂ and 20% O₂). A possible cross sensitivity of the CMOS tungsten oxide nanowire gas sensor to CO₂ can be investigated in this way. The amount of 500 ppm CO₂ is added to the gas stream while keeping the overall gas flow constant at 1000 sccm by the adjustment of the background gas flow. The level of 500 ppm is oversized in respect of today's continuously increasing CO₂ levels in urban centres, where the CO₂ level already reached the 400 ppm threshold value. Figure 6.13 shows the gas sensor resistance at 250 °C and 50% relative humidity exposed to the same H₂S gas pulses of 100 ppb, 250 ppb, 500 ppb and 1000 ppb H₂S with an additional constant flow of 500 ppm CO₂. The CMOS tungsten oxide nanowire sensor shows a significant change in the sensor resistance when it is exposed to H₂S and seems unaffected by the additional gas species CO₂. The sensor response shown in figure 6.14 emphasises the finding, where the independence of the sensor response to the added CO₂ can be proven.

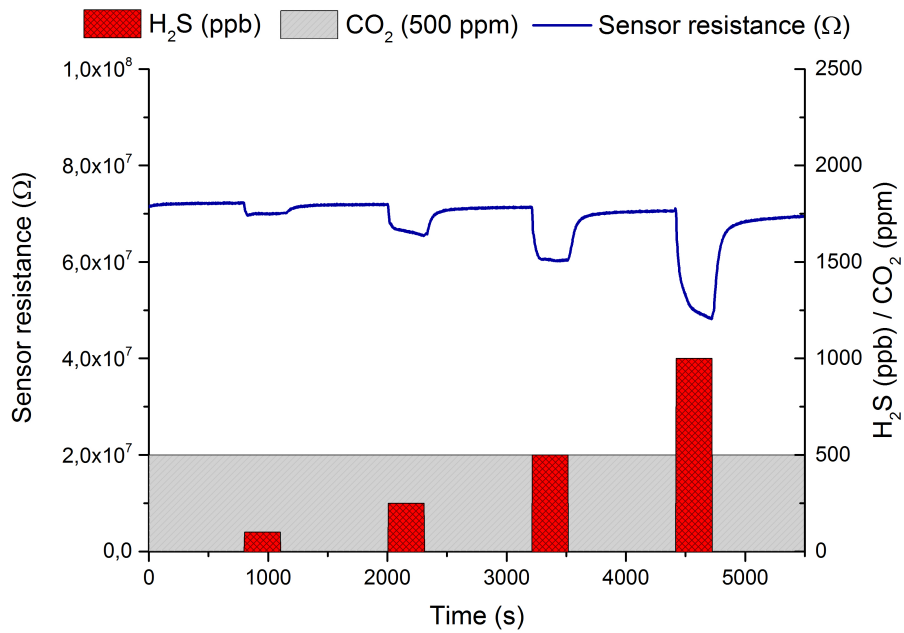


Figure 6.13.: H₂S gas measurement at 250 °C and 50% relative humidity exposed to 100 ppb, 250 ppb, 500 ppb and 1000 ppb H₂S with 500 ppm CO₂ added to the background gas.

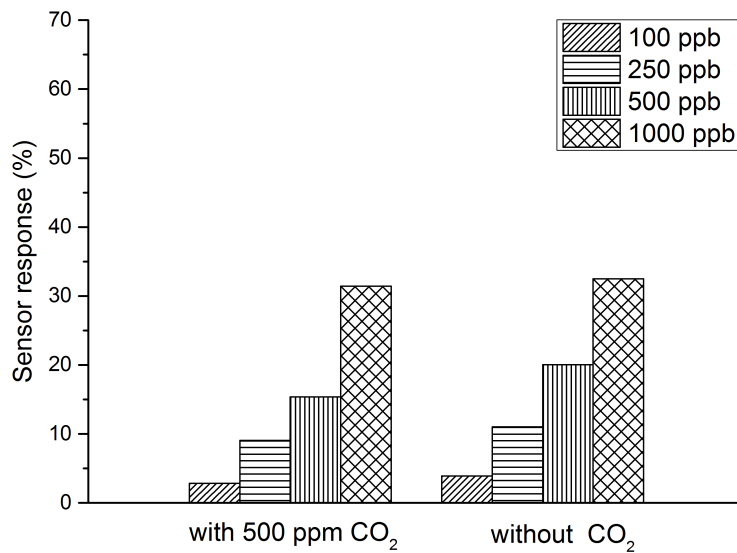


Figure 6.14.: H₂S gas response in (%) at 250 °C at three relative humidity levels with 500 ppm CO₂ added to the background gas.

The following conclusions can be drawn from the gas sensor evaluation for the exposure to H₂S:

- The tungsten oxide nanowire material is sensitive to H₂S.
- The evaluations of the silicon based and the CMOS based sensor correspond to each other.
- The response to ppb-levels of H₂S is higher at the sensor operation temperature of 300 °C, but influenced by humidity changes.
- The response at the sensor operation temperature of 250 °C is less intense, but humidity influence can be reduced in this way to a minimum.
- The response and recovery times are high, no matter if the sensor is conducted at 250 °C or 300 °C.
- The H₂S gas sensing performance is not affected by CO₂ at the sensor operation temperature of 250 °C.

6.3.3. Sensor response to CO

An initial test program is applied to the silicon based tungsten oxide nanowire gas sensor, where the sensor is exposed to various ppm-levels of CO (10 ppm, 30 ppm, 60 ppm, 100 ppm, 150 ppm and 200 ppm) in three relative humidity levels (25 %, 50 % and 75 % at 20 °C) at sensor operation temperatures of 250 °C, 300 °C and 350 °C to determine if the sensor is sensitive to CO. The sensor shows a high response to the CO exposure.

To test the reproducibility of the nanowire printing process, the two sensors (sensor 1 & 2) on the same SB sensor device are tested simultaneously in the above described manner and show same sensor responses. The gas measurements at the highest sensor operation temperature of 350 °C are presented in figure 6.15 for sensor 1 and 6.16 for sensor 2. Sensor 2 shows a slightly lower base resistance, but the determined sensor response is the same for both sensors, which are compared with each other in figure 6.17.

To demonstrate the repeatability of the sensor performance, sensor 1 is shown in figure 6.18 at 50 % relative humidity and 350 °C sensor operation temperature, where the sensor is exposed in an alternating mode to 10 ppm and 200 ppm CO.

In the figures 6.19 and 6.20, the sensor response of sensor 1 and sensor 2 at 300 °C and 250 °C is displayed, which shows that the sensors have the same sensitivity at these lower temperatures as at 350 °C. This means that the sensor operation temperature has no significant influence on the sensor response in this temperature range and therefore, the amount of nanowire material is increased for the fabrication of the CMOS MPW4 sensor to reach a higher sensitivity with the enlarged active area.

The gas measurement of the MPW4 sensor with higher nanowire density is shown in figure 6.21 at the sensor operation temperature of 250 °C. The sensor shows high sensitivity, which is compared to the sensor response of sensor 1 and sensor 2 (SB sensor) consisting of less nanowire material in figure 6.22.

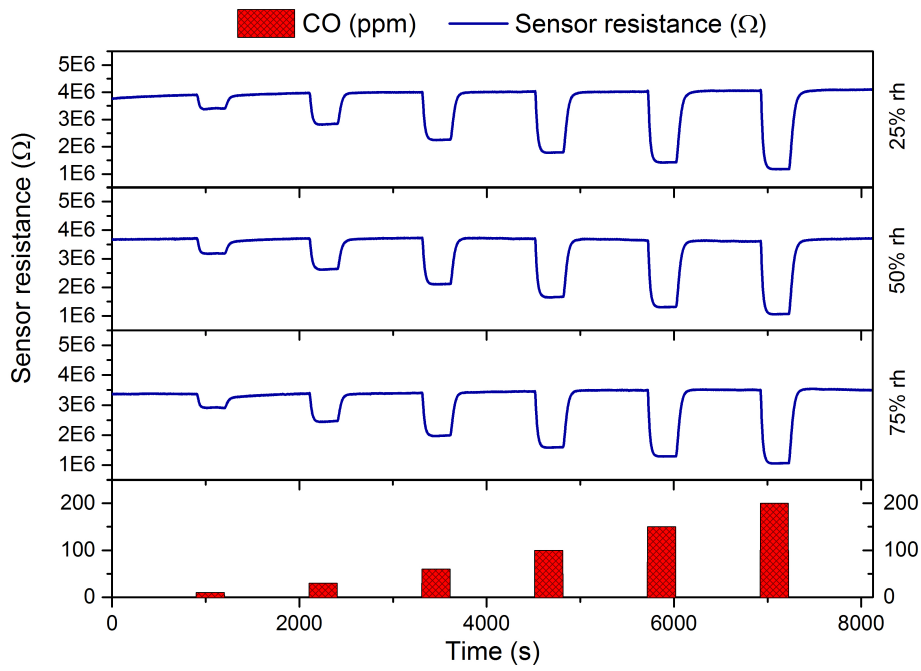


Figure 6.15.: CO gas measurement of sensor 1 at 350 °C and three relative humidity levels exposed to 10 ppm, 30 ppm, 60 ppm, 100 ppm, 150 ppm and 200 ppm CO.

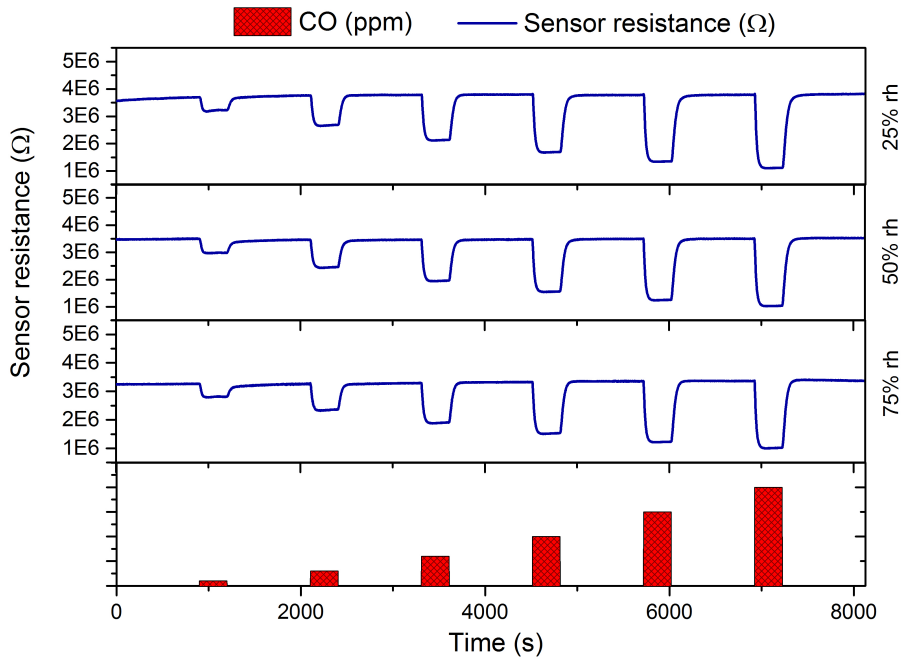


Figure 6.16.: CO gas measurement of sensor 2 at 350 °C and three relative humidity levels exposed to 10 ppm, 30 ppm, 60 ppm, 100 ppm, 150 ppm and 200 ppm CO.

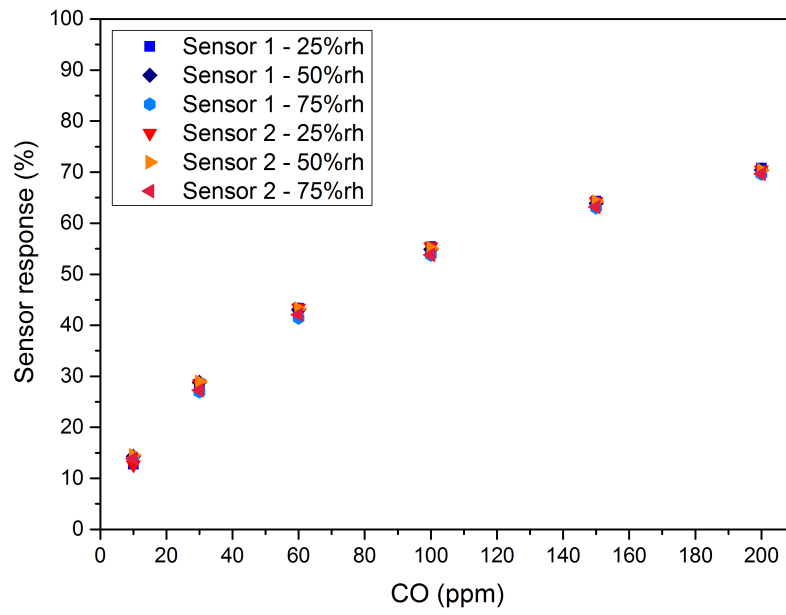


Figure 6.17.: CO gas response of sensor 1 and 2 in (%) at 350 °C at three relative humidity levels.

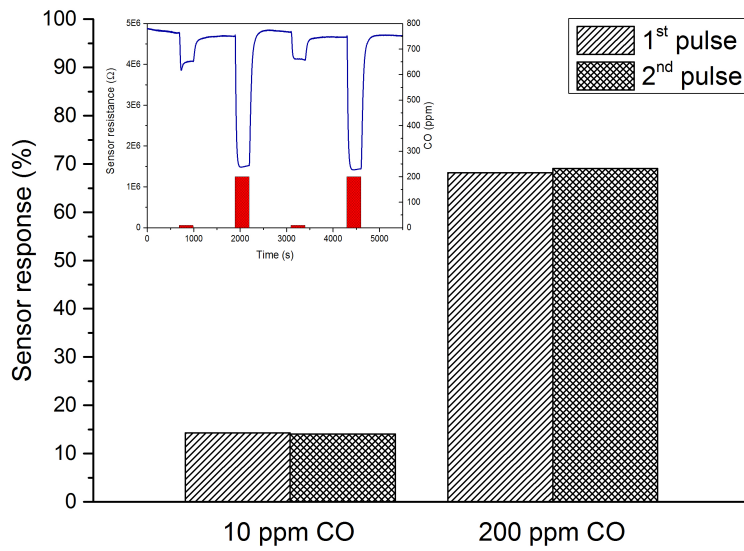


Figure 6.18.: CO gas response in (%) at 350 °C for sensor 1.

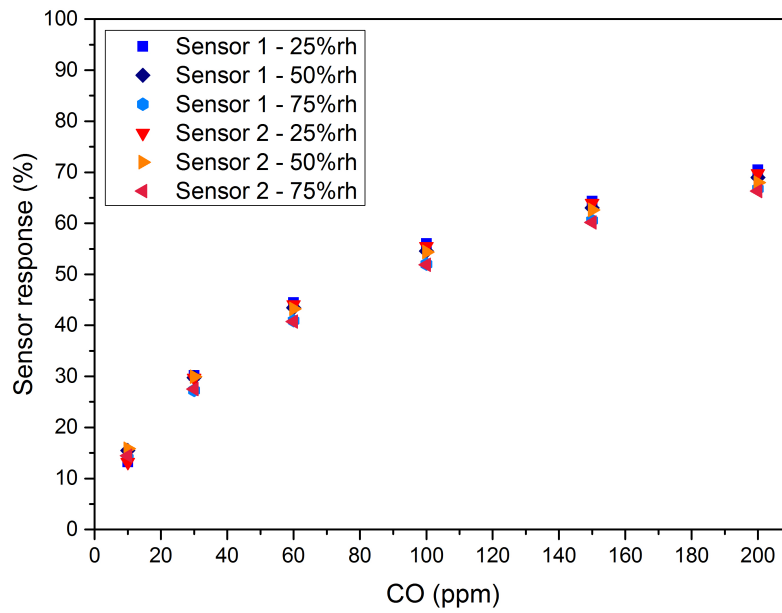


Figure 6.19.: CO gas response of sensor 1 and 2 in (%) at 300 °C at three relative humidity levels.

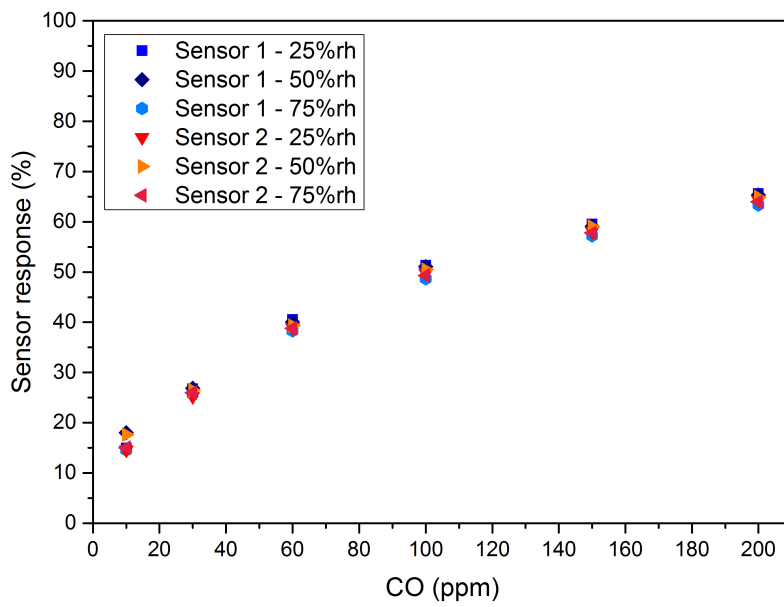


Figure 6.20.: CO gas response of sensor 1 and 2 in (%) at 250 °C at three relative humidity levels.

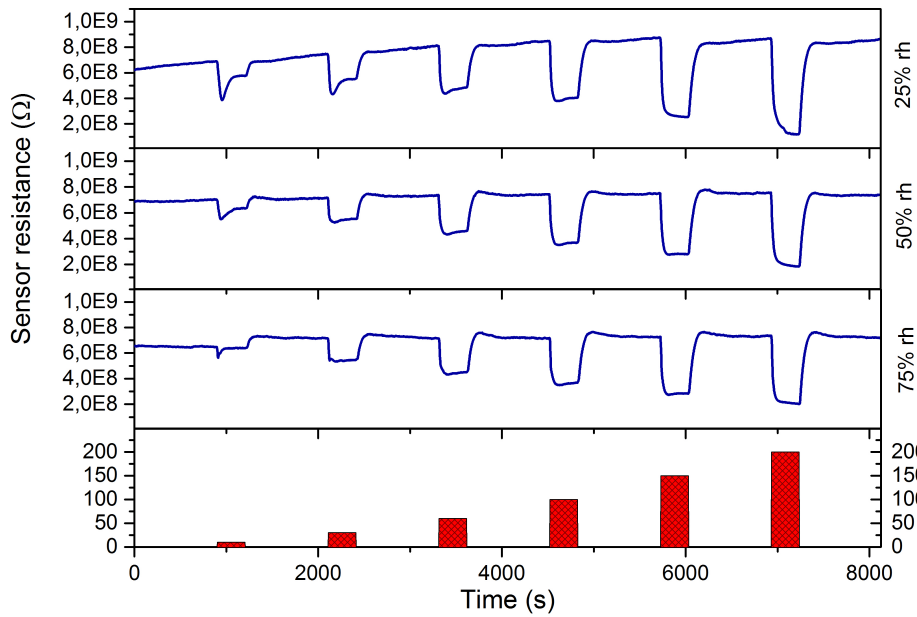


Figure 6.21.: CO gas measurement of CMOS MPW4 sensor at 250 °C and three relative humidity levels exposed to 10 ppm, 30 ppm, 60 ppm, 100 ppm, 150 ppm and 200 ppm CO.

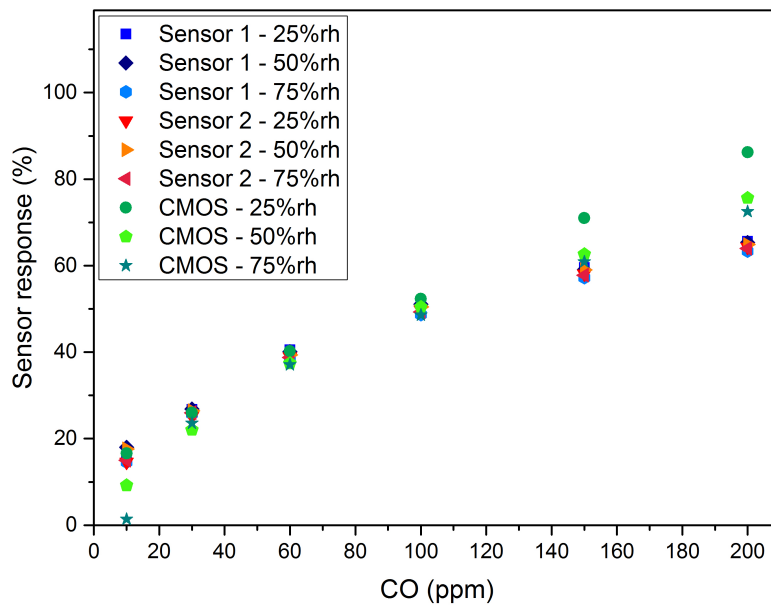


Figure 6.22.: CO gas response in (%) at 250 °C for sensor 1, sensor 2 and the CMOS MPW4 sensor.

The following conclusions can be drawn from the gas sensor evaluation for the exposure to CO:

- The tungsten oxide nanowire material is highly sensitive to CO.
- Sensor 1 and sensor 2 show the same sensor response to the set CO gas pulses, whereby the reproducibility of the sensor fabrication can be shown.
- The sensor is able to detect low and high CO gas concentrations in an alternating mode, which demonstrates the repeatability of the sensor performance.
- The sensor operation temperature has no great influence on the sensor response in the range of 250 °C to 350 °C in the used range of CO gas concentrations.
- The sensor response of the CMOS based sensor with a higher density of tungsten oxide nanowire material slightly deviates from the silicon based sensor.

6.3.4. Sensor response to CO₂

An initial test program is applied to the silicon based tungsten oxide nanowire gas sensor, where the sensor is exposed to various ppm-levels of CO₂ between 500 ppm and 2000 ppm in three relative humidity levels (25 %, 50 % and 75 % at 20 °C) to determine if the sensor is sensitive to CO₂. Since it can be shown that the sensor is not sensitive to CO₂ at the sensor operation temperature of 250 °C and therefore, CO₂ does not affect the H₂S sensing performance (figure 6.14), the sensor material is tested at higher temperatures of up to 400 °C for the above mentioned concentrations of CO₂. The sensor shows a poor change in the sensor resistance while being exposed to CO₂, which means the sensor is sensitive to this target gas, but it has to be evaluated if the sensor response is efficient enough. According to the evaluation of the complete test gas measurement with sensor operation temperatures between 300 °C, 350 °C and 400 °C, the sensitivity of the sensor reaches its maximum at an operation temperature of 400 °C.

The CMOS MPW3mod gas sensor is tested towards CO₂ concentrations of 500 ppm, 1000 ppm, 1500 ppm and 2000 ppm at the operation temperature of 400 °C at the three relative humidity levels (25 %, 50 % and 75 % at 20 °C). Figure 6.23 shows the gas sensor measurement, where the marginal change in the sensor resistance can be seen. Converted to the sensor response (figure 6.24) the sensitivity of the sensor is not even reaching the 5%.

The following conclusions can be drawn from the gas sensor evaluation for the exposure to CO₂:

- The tungsten oxide nanowire sensor is not suitable to efficiently detect CO₂.
- The sensor could be more sensitive at higher sensor operation temperatures, but the CMOS microhotplate chip is limited to 400 °C.

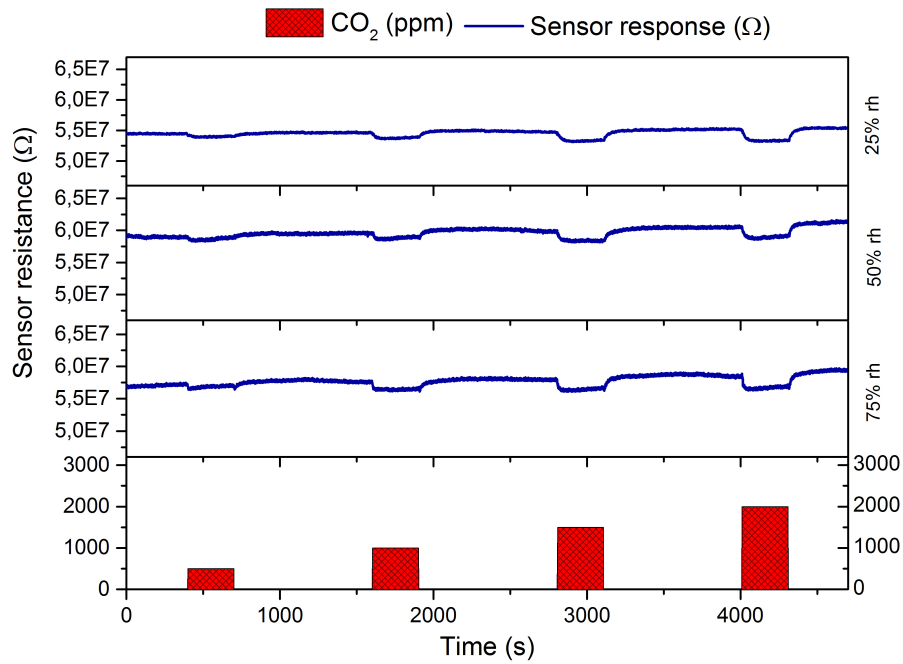


Figure 6.23.: CO₂ gas measurement of CMOS MPW3mod sensor at 400 °C and three relative humidity levels exposed to 500 ppm, 1000 ppm, 1500 ppm and 2000 ppm CO₂.

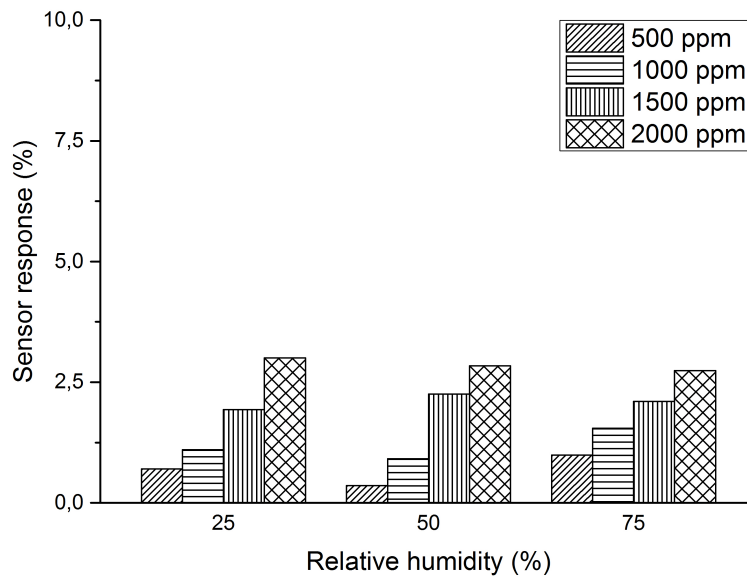


Figure 6.24.: CO₂ gas response of CMOS MPW3mod sensor in (%) at 400 °C at three relative humidity levels.

6.3.5. Sensor response in nitrogen atmosphere

The tungsten oxide nanowire gas sensor shows significant sensitivities to H₂S and CO as presented in the previous sections. All the measurements are conducted in synthetic air and humid atmosphere, where enough oxygen is present to adsorb at the nanowire surface, which leads to the reaction of the target gas molecules with the adsorbed oxygen species. The arising question is, which reactions take place, when no adsorbed oxygen is present at the nanowire surface. To investigate this question, the silicon based sensor (sensor 1) is exposed to H₂S and CO in nitrogen atmosphere. At both measurements, the sensor is first treated at 400 °C for three hours and the lowest humidity level of 3 % (limited by the gas measurement setup) to clean the nanowire surface as good as possible from oxygen species. After this temperature treatment, the sensor was set to the specific sensor operation temperature according to the exposed gas species: 250 °C for the exposure of H₂S and 350 °C for CO.

At the H₂S gas measurement shown in figure 6.25, two gas pulses of 1000 ppb H₂S are applied to the sensor with a pulse duration of five minutes and a break of 15 minutes nitrogen flow in between. A very intensive change in sensor resistance takes place at the first gas pulse. The sensor reacts strongly to the present H₂S gas, but with a low reaction speed. At the end of the first H₂S gas pulse, the sensor resistance has not reached its saturation yet. In the period between the two gas pulses, the sensor resistance goes back slowly to higher resistance values, but within the 15 minutes, the base resistance of the sensor can not be reached. At the second gas pulse, the change in sensor resistance is not as intensive as at the first pulse. After the second gas pulse the sensor resistance gradually increases.

At the CO gas measurement shown in figure 6.26, two gas pulses of 200 ppm CO are applied to the sensor in the same sequence as described for H₂S. The sensor reacts strongly to the gas exposure and reaches its saturation quite fast. After the first gas pulse, the sensor resistance almost reaches its base resistance within the 15 minutes before the second CO gas pulse is introduced into the gas chamber. The sensor resistance drops again, but can not reach the saturation state within the five minutes of CO exposure.

In the tables 6.2 and 6.3 the sensor response for H₂S and CO gas measurements in

synthetic air and nitrogen is presented. It can be seen immediately, that the sensor has a better sensor response to the certain amounts of target gases in nitrogen atmosphere with almost no oxygen present. For H₂S, there is a difference of 40 % in sensor response. For CO, the difference is less, 25 %, which is still a significant value.

In table 6.4, the response times for H₂S and CO gas measurements in nitrogen are summarised and compared to those in synthetic air. First of all, the response times show, that the tungsten oxide nanowire sensor reacts faster to CO than to H₂S. Even if the sensor is operated at 300 °C or 350 °C the response time for 1000 ppb H₂S does not fall below 2 min. In nitrogen, the response time of 3 min 35 s is even higher than in synthetic air. For CO, a different sensor behaviour emerges. The response time for a gas pulse of 200 ppm CO in synthetic air is 48 s and in nitrogen 28 s, hence it can be concluded, that the sensor reacts faster to CO in nitrogen atmosphere than in synthetic air.

In table 6.5, the recovery times for H₂S and CO gas measurements in nitrogen are presented, again compared to those in synthetic air. For the H₂S gas measurement in synthetic air, a recovery time of 1 min 57 s can be calculated, but the sensor resistance can not reach the base resistance within the given time of fifteen minutes (set by the measurement program, see section 6.2.2). After the fifteen minutes, the sensor shows a resistance 98 % of the base resistance value. In the H₂S gas measurement in nitrogen atmosphere, the sensor resistance increases gradually after the second gas pulse of 1000 ppb, with a recovery time of 1 h 46 min. After two hours the sensor still does not reach its base resistance but 94 % of it. For CO, the same trend of a higher recovery time in nitrogen atmosphere than in synthetic air is shown in table 6.5, but the range of the recovery times is within one to eight minutes.

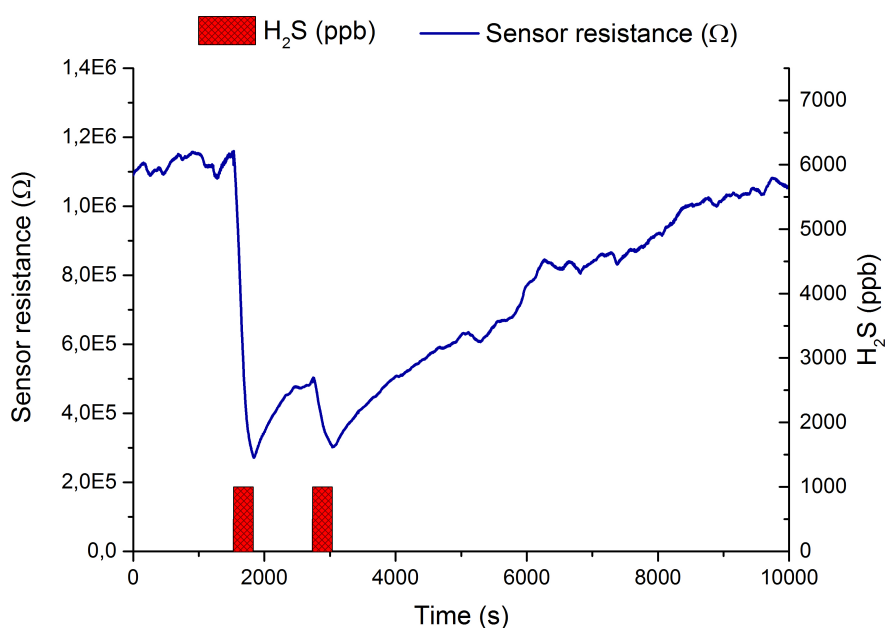


Figure 6.25.: H₂S gas measurement at 250 °C in nitrogen atmosphere with a gas pulse concentration of 1000 ppb H₂S and a relative humidity level of 3% (limited by the gas measurement setup).

Table 6.2.: Sensor response (%) of H₂S gas measurement in synthetic air (SA) and nitrogen (N₂); the sensor response value for the measurement in SA is a mean value of the three relative humidity levels of 25%, 50% and 75% and the sensor response value for the measurement in N₂ is calculated for the first gas pulse.

Target gas	Carrier gas	Sensor operation temperature	Gas concentration	Relative humidity	Sensor response
H ₂ S	SA	250 °C	1000 ppb	25–75 %	30.66 %
H ₂ S	N ₂	250 °C	1000 ppb	3 %	70.61 %

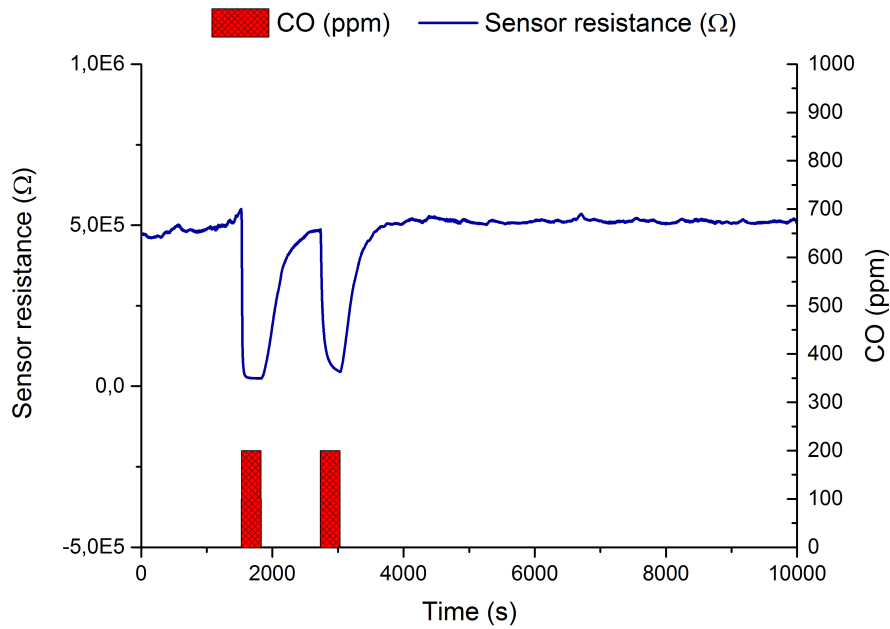


Figure 6.26.: CO gas measurement at 350 °C in nitrogen atmosphere with a gas pulse concentration of 200 ppm CO and a relative humidity level of 3 % (limited by the gas measurement setup).

Table 6.3.: Sensor response (%) of CO gas measurements in synthetic air (SA) and nitrogen (N₂); the sensor response value for the measurement in SA is a mean value of the three relative humidity levels of 25%, 50% and 75% and the sensor response value for the measurement in N₂ is calculated for the first gas pulse.

Target gas	Carrier gas	Sensor operation temperature	Gas concentration	Relative humidity	Sensor response
CO	SA	350 °C	200 ppm	25–75 %	70.28 %
CO	N ₂	350 °C	200 ppm	3 %	95.54 %

Table 6.4.: Response times (t_{resp}) of H₂S and CO gas measurements in synthetic air (SA) and nitrogen (N₂); t_{resp} for measurements in SA are mean values of the three relative humidity levels of 25 %, 50 % and 75 % and the t_{resp} for measurements in N₂ are calculated for the first gas pulse.

Target gas	Carrier gas	Sensor operation temperature	Gas concentration	Relative humidity	t_{resp}
H ₂ S	SA	250 °C	1000 ppb	25–75 %	2 min 19 s
H ₂ S	N ₂	250 °C	1000 ppb	3 %	3 min 35 s
CO	SA	350 °C	200 ppm	25–75 %	48 s
CO	N ₂	350 °C	200 ppm	3 %	28 s

Table 6.5.: Recovery times (t_{recov}) of H₂S and CO gas measurements in synthetic air (SA) and nitrogen (N₂); t_{recov} for measurements in SA are mean values of the three relative humidity levels of 25 %, 50 % and 75 % and the t_{recov} for measurements in N₂ are calculated for the second gas pulse.

Target gas	Carrier gas	Sensor operation temperature	Gas concentration	Relative humidity	t_{recov}
H ₂ S	SA	250 °C	1000 ppb	25–75 %	1 min 57 s
H ₂ S	N ₂	250 °C	1000 ppb	3 %	1 h 46 min
CO	SA	350 °C	200 ppm	25–75 %	1 min 17 s
CO	N ₂	350 °C	200 ppm	3 %	7 min 30 s

6.4. Discussion

In this section the sensor performance of the tungsten oxide nanowires towards H₂S and CO is discussed regarding the influence of the operation temperature, the different humidity levels, the used background gases, synthetic air and N₂, and the exposed target gas concentrations. The detection of CO₂ is not included in the discussion, because the tungsten oxide nanowire gas sensor is not sufficiently sensitive to CO₂ in the feasible temperature range up to 400 °C, which is as described above limited by the CMOS microhotplate chip.

6.4.1. Influence of sensor operation temperature

The sensor operation temperature is an important influence factor for metal oxide gas sensing. For H₂S gas sensing of the tungsten oxide nanowire sensor device, 300 °C is determined to be the sensor operation temperature with the highest sensor response. The response profile for H₂S, as presented in figure 6.7, shows that operation temperatures higher than 300 °C lower the sensor response. This behaviour of having an optimum sensor operation temperature for a certain target gas is explained in [168, 169] by a competitive situation between slow kinetics of the reaction with the target gas at lower sensor operation temperatures and desorption processes promoted by higher temperatures. For the target gas CO, this characteristic behaviour can not be confirmed for the tungsten oxide nanowire sensor, within the used temperature range of 250 °C to 350 °C. The sensor shows similar responses at all three sensor operation temperatures. A maximum deviation of less than 5% can be calculated for all three sensor operation temperatures at all applied target gas concentrations and humidity levels. The sensor operation temperature has no great influence on the sensor response when exposed to CO, but the influence on the response and recovery time is obvious from the figures 6.27 and 6.28.

6.4.2. Influence of humidity

The humidity present in the sensor environment can severely influence the sensing performance of a metal oxide gas sensor, as described in section 6.1.1. The H₂S gas sensor at 300 °C sensor operation temperature clearly shows an influence of the humidity level on the sensor performance (figure 6.9). The sensor response decreases almost 20 % (at 1000 ppb H₂S) from the lowest level of 25 % relative humidity to the highest level of 75 % relative humidity. This behaviour of metal oxide gas sensors in the presence of water molecules is extensively studied and reported in literature [155,168]. Competitive reactions of the metal oxide with the water molecules lead to the decrease in sensor response with increasing humidity level, like it is the case for the tungsten oxide nanowire sensor detecting H₂S. At 250 °C sensor operation temperature, this competition between water molecules and H₂S target molecules seems to be in an equilibrium state, where less active sites are available for the reaction with H₂S, which results in a lower sensor response, but the quantity of water molecules do not affect the sensor performance.

For the detection of CO, humidity seems to affect the sensor not at all. At all three used sensor operation temperatures (250 °C, 300 °C, 350 °C), the humidity influence is negligibly low. Except the CMOS MPW4 sensor with the higher amount of deposited nanowires, which shows a slight influence of the different humidity levels (figure 6.22). At the lowest concentration of 10 ppm CO the deviation of the three sensor responses is about 15 %. At the concentrations from 30 ppm to 100 ppm, no significant difference in sensor response can be reported, but at 150 ppm and 200 ppm the deviation of the sensor responses becomes larger, also around 15 %. This leads to the assumption that too much of the nanowire material could cause problems with humidity interferences. But to truly understand the effect of humidity in the cases of H₂S and CO gas sensing with the fabricated tungsten oxide nanowire gas sensors, the kinetics of the sensor mechanisms have to be studied in more detail and a certain amount of identical sensors has to be analysed, which is not feasible within the framework of this work.

6.4.3. Influence of target gas concentration

The H₂S gas measurement results of the tungsten oxide nanowire gas sensor in section 6.3.2 show that the sensor detects H₂S with a satisfying sensor response, which increases with increasing target gas concentration. When the shape of the resistance changes is analysed, it can be seen that the sensor does not reach a saturation state over the exposure time of five minutes at none of the exposed gas concentrations, which is in agreement with the slow response time of several minutes presented in figure 6.12 and table 6.4. These findings lead to the assumption, that not just reactions with adsorbed oxygen species take place at the nanowire network surface, but also competitive reactions, which have no effect on the material's resistance. A competitive reaction could be the formation of WS₂ as described in equation 6.9. In this reaction, WO₃ and H₂S are reacting with each other and form WS₂, SO₂ and water. SO₂ is a pungent-smelling and toxic gas, which can be detected by tungsten oxide and other metal oxide gas sensors as well as H₂S [170]. So the formation of WS₂ and SO₂ would lead to a changed composition of the gas environment, where both gas species, H₂S and SO₂, are present. The resulting concern is, that SO₂ is also reacting with the tungsten oxide nanowire surface and therefore distorts the gas measurement of H₂S. If this is the case, the detection of H₂S is even more difficult to interpret and evaluate. The formation of WS₂ would also explain the fact that the sensor resistance can not completely recover to the base resistance value after exposure to H₂S.

The CO gas measurements in section 6.3.3 show the tungsten oxide nanowire gas sensor detecting CO with very good performance. The sensor reaches the saturation state, immediately after the exposure to the target gas starts, and the sensor response increases with increasing CO gas concentration, as desired. As presented in figure 6.27, the CO gas concentration has no relevant effect on the response times at the three applied sensor operation temperatures. The deviating value at 10 ppm and 250 °C with 50 % relative humidity (rh) is due to troubles in the humidity configurations, therefore this value should be excluded from the interpretation of the results. It can be shown that the response times are not effected by the amount of gas molecules reacting with the surface in this range of target gas concentrations. In contrast to that, the recovery times shown

in figure 6.28 are significantly increased with the increasing CO concentration. It seems, that reaction processes of CO with the nanowire network surface are much faster than the recovery period. The recovery could consist of the adsorption of oxygen species or the reoxidation of the tungsten oxide itself. The comparison of response and recovery times of the tungsten oxide nanowire gas sensor with other nanowire network sensors in literature shows, that the sensor fabricated in this work provides properties in the same time range [171–173].

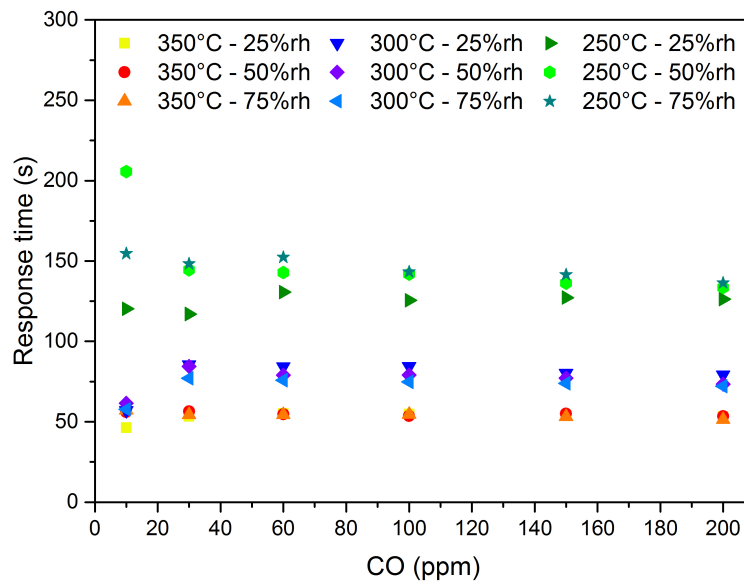


Figure 6.27.: Response time in (s) of CO gas measurement (sensor 1) at three different sensor operation temperatures.

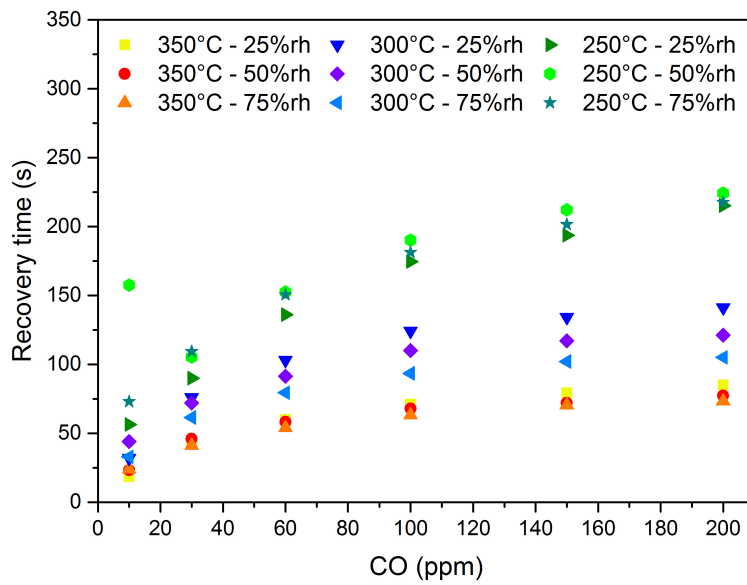


Figure 6.28.: Recovery time in (s) of CO gas measurement (sensor 1) at three different sensor operation temperatures.

6.4.4. Influence of background gas

In the broad spectrum of applications for gas sensors, the more likely gas atmosphere is ambient air, but to get more information about the sensor mechanisms themselves, experiments with N_2 as background gas are performed. In the tables 6.2 and 6.3, the sensor response of the tungsten oxide nanowire gas sensor to the target gases H_2S and CO in synthetic air and N_2 is presented. The trend for both target gas species is that the sensor response is higher in N_2 atmosphere than in synthetic air. At H_2S , the difference in sensor response is almost 40 %, at CO 25 %. This behaviour of higher sensor responses, when no or a low level of oxygen is present, can be confirmed by the report of Hahn et al. for SnO_2 thick films [162].

The evaluation of the response and recovery times (tables 6.4 and 6.5) shows first of all, that the H_2S sensor reactions proceed extremely slow, no matter in which background gas. As already discussed above, it can be presumed that H_2S reacts with the tungsten oxide nanowires in multiple ways: The reversibility of the resistance decrease shows that typical metal oxide sensor reactions take place, but the base resistance does not reach the initial resistance value after H_2S exposure, which indicates an irreversible reaction of H_2S and tungsten oxide like described in equation 6.9.

In the case of CO, the sensor reacts in N_2 atmosphere almost twice as fast as in synthetic air. This behaviour could be explained by the reaction mechanism shown in equation 6.10, where CO adsorbs to the surface and acts as an electron donor, in the absence of oxygen. But also lattice oxygen could react with the CO molecules forming oxygen vacancies (equation 6.11). The latter would lead to higher response and recovery times in bulk materials, because of diffusion of the oxygen vacancies into the bulk, but in the case of nanowires smaller dimensions are present. Concerning the recovery time, an opposite trend emerges, where the recovery of the sensor takes more time in N_2 atmosphere than in synthetic air. This would more likely point out the reaction of CO with lattice oxygen, where reoxidation process of the reduced tungsten oxide nanowire network takes time, especially because a very low amount of oxygen is present.

6.5. Summary

The CMOS tungsten oxide nanowire gas sensors are tested to detect H₂S, CO and CO₂. For the exposure to H₂S and CO, the sensors show good sensor response, whereas the exposure to CO₂ shows a sensor response less than 5%.

The H₂S gas measurement evaluations show that the tungsten oxide nanowire sensor has a good response up to almost 60 % (for the exposure to 1000 ppb H₂S) at the sensor operation temperature of 300 °C. Unfortunately, the sensor exhibits a high cross sensitivity to humidity at this sensor operation temperature. Therefore, the lower temperature of 250 °C is evaluated, where almost no cross sensitivity to humidity can be found, with the drawback of a lower sensor response (30 % at 1000 ppb H₂S). Further can be seen, that CO₂ is not interfering with the detection of H₂S. Although the tungsten oxide nanowires are highly sensitive to H₂S, the analysed response and recovery times in figure 6.12 as well as in the tables 6.4 and 6.5 are too long for an application as gas sensor, where a fast alert is crucial by exposure to a hazardous gas like H₂S. Additional to the slow sensor response and recovery, it is assumed, that H₂S reacts with the tungsten oxide nanowires and irreversibly forms WS₂. This is indicated by the fact, that the base resistance can not be reached again after the exposure to H₂S. Thus the question arises, if SO₂, which results from the formation of WS₂, is also reacting with the nanowire surface or not.

The evaluation of the CO gas measurements shows that the fabrication process of inkjet printing is reproducible, so that the two identical sensors 1 and 2 can be fabricated. The sensor response of the two sensors is in good agreement, independent from the applied temperatures in the range of 250 °C to 350 °C (figures 6.17, 6.19 and 6.20). The repeatability of gas detection is also presented, where a low amount of 10 ppm and a high amount of 200 ppm CO is applied in an alternating mode to the sensor. The calculated sensor response in figure 6.18 shows well correlating data for the detection of alternating target gas pulses. The fabricated CMOS MPW4 sensor, with a higher nanowire network density, shows a slightly deviating sensor response to the SB sensor, which could be due to humidity interferences. The presented sensor response in nitrogen atmosphere indicates the different reaction mechanisms depending on the amount of oxygen species adsorbed at the nanowire surface. When almost no oxygen is present in the gas sensor

atmosphere, it is assumed that the CO molecules adsorb to the tungsten oxide and act as donor, or react directly with the lattice oxygen and reduce the tungsten oxide.

Additionally can be shown, that the tungsten oxide nanowire sensor is insensitive to the exposure of CO₂, because the sensor response of less than 5 % is not suitable to efficiently detect the target gas and can be neglected.

The overall evaluation of the tungsten oxide nanowire gas sensors results in the fact, that the metal oxide nanowire material is an excellent CO gas sensor with an outstanding sensor response and fast response and recovery times.

7. Conclusion & Outlook

The objective of this thesis is the fabrication of CMOS integrated nanowire gas sensors. The technological methods to integrate nanowires onto CMOS microhotplates are discussed and the feasibility of the used inkjet printing technique is shown. The CMOS integrated tungsten oxide nanowire gas sensors can be realised.

The tungsten oxide nanowires are hydrothermally synthesised and investigated by different characterisation methods in terms of material properties and chemical composition. The gas sensing properties of the sensor material are studied with a test sensor (SB sensor) and the CMOS integrated devices in terms of sensitivity to the different target gases H_2S , CO and CO_2 , the cross-sensitivity to humidity and the sensor response and recovery times.

The hydrothermal synthesis of the tungsten oxide nanowires represents a simple and low-cost technique, without the usage of any hazardous reactants. Furthermore, the moderate reaction temperature of 180°C requires no expensive heating equipment. The potassium sulphate, which is acting as a shaping agent in the nanowire growth, can be even recycled at the end of the reaction. The hydrothermal synthesis of tungsten oxide nanowires demonstrates a promising way to scale up the sensor material production, even to industrial scale.

The synthesised tungsten oxide nanowires are investigated by several analysis methods. SEM and TEM are used to get more information about the material morphology and geometry. The resulting images showed nanowires with high aspect ratios up to 1000 with a fibrous looking texture. By high resolution TEM and SAED characteristic lattice constants can be identified, which refer to a non stoichiometric tungsten oxide nanowire material. The XRD spectrum recorded from the nanowire powder is in best agreement with the hexagonal stoichiometric WO_3 published by Oi et al. [110]. The EDX is used as chemical characterisation method, which shows that the nanowires consist of the expected elements tungsten and oxygen, but also a certain amount of potassium is present in the nanowires. The Raman investigations are not significant for the determination of the nanowire composition, but can show that a temperature induced transformation of the nanowires occurs. By the use of these available investigation methods, no clear

statement about the tungsten oxide nanowire composition or crystal structure of the nanowires can be given. Further investigations will have to be conducted, which could give more precise chemical information about the nanowires, for example electron probe micro analysis (EPMA) to exactly determine the chemical composition or X-ray photo electron spectroscopy (XPS) to identify the electronic state of tungsten.

The integration of the tungsten oxide nanowires onto the CMOS microhotplates is realised by the use of a FUJIFILM inkjet printer [139]. A water based nanowire suspension is homogenised by ultrasonication and filled in the printer cartridge, which is mounted on the printer. With the precisely adjustable sample stage and camera system, the nanowire suspension is deposited on the designated CMOS microhotplate positions. This is a simple nanowire deposition technique, which can be applied to any substrate with an accurate reproducibility. The printing process is not specific for the tungsten oxide nanowire material, so the composition of the nanowire suspension is flexible and can be arbitrary adapted.

The gas sensing properties of the printed CMOS tungsten oxide nanowire sensors are analysed for the exposure to H_2S , CO and CO_2 . The evaluation shows, that the sensor material is sensitive to H_2S and CO producing a satisfying sensor response, but the exposure of CO_2 affects no significant change in the materials resistance. The drawback in the detection of H_2S is the slow response time of several minutes, which is not feasible for a real life gas detector. But the fabricated gas sensors show a highly effective CO sensing performance: sensor response up to 70 % with response times of a few seconds and no cross-sensitivity to humidity. Also the repeatability of the CO detection can be shown by the exposure of the sensor to the lowest and highest CO concentrations, used in the measurement procedure, in an alternating mode. Therefore, the fabricated CMOS tungsten oxide nanowire gas sensor turns out to be an excellent CO detector.

In the future, the CMOS nanowire gas sensors fabricated in this work can be refined in different aspects:

- The nanowire material can be functionalised with metallic nanoparticles to improve the gas sensing properties. The metallic nanoparticles have a catalytic effect on the dissociation of the adsorbing target gas molecules and therefore enhance the

sensitivity of the sensor to certain gases. The functionalisation can also have an influence on reaction speeds, which means that sensor response times can be reduced in this way.

- The nanowire integration on the CMOS chip or any other substrates can be improved by the adjustment of the printing process to the nanowire printing application. A suggestion for a nanowire printer on industrial scale is given.
- The fabricated tungsten oxide nanowire gas sensor can be combined with other nanowire gas sensors by the use of the unique CMOS MPW4 chip, which consists of eight well-designed microhotplates, which can be operated in parallel. This will lead to a CMOS sensor array, where multiple different gas sensors are located on one single chip.

These three aspects will be discussed in detail in the following sections as an outlook to future improvements of the CMOS integrated nanowire gas sensors.

Outlook for sensor material optimisation

The combination of metallic nanostructures like nanoparticles and metal oxide nanowires can optimise the sensing performance of gas sensors. This method of sensor improvement is well reported and accepted in literature [174–177]. Therefore, the tungsten oxide nanowires synthesised in this work are functionalised with bimetallic nickel platinum nanoparticles within the project "RealNano - Industrielle Realisierung innovativer CMOS basierter Nanosensoren" (Grant No. 843598). The project partner and nanotechnology expert CAN GmbH synthesises the nanoparticles and by the use of a simple mixing technique the nanoparticles attach to the tungsten oxide nanowires. The resulting nanoparticle functionalised nanowires are characterised by TEM, which is shown in figure 7.1. The nanoparticles with a size of around 3 nm are well distributed all over the nanowire network. The interface between the nanoparticle and the nanowire will be analysed by a cross section of the nanowire in upcoming TEM experiments. The gas sensing properties of the material combination are currently under investigation.

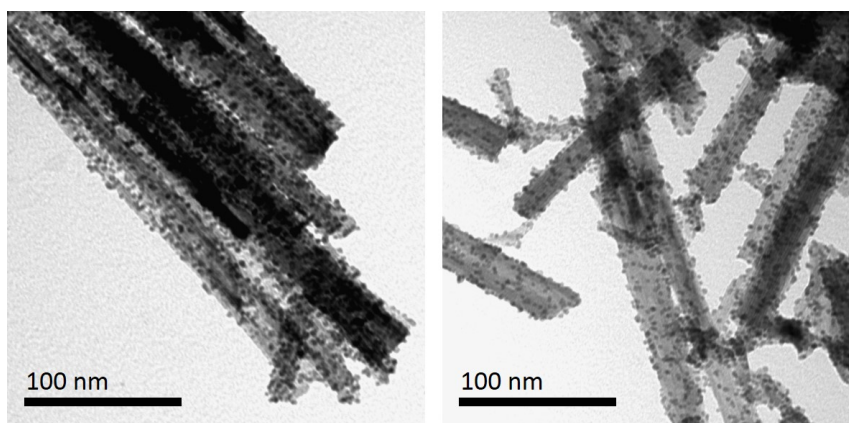


Figure 7.1.: TEM images of tungsten oxide nanowires functionalised with bimetallic nickel platinum (NiPt) nanoparticles.

Outlook for nanowire integration

The inkjet printing technique is suitable for the sensor fabrication in this work, but if the quantity of sensors to produce increases, a straightforward inkjet printer will not fulfil the production requirements. Therefore, an idea, how the realisation of such a nanowire printing tool can look like, is presented in figure 7.2. The nanowire suspension is either stirred or ultrasonicated to achieve the homogeneous distribution in the liquid phase. The nanowire suspension is transferred continuously to the head of the printer, where a piezo-driven or another dispensing technique is used to form a droplet of the required size. The droplet is deposited at the desired position on the CMOS wafer. In this way, microhotplates on the entire CMOS wafer can be coated with a certain nanowire material.

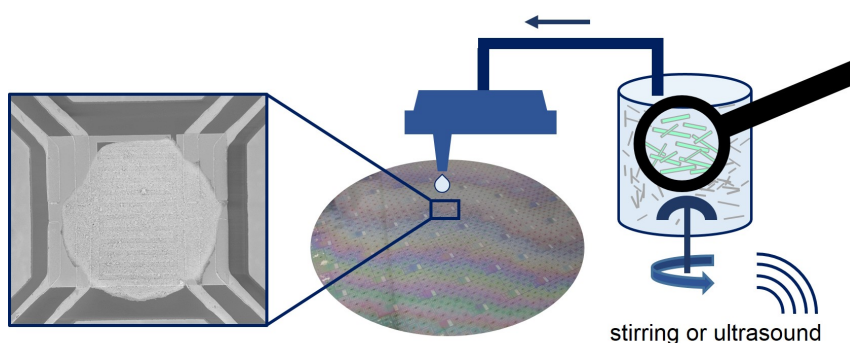


Figure 7.2.: Scheme of potential nanowire printing tool.

Outlook for unique CMOS integrated sensor array

The combination of the nanowire sensor printing and the CMOS MPW4 microhotplate chip design offers the possibility to create unique CMOS sensor arrays, where on each of the eight available microhotplates another nanowire material can be deposited. A possible nanowire combination can be tungsten oxide, tin oxide and copper oxide as shown in figure 7.3. Also other nanowire materials or nanowire-nanoparticle combinations can be part of the sensor array. This unique sensor array is expected to be able to distinguish between different gas species by the diverse materials being sensitive to specific target gases and a well-designed software supporting and evaluating the obtained data.

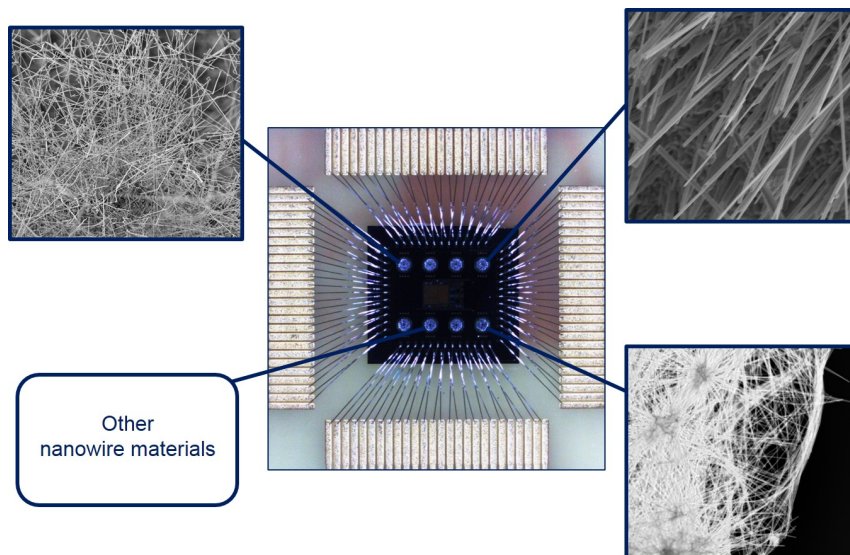


Figure 7.3.: Nanowire sensor array on CMOS MPW4 microhotplate chip with eight microhotplates.

List of Abbreviations

AAM	Anodic Aluminium Membrane
ALD	Atomic Layer Deposition
CMOS	Complementary Metal Oxide Semiconductor
CVD	Chemical Vapour Deposition
EDX	Energy Dispersive X-ray Spectroscopy
EPMA	Electron Probe Micro Analysis
FFT	Fast Fourier Transformation
MBE	Molecular Beam Epitaxy
MFC	Mass Flow Controller
MPW	Multi Project Wafer
NTS BSD	Backscattered Electron Detector
rh	Relative Humidity
SAM	Self Assembled Monolayer
SB	Silicon Based
SE2	Secondary Electron Detector
SEM	Scanning Electron Microscopy
SMU	Source Measure Unit
TEM	Transmission Electron Microscopy
TSV	Through Silicon Via
XPS	X-ray Photo Electron Spectroscopy
XRD	X-ray Diffraction

Bibliography

- [1] Bundeskanzleramt Rechtsinformationssystem. <https://www.ris.bka.gv.at/>.
- [2] K. Sasaki, K. Susuki, A. Iyoshi, M. Uchimura, N. Imamura, H. Kusaba, Y. Teraoka, H. Fuchino, K. Tsujimoto, Y. Uchida, and N. Jingo. H₂S poisoning of solid oxide fuel cells. *Journal of the Electrochemical Society*, 153(11):A2023–A2029, 2006.
- [3] CO₂.earth. <https://www.co2.earth/>.
- [4] T. Seiyama, A. Kato, K. Fujiishi, and M. Nagatani. A new detector for gaseous components using semiconductive thin films. *Analytical Chemistry*, 34:1502–1503, 1962.
- [5] G. Fine, L. Cavanagh, A. Afonja, and R. Binions. Metal oxide semi-conductor gas sensors in environmental monitoring. *Sensors*, 10(6):5469–502, 2010.
- [6] P. Kofstad. *Nonstoichiometry, Diffusion and Electrical Conductivity in Binary Metal Oxides*. Wiley-Interscience, 1972.
- [7] E. H. Nicollian and J. R. Brews. *MOS (Metal Oxide Semiconductor) Physics and Technology*. Wiley, 1982.
- [8] B. Sapoval and C. Hermann. *Physics of Semiconductors*. Springer, 1995.
- [9] H. Bentarzi. *Transport in Metal-Oxide-Semiconductor Structures*. Springer, 2011.
- [10] R. Schmidt, A. M. F. Benial, and D. D. Antia. *Advanced Environmental Analysis: Applications of Nanomaterials Volume 2*. Royal Society of Chemistry, 2016.
- [11] N. Barsan, M. Hübner, and U. Weimar. Conduction mechanisms in SnO₂ based polycrystalline thick film gas sensors exposed to CO and H₂ in different oxygen backgrounds. *Sensors and Actuators, B: Chemical*, 157:510–517, 2011.
- [12] A. Gurlo. Insights into the Mechansim of Gas Sensor Operation. In *Metal Oxide Nanomaterials for Chemical Sensors*, chapter 1. Springer Science+Business, 2013.

- [13] N. Barsan and U. Weimar. Conduction Model of Metal Oxide Gas Sensors. *Journal of Electroceramics*, 7(3):143–167, 2001.
- [14] J. Vetelino and R. Aravind. *Introduction to Sensors*. CRC Press Inc, 2010.
- [15] E. Brunet, T. Maier, G. C. Mutinati, S. Steinhauer, A. Köck, C. Gspan, and W. Grogger. Comparison of the gas sensing performance of SnO₂ thin film and SnO₂ nanowire sensors. *Sensors and Actuators, B: Chemical*, 165(1):110–118, 2012.
- [16] A. Fioravanti, A. Bonanno, S. Gherardi, M. C. Carotta, and A. N. Skouloudis. A portable air-quality station based on thick film gas sensors for real time detection of traces of atmospheric pollutants. *IOP Conference Series: Materials Science and Engineering*, 108(1):012005, 2016.
- [17] T. Becker, S. Ahlers, C. Bosch-v.Braunmühl, G. Müller, and O. Kiesewetter. Gas sensing properties of thin- and thick-film tin-oxide materials. *Sensors and Actuators, B: Chemical*, 77(1-2):55–61, 2001.
- [18] N. Barsan, M. Schweizer-Berberich, and W. Göpel. Fundamental and practical aspects in the design of nanoscaled SnO₂ gas sensors: a status report. *Fresenius Journal Of Analytical Chemistry*, 365(4):287–304, 1999.
- [19] G. Sberveglieri. Classical and novel techniques for the preparation of SnO₂ thin-film gas sensors. *Sensors and Actuators, B: Chemical*, 6:239–247, 1992.
- [20] H. Meixner, J. Gerblinger, U. Lampe, and M. Fleischer. Thin-film gas sensors based on semiconducting metal oxides. *Sensors and Actuators, B: Chemical*, 23:119–125, 1995.
- [21] G. Cao. *Nanostructures and Nanomaterials - Synthesis, Properties and Applications*, volume 2. Imperial College Press, 2004.
- [22] A. Tischner, T. Maier, C. Stepper, and A. Köck. Ultrathin SnO₂ gas sensors fabricated by spray pyrolysis for the detection of humidity and carbon monoxide. *Sensors and Actuators, B: Chemical*, 134(2):796–802, 2008.

- [23] G. C. Mutinati, E. Brunet, S. Steinhauer, A. Köck, J. Teva, J. Kraft, J. Siegert, F. Schrank, and E. Bertagnolli. CMOS-integrable ultrathin SnO₂ layer for smart gas sensor devices. *Procedia Engineering*, 47:490–493, 2012.
- [24] R. Wimmer-Teubenbacher, S. Steinhauer, O. von Sicard, E. Magori, J. Siegert, K. Rohrer, C. Gspan, W. Grogger, and A. Köck. Gas Sensing Characterisation of CMOS Integrated Nanocrystalline SnO₂ – Au Thin Films. *Materials Today: Proceedings*, 2(8):4295–4301, 2015.
- [25] E. Lackner, J. Krainer, R. Wimmer-Teubenbacher, F. Sosada, M. Deluca, J. Bekacz, E. Laubender, O. Yurchenko, G. Urban, K. Rohrer, E. Wachmann, and A. Koeck. CMOS integrated tin dioxide gas sensors functionalized with bimetallic nanoparticles for improved carbon monoxide detection. In *IEEE Sensors 2016*, pages 74–76, 2016.
- [26] L. Gmelin. *Handbuch der anorganische Chemie (Band 46)*. Verlag Chemie ed., 1972.
- [27] R. Chamberlin and J. S. Skarman. Chemical spray deposition process for inorganic films. *Journal of Electrochemical Society*, 113(1):86–89, 1966.
- [28] M. D. Blešić, Z. V. Šaponjić, J. M. Nedeljković, and D. P. Uskoković. TiO₂ films prepared by ultrasonic spray pyrolysis of nanosize precursor. *Materials Letters*, 54(4):298–302, 2002.
- [29] F. Paraguay D., W. Estrada L., D. R. Acosta N., E. Andrade, and M. Miki-Yoshida. Growth, structure and optical characterization of high quality ZnO thin films obtained by spray pyrolysis. *Thin Solid Films*, 350(1):192–202, 1999.
- [30] F. Hernandez-Ramirez, J. D. Prades, and A. Cirera. Nanosensors: A platform to model the sensing mechanisms in metal oxides. In *Chemical Sensors - Simulation and modeling Vol.2: Conductometric-type sensors*, chapter 3. Momentum Press, 2012.
- [31] F. Hernandez-Ramirez, J. D. Prades, R. Jimenez-Diaz, T. Fischer, A. Romano-Rodriguez, S. Mathur, and J. R. Morante. On the role of individual metal oxide

- nanowires in the scaling down of chemical sensors. *Physical Chemistry Chemical Physics*, 11(33):7105–10, 2009.
- [32] R. G. Hobbs, N. Petkov, and J. D. Holmes. Semiconductor Nanowire Fabrication by Bottom-Up and Top-Down Paradigms. *Chemistry of Materials*, 24:1975–1991, 2012.
- [33] F. Hernandez-Ramirez, J. D. Prades, A. Tarancon, S. Barth, O. Casals, R. Jiménez-Díaz, E. Pellicer, J. Rodríguez, M. A. Juli, A. Romano-Rodríguez, J. R. Morante, S. Mathur, A. Helwig, J. Spannhake, and G. Mueller. Portable microsensors based on individual SnO₂ nanowires. *Nanotechnology*, 18(49):495501, 2007.
- [34] O. Lupan, L. Chow, Th Pauporté, L. K. Ono, B. Roldan Cuenya, and G. Chai. Highly sensitive and selective hydrogen single-nanowire nanosensor. *Sensors and Actuators, B: Chemical*, 173:772–780, 2012.
- [35] S. Steinhauer, V. Singh, C. Cassidy, C. Gspan, W. Grogger, M. Sowwan, and A. Köck. Single CuO nanowires decorated with size-selected Pd nanoparticles for CO sensing in humid atmosphere. *Nanotechnology*, 26(17):175502, 2015.
- [36] O. Lupan, G. Chai, and L. Chow. Novel hydrogen gas sensor based on single ZnO nanorod. *Microelectronic Engineering*, 85(11):2220–2225, 2008.
- [37] E. Riedel and C. Janiak. *Anorganische Chemie*. de Gruyter, 7th edition, 2007.
- [38] Mineralienatlas. <https://www.mineralienatlas.de/>.
- [39] 3D-ChemTube - University of Liverpool. <http://www.chemtube3d.com/>.
- [40] G. D. Rieck. *Tungsten and Its Compounds*. Pergamon Press Ltd, 1967.
- [41] M. Boulova and G. Lucazeau. Crystallite nanosize effect on the structural transitions of WO₃ studied by Raman spectroscopy. *Journal of Solid State Chemistry*, 167(2):425–434, 2002.

- [42] D. Y. Lu, J. Chen, H. J. Chen, L. Gong, S. Z. Deng, N. S. Xu, and Y. L. Liu. Raman study of thermochromic phase transition in tungsten trioxide nanowires. *Applied Physics Letters*, 90(4):1–4, 2007.
- [43] F. P. Koffyberg, K. Dwight, and A. Wold. Interband transitions of semiconducting oxides determined from photoelectrolysis spectra. *Solid State Communications*, 30(7):433–437, 1979.
- [44] M. Deepa, A. K. Srivastava, M. Kar, and S. A. Agnihotry. A case study of optical properties and structure of sol–gel derived nanocrystalline electrochromic WO₃ films. *Journal of Physics D: Applied Physics*, 39(9):1885–1893, 2006.
- [45] R. A. May, L. Kondrachova, B. P. Hahn, and K. J. Stevenson. Optical Constants of Electrodeposited Mixed Molybdenum - Tungsten Oxide Films Determined by Variable-Angle Spectroscopic Ellipsometry. *Journal of Physical Chemistry C*, 111:18251–18257, 2007.
- [46] J. M. Berak and M. J. Sienko. Effect of oxygen-deficiency on electrical transport properties of tungsten trioxide crystals. *Journal of Solid State Chemistry*, 2(1):109–133, 1970.
- [47] B. A. De Angelis and M. Schiavello. X-ray photoelectron spectroscopy study of nonstoichiometric tungsten oxides. *Journal of Solid State Chemistry*, 21(1):67–72, 1977.
- [48] A. Hjelm, C. Granqvist, and J. Wills. Electronic structure and optical properties of WO₃, LiWO₃, NaWO₃, and HWO₃. *Physical Review B*, 54(4):2436–2445, 1996.
- [49] H. Zheng, J. Z. Ou, M. S. Strano, R. B. Kaner, A. Mitchell, and K. Kalantar-zadeh. Nanostructured Tungsten Oxide - Properties, Synthesis, and Applications. *Advanced Functional Materials*, 21(12):2175–2196, 2011.
- [50] Caterina Soldano, Elisabetta Comini, Camilla Baratto, Matteo Ferroni, Guido Faglia, and Giorgio Sberveglieri. Metal oxides mono-dimensional nanostructures for gas sensing and light emission. *Journal of the American Ceramic Society*, 95(3):831–850, jan 2012.

- [51] E. Comini, C. Baratto, G. Faglia, M. Ferroni, A. Vomiero, and G. Sberveglieri. Quasi-one dimensional metal oxide semiconductors: Preparation, characterization and application as chemical sensors. *Progress in Materials Science*, 54:1–67, 2009.
- [52] Y. Wu and P. Yang. Direct observation of vapor-liquid-solid nanowire growth. *Journal of the American Chemical Society*, 123(13):3165–3166, 2001.
- [53] M. Chhowalla, K. B. K. Teo, C. Ducati, N. L. Rupesinghe, G. A. J. Amaratunga, A. C. Ferrari, D. Roy, J. Robertson, and W. I. Milne. Growth process conditions of vertically aligned carbon nanotubes using plasma enhanced chemical vapor deposition. *Journal of Applied Physics*, 90(10):5308–5317, 2001.
- [54] B. M. Kayes, M. A. Filler, M. C. Putnam, M. D. Kelzenberg, N. S. Lewis, and H. A. Atwater. Growth of vertically aligned Si wire arrays over large areas with Au and Cu catalysts. *Applied Physics Letters*, 91(10):1–4, 2007.
- [55] P. X. Gao, Y. Ding, and Z. L. Wang. Crystallographic orientation-aligned ZnO nanorods grown by a tin catalyst. *Nano Letters*, 3(9):1315–1320, 2003.
- [56] S. M. Roper, S. H. Davis, S. A. Norris, A. A. Golovin, P. W. Voorhees, and M. Weiss. Steady growth of nanowires via the vapor-liquid-solid method. *Journal of Applied Physics*, 102(3), 2007.
- [57] J. Thangala, S. Vaddiraju, R. Bogale, R. Thurman, T. Powers, B. Deb, and M. K. Sunkara. Large-scale, hot-filament-assisted synthesis of tungsten oxide and related transition metal oxide nanowires. *Small*, 3(5):890–896, 2007.
- [58] K. Wasa, I. Kanno, and H. Kotera. *Handbook of Sputter Deposition Technology - Fundamentals and Applications for Functional Thin Films, Nanomaterials, and MEMS*. Elsevier, 2012.
- [59] C.-H. Chen, S.-J. Wang, R.-M. Ko, Y.-C. Kuo, K.-M. Uang, T.-M. Chen, B.-W. Liou, and H.-Y. Tsai. The influence of oxygen content in the sputtering gas on the self-synthesis of tungsten oxide nanowires on sputter-deposited tungsten films. *Nanotechnology*, 17:217–223, 2006.

- [60] Hong Goo Choi, Young Hwa Jung, and Do Kyung Kim. Solvothermal Synthesis of Tungsten Oxide Nanorod/Nanowire/Nanosheet. *Journal of the American Ceramic Society*, 88(6):1684–1686, jun 2005.
- [61] L. Zhou, J. Zou, M. Yu, P. Lu, J. Wei, Y. Qian, and Y. Wang. Green Synthesis of Hexagonal-Shaped $\text{WO}_{3.0,33}\text{H}_2\text{O}$ Nanodiscs Composed of Nanosheets. *Crystal Growth & Design*, 8(11):3993, 2008.
- [62] B. Tang, L. Zhuo, J. Ge, J. Niu, and Z. Shi. Hydrothermal synthesis of ultralong and single-crystalline $\text{Cd}(\text{OH})_2$ nanowires using alkali salts as mineralizers. *Inorganic Chemistry*, 44(8):2568–9, 2005.
- [63] Z. Gu, T. Zhai, B. Gao, X. Sheng, Y. Wang, H. Fu, Y. Ma, and J. Yao. Controllable assembly of WO_3 nanorods/nanowires into hierarchical nanostructures. *Journal of Physical Chemistry B*, 110(47):23829–23836, 2006.
- [64] S. Rajagopal, D. Nataraj, D. Mangalaraj, Y. Djaoued, J. Robichaud, and O. Y. Khyzhun. Controlled growth of WO_3 nanostructures with three different morphologies and their structural, optical, and photodecomposition studies. *Nanoscale Research Letters*, 4(11):1335–1342, 2009.
- [65] K. D. Lee. Deposition of WO_3 thin films by the sol-gel method. *Thin Solid Films*, 302:84–88, 1997.
- [66] S. Pokhrel, C. E. Simion, V. S. Teodorescu, N. Barsan, and U. Weimar. Synthesis, mechanism, and gas-sensing application of surfactant tailored tungsten oxide nanostructures. *Advanced Functional Materials*, 19(11):1767–1774, 2009.
- [67] B. B. Lakshmi, P. K. Dorhout, and C. R. Martin. Sol-Gel Template Synthesis of Semiconductor Nanostructures. *Chemistry of Materials*, 9(8):857–862, 1997.
- [68] J. Livage and D. Ganguli. Sol gel electrochromic coatings and devices : A review. *Solar energy materials and solar cells*, 68:365–381, 2001.

- [69] K. Yamanaka, H. Oakamoto, H. Kidou, and T. Kudo. Peroxotungstic acid coated films for electrochromic display devices. *Japanese Journal of Applied Physics*, 25(9 R):1420–1426, 1986.
- [70] S. Badilescu and P. V. Ashrit. Study of sol-gel prepared nanostructured WO₃ thin films and composites for electrochromic applications. *Solid State Ionics*, 158(1-2):187–197, 2003.
- [71] W. H. Lai, J. Shieh, L. G. Teoh, and M. H. Hon. Fabrication of one-dimensional mesoporous tungsten oxide. *Nanotechnology*, 17(1):110–115, 2005.
- [72] K. Zhu, H. He, S. Xie, X. Zhang, W. Zhou, S. Jin, and B. Yue. Crystalline WO₃ nanowires synthesized by templating method. *Chemical Physics Letters*, 377(3-4):317–321, 2003.
- [73] E. Rossinyol, J. Arbiol, F. Peiró, A. Cornet, J.R. Morante, B. Tian, T. Bo, and D. Zhao. Nanostructured metal oxides synthesized by hard template method for gas sensing applications. *Sensors and Actuators, B: Chemical*, 109(1):57–63, 2005.
- [74] X.-L. Li, T.-J. Lou, X.-M. Sun, and Y.-D. Li. Highly Sensitive WO₃ Hollow-Sphere Gas Sensors. *Inorganic Chemistry*, 43(17):9079–9085, 2004.
- [75] C. Santato, M. Ulmann, and J. Augustynski. Enhanced visible light conversion efficiency using nanocrystalline WO₃ films. *Advanced Materials*, 13(7):511–514, 2001.
- [76] M. Sadakane, K. Sasaki, H. Kunioku, B. Ohtani, R. Abe, and W. Ueda. Preparation of 3-D ordered macroporous tungsten oxides and nano-crystalline particulate tungsten oxides using a colloidal crystal template method, and their structural characterization and application as photocatalysts under visible light irradiation. *Journal of Materials Chemistry*, 20:1811–1818, 2010.
- [77] A. Formhals. Process and apparatus for preparing artificial threads (US patent 1975504), 1934.

- [78] D. H. Reneker and I. Chun. Nanometre diameter fibres of polymer, produced by electrospinning. *Nanotechnology*, 7(3):216–223, 1996.
- [79] X. Lu, X. Liu, W. Zhang, C. Wang, and Y. Wei. Large-scale synthesis of tungsten oxide nanofibers by electrospinning. *Journal of Colloid and Interface Science*, 298(2):996–999, 2006.
- [80] I. M. Szilágyi, E. Santala, M. Heikkilä, M. Kemell, T. Nikitin, L. Khriachtchev, M. Räsänen, M. Ritala, and M. Leskelä. Thermal study on electrospun polyvinylpyrrolidone/ammonium metatungstate nanofibers: Optimising the annealing conditions for obtaining WO₃ nanofibers. *Journal of Thermal Analysis and Calorimetry*, 105(1):73–81, 2011.
- [81] G. Wang, Y. Ji, X. Huang, X. Yang, P. I. Gouma, and M. Dudley. Fabrication and characterization of polycrystalline WO₃ nanofibers and their application for ammonia sensing. *Journal of Physical Chemistry B*, 110(47):23777–23782, 2006.
- [82] H. S. Shim, J. W. Kim, Y. E. Sung, and W. B. Kim. Electrochromic properties of tungsten oxide nanowires fabricated by electrospinning method. *Solar Energy Materials and Solar Cells*, 93(12):2062–2068, 2009.
- [83] C. G. Granqvist. Electrochromic oxides: a bandstructure approach. *Solar Energy Materials and Solar Cells*, 32(4):369–382, 1994.
- [84] C. G. Granqvist. Electrochromic tungsten oxide: Review of progress 1993-1998. *Solar Energy Materials and Solar Cells*, 60:201–262, 2000.
- [85] P. M. S. Monk, R. J. Mortimer, and D. R. Rosseinsky. *Electrochromism: Fundamentals and Applications*. Wiley-VCH, 1995.
- [86] S. J. Yoo, J. W. Lim, Y.-E. Sung, Y. H. Jung, H. G. Choi, and D. K. Kim. Fast switchable electrochromic properties of tungsten oxide nanowire bundles. *Applied Physics Letters*, 90(17):173126, 2007.

- [87] G. A. Niklasson and C. G. Granqvist. Electrochromics for smart windows: thin films of tungsten oxide and nickel oxide, and devices based on these. *Journal of Materials Chemistry*, 17(2):127–156, 2007.
- [88] A. J. More, R. S. Patil, D. S. Dalavi, S. S. Mali, C. K. Hong, M. G. Gang, J. H. Kim, and P. S. Patil. Electrodeposition of nano-granular tungsten oxide thin films for smart window application. *Materials Letters*, 134:298–301, 2014.
- [89] C. Lampert. Smart switchable glazing for solar energy and daylight control. *Solar Energy Materials and Solar Cells*, 52(3-4):207–221, 1998.
- [90] A. Fujishima and K. Honda. Electrochemical photolysis of water at a semiconductor electrode. *Nature*, 238:37, 1972.
- [91] B. D. Alexander, P. J. Kulesza, I. Rutkowska, R. Solarska, and J. Augustynski. Metal oxide photoanodes for solar hydrogen production. *Journal of Materials Chemistry*, 18:2298–2303, 2008.
- [92] H. Zhang, G. Chen, and D. W. Bahnemann. Photoelectrocatalytic Materials for Environmental Applications. *Journal of Materials Chemistry*, 19:5089–5121, 2009.
- [93] C. Santato, M. Ulmann, and J. Augustynski. Photoelectrochemical properties of nanostructured tungsten trioxide films. *Journal of Physical Chemistry B*, 105(5):936–940, 2001.
- [94] K. Sayama, K. Mukasa, R. Abe, Y. Abe, and H. Arakawa. Stoichiometric water splitting into H₂ and O₂ using a mixture of two different photocatalysts and an IO₃⁻/I⁻ shuttle redox mediator under visible light irradiation. *Chemical Communications*, 23:2416–2417, 2001.
- [95] X. C. Song, Y. F. Zheng, E. Yang, and Y. Wang. Large-scale hydrothermal synthesis of WO₃ nanowires in the presence of K₂SO₄. *Materials Letters*, 61(18):3904–3908, 2007.

- [96] Acid Digestion Vessel 4744 from Parr Instruments. <http://www.parrinst.com/products/sample-preparation/acid-digestion/general-purpose-acid-digestion-vessel-model-4744-45-ml/>.
- [97] Universal oven UNB200 from memmert GmbH + Co.KG. <https://www.memmert.com/>.
- [98] J. Wang, E. Khoo, P. S. Lee, and J. Ma. Synthesis, assembly, and electrochromic properties of uniform crystalline WO₃ nanorods. *Journal of Physical Chemistry C*, 112(37):14306–14312, 2008.
- [99] Z. Gu, H. Li, T. Zhai, W. Yang, Y. Xia, Y. Ma, and J. Yao. Large-scale synthesis of single-crystal hexagonal tungsten trioxide nanowires and electrochemical lithium intercalation into the nanocrystals. *Journal of Solid State Chemistry*, 180(1):98–105, 2007.
- [100] X. Song, Y. Zhao, and Y. Zheng. Hydrothermal synthesis of tungsten oxide nanobelts. *Materials Letters*, 60(28):3405–3408, 2006.
- [101] Z. G. Zhao and M. Miyauchi. Shape Modulation of Tungstic Acid and Tungsten Oxide Hollow Structures. *Journal of Physical Chemistry C*, 113(16):6539–6546, 2009.
- [102] D. J. Ham, A. Phuruangrat, S. Thongtem, and J. S. Lee. Hydrothermal synthesis of monoclinic WO₃ nanoplates and nanorods used as an electrocatalyst for hydrogen evolution reactions from water. *Chemical Engineering Journal*, 165(1):365–369, 2010.
- [103] O. Yayapao, T. Thongtem, A. Phuruangrat, and S. Thongtem. CTAB-assisted hydrothermal synthesis of tungsten oxide microflowers. *Journal of Alloys and Compounds*, 509(5):2294–2299, 2011.
- [104] J. Li, M. Posfai, P. V. Hobbs, and P. R. Buseck. Individual Aerosol Particles from Biomass Burning in Southern Africa: 2. Compositions and Aging of Inorganic Particles. *Journal of Geophysical Research*, 108:1–12, 2003.

- [105] A. Baserga, V. Russo, F. Di Fonzo, A. Bailini, D. Cattaneo, C. S. Casari, A. Li Bassi, and C. E. Bottani. Nanostructured tungsten oxide with controlled properties: Synthesis and Raman characterization. *Thin Solid Films*, 515(16):6465–6469, jun 2007.
- [106] R. F. Garcia-Sanchez, T. Ahmido, D. Casimir, S. Baliga, and P. Misra. Thermal Effects Associated with the Raman Spectroscopy of WO₃ Gas-Sensor Materials. *Journal of Physical Chemistry A*, 117:13825–13831, 2013.
- [107] C. Bittencourt and R. Landers. The role of oxygen partial pressure and annealing temperature on the formation of W=O bonds in thin WO₃ films. *Semiconductor Science and Technology*, 17:522, 2002.
- [108] K. Kalantar-Zadeh, A. Vijayaraghavan, M. H. Ham, H. Zheng, M. Breedon, and M. S. Strano. Synthesis of atomically thin WO₃ sheets from hydrated tungsten trioxide. *Chemistry of Materials*, 22(19):5660–5666, 2010.
- [109] E. Salje. Lattice dynamics of WO₃. *Acta Crystallographica Section A*, 31(3):360–363, 1975.
- [110] J. Oi, A. Kishimoto, T. Kudo, and M. Hiratani. Hexagonal tungsten trioxide obtained from peroxo-polytungstate and reversible lithium electro-intercalation into its framework. *Journal of Solid State Chemistry*, 96(1):13–19, 1992.
- [111] FIZ Karlsruhe ICSD. <https://icsd.fiz-karlsruhe.de>.
- [112] Z. Gu, M. Ying, T. Zhai, B. Gao, W. Yang, and J. Yao. A simple hydrothermal method for the large-scale synthesis of single-crystal potassium tungsten bronze nanowires. *Chemistry - A European Journal*, 12(29):7717–7723, 2006.
- [113] C. Guo, S. Yin, L. Huang, and T. Sato. Synthesis of one-dimensional potassium tungsten bronze with excellent near-infrared absorption property. *ACS Applied Materials and Interfaces*, 3(7):2794–2799, 2011.

- [114] A. Magneli and B. Blomberg. Contribution to the Knowledge of the Alkali Tungsten Bronzes. *Acta Chemica Scandinavica*, 5:372–378, 1951.
- [115] T. Kudo, J. Oi, A. Kishimoto, and M. Hiratani. Three kinds of framework structures of corner-sharing WO₆ octahedra derived from peroxo- polytungstates as a precursor. *Materials Research Bulletin*, 26:779–787, 1991.
- [116] D. Y. Lu, J. Chen, J. Zhou, S. Z. Deng, N. S. Xu, and J. B. Xu. Raman spectroscopic study of oxidation and phase transition in W₁₈O₄₉ nanowires. *Journal of Raman Spectroscopy*, 38:176–180, 2007.
- [117] L.-W. Liu, J. Zheng, J.-L. Wang, J. Xu, H.-H. Li, and S.-H. Yu. Ultrathin W₁₈O₄₉ nanowire assemblies for electrochromic devices. *Nano Letters*, 13:1–8, 2013.
- [118] E. Comini and G. Sberveglieri. Metal oxide nanowires as chemical sensors. *Materials Today*, 13(7-8):36–44, 2010.
- [119] S. D. Hoath. *Fundamentals of Inkjet Printing: The Science of Inkjet and Droplets*. Wiley-VCH, 2016.
- [120] M. Singh, H. M. Haverinen, P. Dhagat, and G. E. Jabbour. Inkjet printing-process and its applications. *Advanced Materials*, 22(6):673–685, 2010.
- [121] L. Liao, Z. Zhang, B. Yan, Z. Zheng, Q. L. Bao, T. Wu, C. M. Li, Z. X. Shen, J. X. Zhang, H. Gong, J. C. Li, and T. Yu. Multifunctional CuO nanowire devices: p-type field effect transistors and CO gas sensors. *Nanotechnology*, 20(8):085203, 2009.
- [122] Z. Fan, J. C. Ho, Z. A. Jacobson, R. Yerushalmi, R. L. Alley, H. Razavi, and A. Javey. Wafer-scale assembly of highly ordered semiconductor nanowire arrays by contact printing. *Nano Letters*, 8(1):20–25, 2008.
- [123] A. C. Ford, J. C. Ho, Z. Fan, O. Ergen, V. Altoe, S. Aloni, H. Razavi, and A. Javey. Synthesis, contact printing, and device characterization of Ni-catalyzed, crystalline InAs nanowires. *Nano Research*, 1:32–39, 2008.

- [124] T. Takahashi, K. Takei, J. C. Ho, Y. L. Chueh, Z. Fan, and A. Javey. Monolayer resist for patterned contact printing of aligned nanowire arrays. *Journal of the American Chemical Society*, 131:2102–2103, 2009.
- [125] R. Yerushalmi, Z. A. Jacobson, J. C. Ho, Z. Fan, and A. Javey. Large scale, highly ordered assembly of nanowire parallel arrays by differential roll printing. *Applied Physics Letters*, 91:1–4, 2007.
- [126] L. Mai, Y. Gu, C. Han, B. Hu, W. Chen, P. Zhang, L. Xu, W. Guo, and Y. Dai. Orientated Langmuir-Blodgett Assembly of VO₂ Nanowires. *Nano Letters*, 9(2):826–830, 2009.
- [127] J. Israelachvili. *Intermolecular and Surface Forces*. Academic Press, 3rd edition, 2011.
- [128] G. Cao and Y. Wang. *Nanostructures and Nanomaterials: Synthesis, Properties, and Applications*. World Scientific Publishing Co. Pte. Ltd., 2011.
- [129] D. Whang, S. Jin, and C. M. Lieber. Nanolithography using hierarchically assembled nanowire masks. *Nano Letters*, 3(7):951–954, 2003.
- [130] G. Roberts. *Langmuir-Blodgett Films*. Springer Science+Business, 1990.
- [131] D. Whang, S. Jin, Y. Wu, and C. M Lieber. Large-Scale Hierarchical Organization of Nanowire Arrays for Integrated Nanosystems. *Nano Letters*, 3(9):1255–1259, 2003.
- [132] D. Wang, Y. L. Chang, Z. Liu, and H. Dai. Oxidation Resistant Germanium Nanowires: Bulk Synthesis, Long Chain Alkanethiol Functionalization and Langmuir-Blodgett Assembly. *Journal of American Chemical Society*, 127:11871–11875, 2005.
- [133] A. R. Tao, J. Huang, and P. Yang. Langmuir-Blodgettry of nanocrystals and nanowires. *Accounts of Chemical Research*, 41(12):1662–1673, 2008.
- [134] J. Guilera, C. Fabrega, O. Casals, F. Hernandez-Ramirez, S. Wang, S. Mathur, Fl. Udrea, A. De Luca, S. Z. Ali, A. Romano-Rodriguez, J. D. Prades, and J. R. Morante.

- Facile integration of ordered nanowires in functional devices. *Sensors and Actuators, B: Chemical*, 221:104–112, 2015.
- [135] E. M. Freer, O. Grachev, and D. P. Stumbo. High-yield self-limiting single-nanowire assembly with dielectrophoresis. *Nature Nanotechnology*, 5(7):525–530, 2010.
- [136] S. Kumar, S. Rajaraman, R. A. Gerhardt, Z. L. Wang, and P. J. Hesketh. Tin oxide nanosensor fabrication using AC dielectrophoretic manipulation of nanobelts. *Electrochimica Acta*, 51(5):943–951, 2005.
- [137] C. S. Lao, J. Liu, P. Gao, L. Zhang, D. Davidovic, R. Tummala, and Z. L. Wang. ZnO Nanobelt / Nanowire Schottky Diodes Formed by Dielectrophoresis Alignment across Au Electrodes. *Nano Letters*, 6(2):263–266, 2006.
- [138] Y. Liu, J.-h. Chung, W. K. Liu, and R. S. Ruoff. Dielectrophoretic Assembly of Nanowires. *Journal of Physical Chemistry B*, 110:14098–14106, 2006.
- [139] Dimatix Materials Printer DMP2831 FUJIFILM. <https://www.fujifilmusa.com/shared/bin/PDS00085-DMP2831.pdf>.
- [140] Delta-R. <http://delta-r.de/>.
- [141] mb Technologies GmbH. <http://www.mb-technologies.com/>.
- [142] F&K DELVOTEC. <http://www.fkdelvotec.com/>.
- [143] Hesse GmbH. <http://www.hesse-mechatronics.com/>.
- [144] G. Korotcenkov. *Handbook of Gas Sensor Materials*, volume 2. Springer, 2014.
- [145] J. H. Park and K. H. Kim. Improvement of long-term stability in SnO₂-based gas sensor for monitoring offensive odor. *Sensors and Actuators*, 56:50–58, 1999.
- [146] M. Fleischer, L. Höllbauer, and H. Meixner. Effect of the sensor structure on the stability of Ga₂O₃ sensors for reducing gases. *Sensors and Actuators, B: Chemical*, 18(1-3):119–124, 1994.

- [147] E. Brunet. *Fabrication of tin oxide nanowire gas sensors*. Doctoral thesis, Technical University of Vienna, 2014.
- [148] J. Tamaki, J. Niimi, S. Ogura, and S. Konishi. Effect of micro-gap electrode on sensing properties to dilute chlorine gas of indium oxide thin film microsensors. *Sensors and Actuators, B: Chemical*, 108:202–206, 2005.
- [149] S. Capone, P. Siciliano, F. Quaranta, R. Rella, M. Epifani, and L. Vasanelli. Moisture influence and geometry effect of Au and Pt electrodes on CO sensing response of SnO₂ microsensors based on sol-gel thin film. *Sensors and Actuators, B: Chemical*, 77:503–511, 2001.
- [150] R. Pohle, M. Fleischer, and H. Meixner. Infrared emission spectroscopic study of the adsorption of oxygen on gas sensors based on polycrystalline metal oxide films. *Sensors and Actuators, B: Chemical*, 78(1-3):133–137, 2001.
- [151] N. Yamazoe, J. Fuchigami, M. Kishikawa, and T. Seiyama. Interactions of tin oxide surface with O₂, H₂O and H₂. *Surface Science*, 86(C):335–344, 1979.
- [152] M. Caldaru, D. Sprinceana, V. T. Popa, and N. I. Ionescu. Surface dynamics in tin dioxide-containing catalysts II. Competition between water and oxygen adsorption on polycrystalline tin dioxide. *Sensors and Actuators, B: Chemical*, 30(1):35–41, 1996.
- [153] G. Heiland and D. Kohl. *Chemical Sensor Technology Vol.1*. tokyo:kod ed., 1988.
- [154] M. A. Barteau. Site requirements of reactions on oxide surfaces. *Journal of Vacuum Science & Technology A: Vacuum, Surfaces, and Films*, 11:2162–2597, 1993.
- [155] N. Barsan and U. Weimar. Understanding the fundamental principles of metal oxide based gas sensors; the example of CO sensing with SnO₂ sensors in the presence of humidity. *Journal of Physics: Condensed Matter*, 15(20):R813–R839, 2003.
- [156] S. R. Morrison. Semiconductor gas sensors. *Sensors and Actuators*, 2:329–341, 1981.
- [157] C. S. Rout, M. Hegde, and C. N. R. Rao. H₂S sensors based on tungsten oxide nanostructures. *Sensors and Actuators, B: Chemical*, 128(2):488–493, 2008.

- [158] B. Frühberger, M. Grunze, and D. J. Dwyer. Surface chemistry of H₂S-sensitive tungsten oxide films. *Sensors and Actuators, B: Chemical*, 31(3):167–174, 1996.
- [159] E. P. S. Barrett and G. C. Georgiades. The Mechanism of Operation of WO₃-based H₂S Sensors. *Sensors and Actuators, B*:116–120, 1990.
- [160] R. L. D. Whitby, W. K. Hsu, H. W. Kroto, and D. R. M. Walton. Conversion of amorphous WO_{3-x} into WS₂ nanotubes. *Physical Chemistry Chemical Physics*, 4(16):3938–3940, 2002.
- [161] V. O. Glemser, H. Sauer, and P. König. Über Wolframsulfide und Wolframselenide. *Zeitschrift für anorganische Chemie*, 144(54), 1948.
- [162] S. H. Hahn, N. Barsan, U. Weimar, S. G. Ejakov, J. H. Visser, and R. E. Soltis. CO sensing with SnO₂ thick film sensors: Role of oxygen and water vapour. *Thin Solid Films*, 436(1):17–24, 2003.
- [163] N. Mizuno, T. Yoshioka, K. Kato, and M. Iwamoto. CO₂-sensing characteristics of SnO₂ element modified by La₂O₃. *Sensors and Actuators, B: Chemical*, 13-14:473–475, 1993.
- [164] B. Ostrick, M. Fleischer, H. Meixner, and C. D. Kohl. Investigation of the reaction mechanisms in work function type sensors at room temperature by studies of the cross-sensitivity to oxygen and water: the carbonate-carbon dioxide system. *Sensors and Actuators, B: Chemical*, 68(1):197–202, 2000.
- [165] D. H. Kim, J. Y. Yoon, H. C. Park, and K. H. Kim. CO₂-sensing characteristics of SnO₂ thick film by coating lanthanum oxide. *Sensors and Actuators, B: Chemical*, 62(1):61–66, 2000.
- [166] I. Lee. Carbon dioxide resistive sensor based on titanium oxide nanowires doped with potassium. *Micro & Nano Letters*, 9(4):248–250, 2014.
- [167] M. Madou and S. Morrison. *Chemical Sensing with Solid State Devices*. Academic Press, 1989.

- [168] C. Wang, L. Yin, Y. Zhang, D. Xiang, and R. Gao. Metal oxide gas sensors: Sensitivity and influencing factors. *Sensors*, 10(3):2088–2106, 2010.
- [169] J. F. Chang, H. H. Kuo, I. C. Leu, and M. H. Hon. The effects of thickness and operation temperature on ZnO:Al thin film CO gas sensor. *Sensors and Actuators, B: Chemical*, 84(2-3):258–264, 2002.
- [170] Y. Shimizu, N. Matsunaga, T. Hyodo, and M. Egashira. Improvement of SO₂ sensing properties of WO₃ by noble metal loading. *Sensors and Actuators, B: Chemical*, 77:35–40, 2001.
- [171] Y. Zhang, X. He, J. Li, Z. Miao, and F. Huang. Fabrication and ethanol-sensing properties of micro gas sensor based on electrospun SnO₂ nanofibers. *Sensors and Actuators, B: Chemical*, 132(1):67–73, 2008.
- [172] Q. Wan, Q. H. Li, Y. J. Chen, T. H. Wang, X. L. He, J. P. Li, and C. L. Lin. Fabrication and ethanol sensing characteristics of ZnO nanowire gas sensors. *Applied Physics Letters*, 84(18):3654–3656, 2004.
- [173] Y.-J. Choi, I.-S. Hwang, J.-G. Park, K. J. Choi, J.-H. Park, and J.-H. Lee. Novel fabrication of an SnO₂ nanowire gas sensor with high sensitivity. *Nanotechnology*, 19(9):095508, 2008.
- [174] A. Kolmakov, D. O. Klenov, Y. Lilach, S. Stemmer, and M. Moskovitst. Enhanced gas sensing by individual SnO₂ nanowires and nanobelts functionalized with Pd catalyst particles. *Nano Letters*, 5(4):667–673, 2005.
- [175] S. Vallejos, T. Stoycheva, P. Umek, C. Navio, R. Snyders, C. Bittencourt, E. Llobet, C. Blackman, S. Moniz, and X. Correig. Au nanoparticle-functionalised WO₃ nanoneedles and their application in high sensitivity gas sensor devices. *Chemical Communications*, 47(1):565–567, 2011.
- [176] N. Singh, R. K. Gupta, and P. S. Lee. Gold-nanoparticle-functionalized In₂O₃ nanowires as CO Gas sensors with a significant enhancement in response. *ACS Applied Materials and Interfaces*, 3(7):2246–2252, 2011.

- [177] J. Guo, J. Zhang, M. Zhu, D. Ju, H. Xu, and B. Cao. High-performance gas sensor based on ZnO nanowires functionalized by Au nanoparticles. *Sensors and Actuators, B: Chemical*, 199:333–339, 2014.

List of Figures

2.1. Band model of insulator, semiconductor and conductor.	4
2.2. Energy bands of n-type and p-type semiconducting metal oxides.	6
2.3. Schematic of conduction mechanism in a porous metal oxide thick film gas sensor.	8
2.4. Schematic of conduction mechanism in a compact thin film metal oxide gas sensor.	9
2.5. Schematic of conduction mechanism in multi nanowire metal oxide gas sensor.	10
3.1. Crystal structure of WO_3	13
3.2. Crystal structure of WO_2	14
4.1. Autoclave and dried nanowire powder.	22
4.2. SEM image of tungsten oxide nanowires.	24
4.3. SEM image of tungsten oxide nanowires (higher magnification).	24
4.4. TEM image of tungsten oxide nanowires.	26
4.5. High resolution TEM image of an individual tungsten oxide nanowire.	26
4.6. Selected area diffraction (SAED) pattern.	27
4.7. SAED pattern with peak profile of reflections.	28
4.8. EDX spectrum of tungsten oxide nanowires.	30
4.9. Raman spectra of tungsten oxide nanowires.	32
4.10. Raman spectra of tungsten oxide nanowires with increased laser power.	32
4.11. Raman spectra of tungsten oxide nanowires with increasing laser power.	33
4.12. Raman spectra of tungsten oxide nanowires with alternating laser power.	33
4.13. Raman spectra of tungsten oxide nanowires after thermal treatment of 400 °C for 12 h.	34
4.14. SEM image of tungsten oxide nanowires without temperature treatment.	35
4.15. SEM image of annealed tungsten oxide nanowires.	35
4.16. XRD spectrum of tungsten oxide nanowires.	36
5.1. CMOS microhotplate stack.	42

5.2.	Straightforward microhotplate with heated suspended membrane.	42
5.3.	Power consumption vs. temperature of CMOS MPW3mod microhotplate.	43
5.4.	CMOS MPW3mod microhotplate chip with two microhotplates.	44
5.5.	CMOS MPW3mod microhotplate with an arm length of 147 μm	44
5.6.	MPW3mod CMOS microhotplate with tungsten plugs.	45
5.7.	Tungsten plugs on CMOS MPW3mod microhotplate.	45
5.8.	Power consumption vs. temperature of CMOS MPW4 microhotplate. . .	46
5.9.	CMOS MPW4 microhotplate chip with eight microhotplates.	47
5.10.	CMOS MPW4 microhotplate with gold electrodes.	47
5.11.	Inkjet printer DMP-2831 from FUJIFILM [139].	52
5.12.	Silicon based sensor.	53
5.13.	IDES electrode design used for silicon based sensor.	53
5.14.	IDES electrode design used for MPW3mod and MPW4.	54
5.15.	MPW4 electrodes with IDES electrodes made by ebeam lithography. . . .	54
5.16.	CMOS MPW3mod microhotplate chip wire bonded on carrier.	55
5.17.	CMOS MPW4 microhotplate chip wire bonded on carrier.	55
5.18.	Fabrication process of tungsten oxide nanowire gas sensors.	56
5.19.	CMOS MPW4 tungsten oxide nanowire sensor before sensor annealing. .	60
5.20.	CMOS MPW4 tungsten oxide nanowire sensor after sensor annealing. . .	60
5.21.	Raman spectra during sensor annealing with several measurements. . . .	62
5.22.	Raman spectra during sensor annealing (0 h, 1 h, 2 h, 3 h and 4 h).	62
5.23.	Microscope image at the start of sensor annealing and after 3 h.	63
5.24.	Microscope image after 12 h of sensor annealing.	63
6.1.	Scheme of water adsorption mechanism on metal oxide surfaces.	65
6.2.	Gas measurement setup in the laboratory.	70
6.3.	Scheme of gas measurement setup.	70
6.4.	Scheme of gas measurement with temperature and humidity levels. . . .	72
6.5.	Scheme of gas pulse configuration.	72
6.6.	Scheme of response and recovery time definition.	73
6.7.	Sensor response (sensor 1) vs. sensor operation temperature.	75

6.8.	H ₂ S gas measurement at 300 °C and three relative humidity levels.	77
6.9.	H ₂ S gas response in (%) at 300 °C at three relative humidity levels.	77
6.10.	H ₂ S gas measurement at 250 °C and three relative humidity levels.	79
6.11.	H ₂ S gas response in (%) at 250 °C at three relative humidity levels.	79
6.12.	Normalised sensor resistance for the exposure to 1000 ppb H ₂ S.	80
6.13.	H ₂ S gas measurement with 500 ppm CO ₂ added to the background gas.	82
6.14.	H ₂ S gas response in (%) with 500 ppm CO ₂ added to the background gas.	82
6.15.	CO gas measurement of sensor 1 at 350 °C.	85
6.16.	CO gas measurement of sensor 2 at 350 °C.	85
6.17.	CO gas response in (%) at 350 °C.	86
6.18.	CO gas response in (%) at 350 °C for sensor 1.	86
6.19.	CO gas response in (%) at 300 °C.	87
6.20.	CO gas response in (%) at 250 °C.	87
6.21.	CO gas measurement of CMOS MPW4 sensor at 250 °C.	88
6.22.	CO gas response in (%) at 250 °C for sensor 1, sensor 2 and the CMOS MPW4 sensor.	88
6.23.	CO ₂ gas measurement of CMOS MPW3mod sensor at 400 °C.	91
6.24.	CO ₂ gas response of CMOS MPW3mod sensor in (%) at 400 °C.	91
6.25.	H ₂ S gas measurement at 250 °C in nitrogen atmosphere.	94
6.26.	CO gas measurement at 350 °C in nitrogen atmosphere.	95
6.27.	Response time in (s) of CO gas measurement (sensor 1).	101
6.28.	Recovery time in (s) of CO gas measurement (sensor 1).	101
7.1.	TEM images of tungsten oxide nanowires with NiPt nanoparticles.	108
7.2.	Scheme of potential nanowire printing tool.	108
7.3.	Nanowire sensor array on CMOS MPW4 microhotplate chip.	109
A.1.	SAED pattern with six most intense reflection rings highlighted.	135
A.2.	Profile of SAED pattern; peak at a distance of 2.469 (nm ⁻¹).	136
A.3.	Profile of SAED pattern; peak at a distance of 2.757 (nm ⁻¹).	136
A.4.	Profile of SAED pattern; peak at a distance of 5.058 (nm ⁻¹).	137
A.5.	Profile of SAED pattern; peak at a distance of 5.321 (nm ⁻¹).	137

A.6. Profile of SAED pattern; peak at a distance of 7.598 (nm^{-1}).	138
A.7. Profile of SAED pattern; peak at a distance of 7.838 (nm^{-1}).	138
B.1. XRD spectrum with peak positions from database for hexagonal WO_3 . . .	139

List of Tables

2.1. Examples for n-type and p-type metal oxide materials [10].	5
4.1. Summary of WO _x nanostructures synthesised by hydrothermal method. .	23
4.2. Evaluation of SAED pattern.	28
4.3. Composition of tungsten oxide nanowires - approximated calculation of atomic percentage of oxygen (O), potassium (K) and tungsten (W).	30
4.4. Indications for suggested tungsten oxide nanowire compositions.	40
6.1. Sensor assignment for specific target gases.	74
6.2. Sensor response (%) of H ₂ S gas measurement in synthetic air (SA) and nitrogen (N ₂); the sensor response value for the measurement in SA is a mean value of the three relative humidity levels of 25 %, 50 % and 75 % and the sensor response value for the measurement in N ₂ is calculated for the first gas pulse.	94
6.3. Sensor response (%) of CO gas measurements in synthetic air (SA) and nitrogen (N ₂); the sensor response value for the measurement in SA is a mean value of the three relative humidity levels of 25 %, 50 % and 75 % and the sensor response value for the measurement in N ₂ is calculated for the first gas pulse.	95
6.4. Response times (<i>t_{resp}</i>) of H ₂ S and CO gas measurements in synthetic air (SA) and nitrogen (N ₂); <i>t_{resp}</i> for measurements in SA are mean values of the three relative humidity levels of 25 %, 50 % and 75 % and the <i>t_{resp}</i> for measurements in N ₂ are calculated for the first gas pulse.	96
6.5. Recovery times (<i>t_{recov}</i>) of H ₂ S and CO gas measurements in synthetic air (SA) and nitrogen (N ₂); <i>t_{recov}</i> for measurements in SA are mean values of the three relative humidity levels of 25 %, 50 % and 75 % and the <i>t_{recov}</i> for measurements in N ₂ are calculated for the second gas pulse.	96

Appendix

A. Selected area diffraction (SAED)

Selected Area Diffraction (SAED) pattern of tungsten oxide nanowires with the identified reflections forming rings (blue marked rings in figure A.1). Green-white dotted frame shows the area of the taken peak profile, which is evaluated in figures A.2 to A.7.

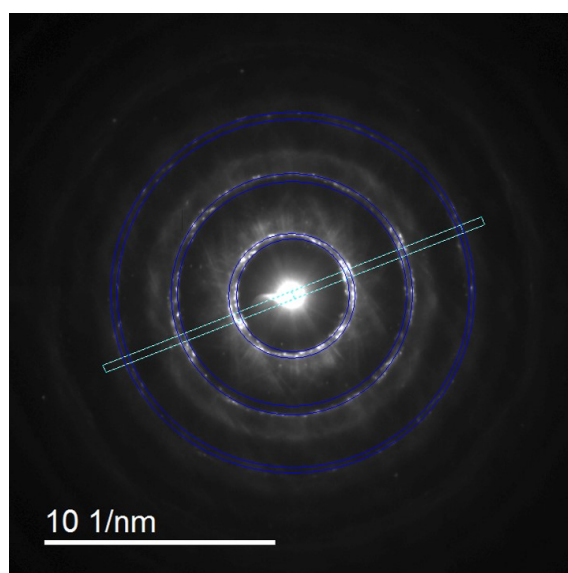


Figure A.1.: SAED pattern with six most intense reflection rings highlighted.

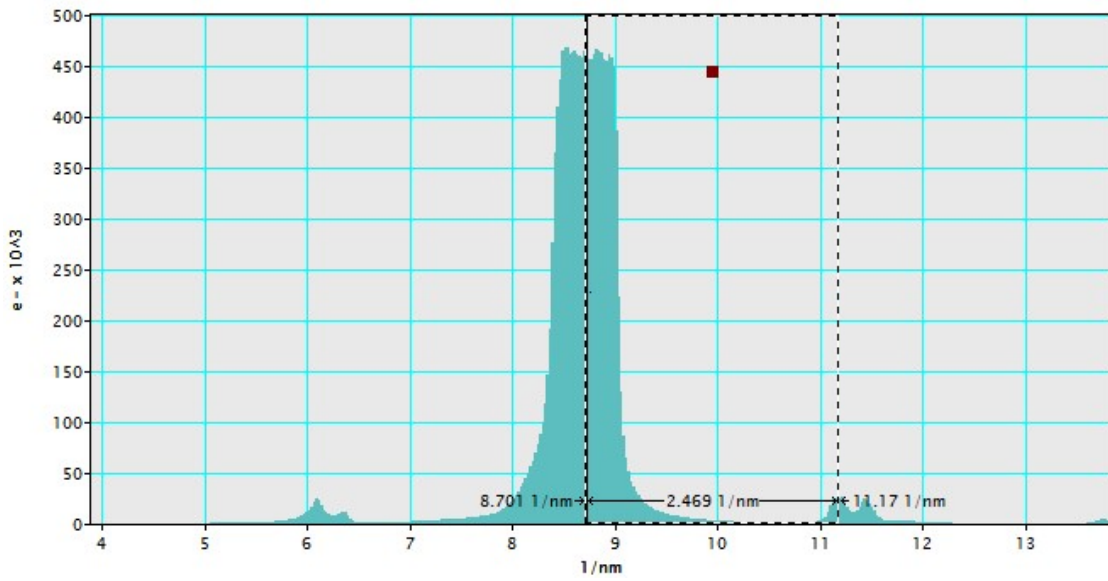


Figure A.2.: Profile of SAED pattern; peak at a distance of 2.469 (nm^{-1}).

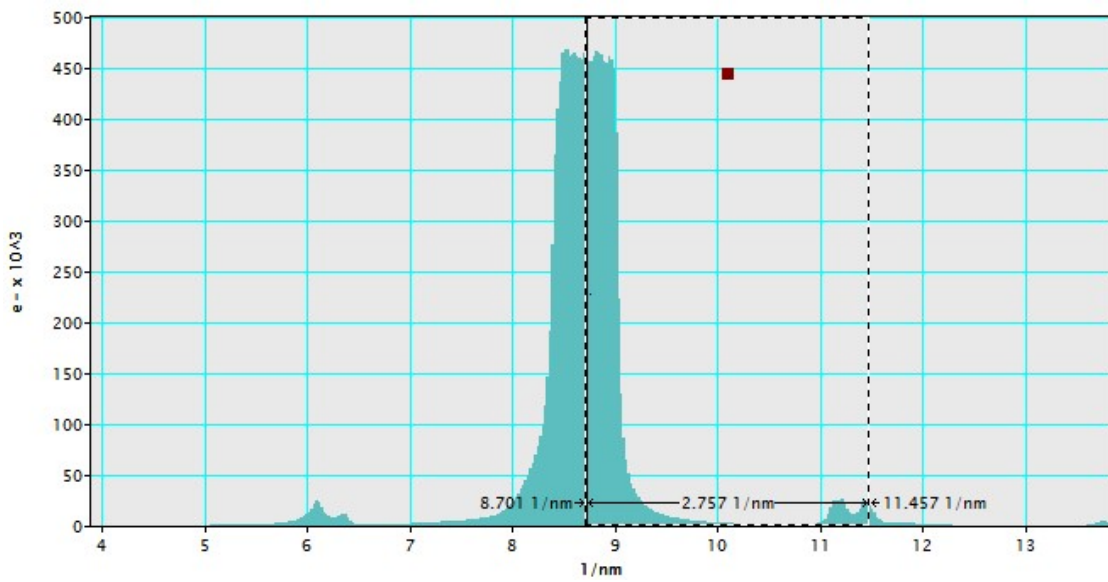


Figure A.3.: Profile of SAED pattern; peak at a distance of 2.757 (nm^{-1}).

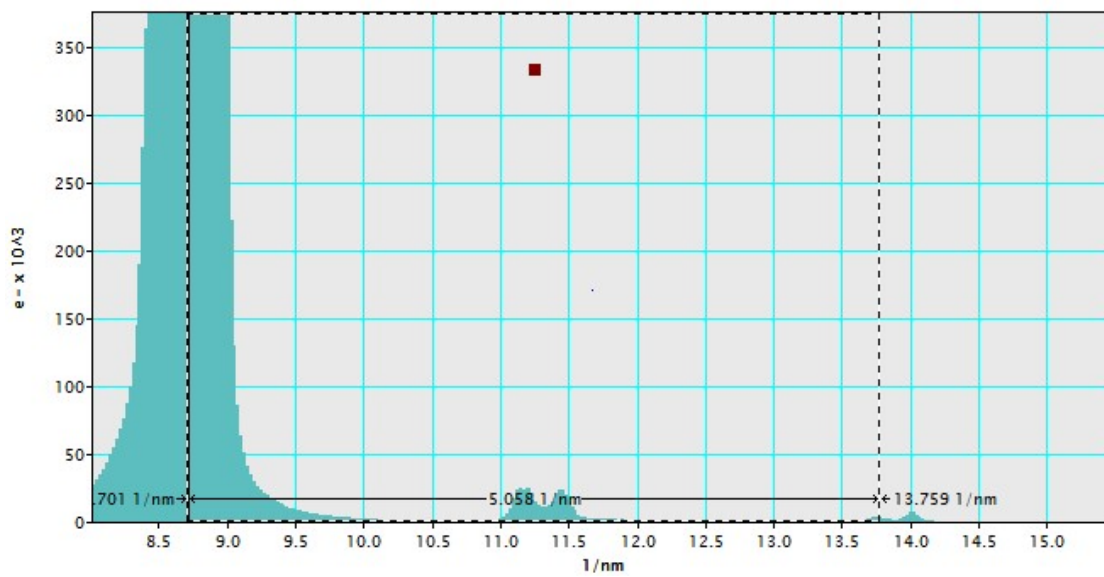


Figure A.4.: Profile of SAED pattern; peak at a distance of $5.058 \text{ (nm}^{-1}\text{)}$.

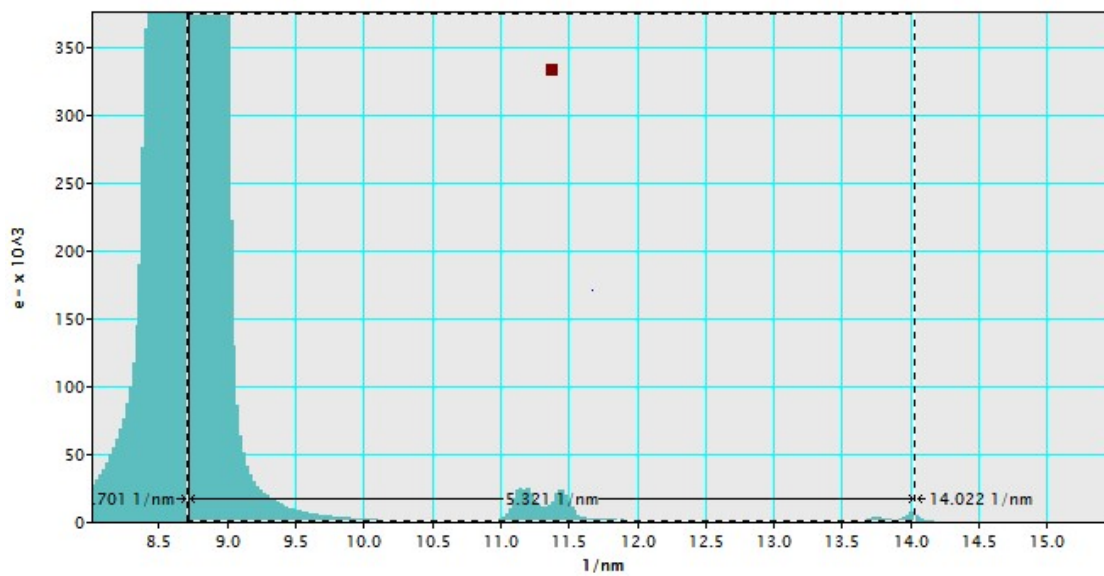


Figure A.5.: Profile of SAED pattern; peak at a distance of $5.321 \text{ (nm}^{-1}\text{)}$.

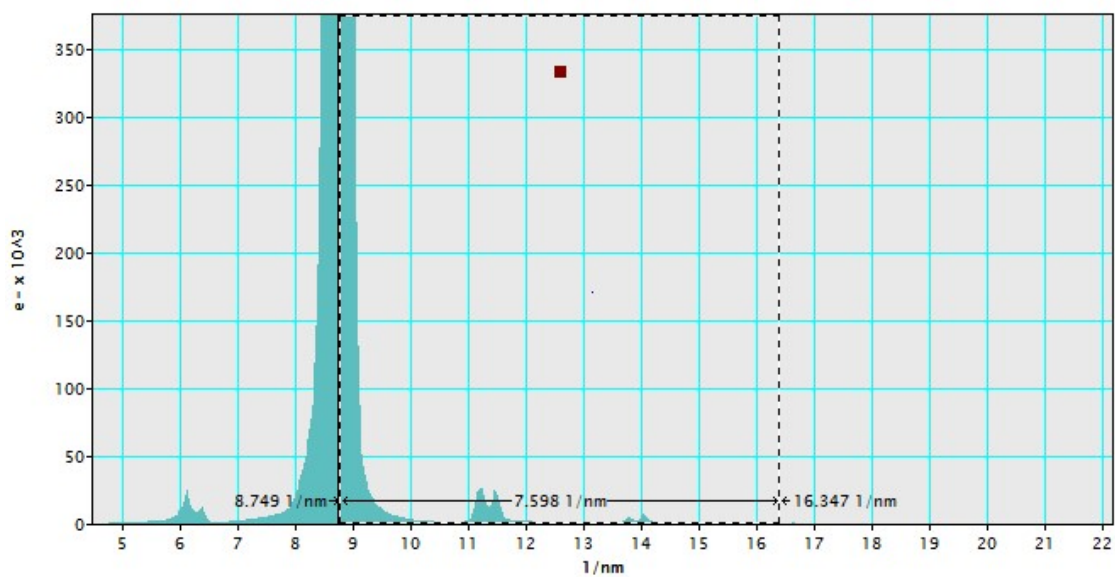


Figure A.6.: Profile of SAED pattern; peak at a distance of $7.598 (nm^{-1})$.

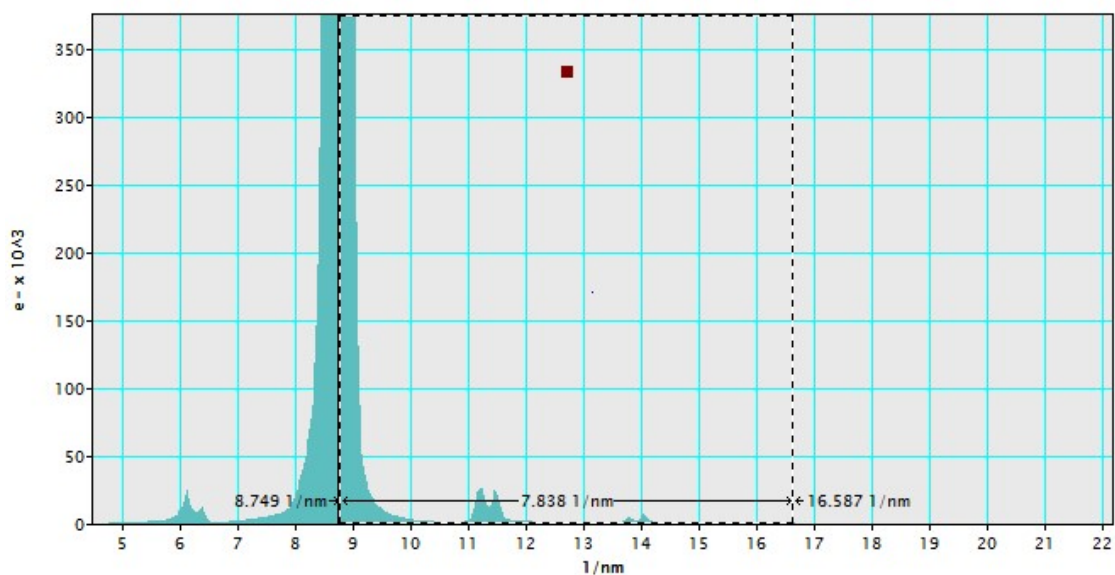


Figure A.7.: Profile of SAED pattern; peak at a distance of $7.838 (nm^{-1})$.

B. X-ray Diffraction (XRD)

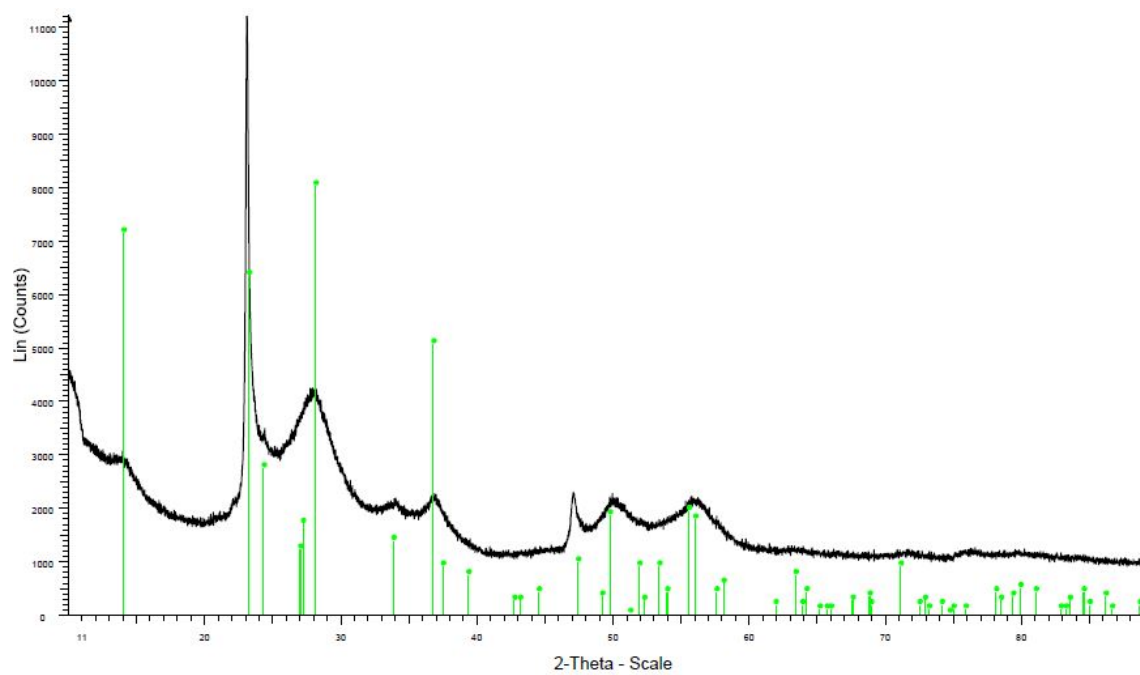


Figure B.1.: XRD spectrum with peak positions for hexagonal WO_3 [110] from ICSD database [111].

List of Publications

R. Wimmer-Teubenbacher, E. Lackner, J. Krainer, S. Steinhauer, A. Koeck. Gas Sensor Devices based on CuO- and ZnO-Nanowires directly synthesized on silicon substrate. *Proceedings of MRS Conference 2015. MRS Advances*, 1(13) : 817 – 823, 2016.

J. Krainer, M. Delcua, E. Lackner, R. Wimmer-Teubenbacher, F. Sosada, C. Gspan, K. Rohrer, E. Wachmann, A. Koeck. CMOS integrated tungsten oxide nanowire networks for ppb-level H₂S sensing. *Proceedings of 30th Eurosensors Conference, EUROSENSORS 2016. Procedia Engineering*, 168 : 272 – 275, 2016.

E. Lackner, J. Krainer, R. Wimmer-Teubenbacher, F. Sosada, C. Gspan, K. Rohrer, E. Wachmann, A. Koeck. CMOS nanocrystalline SnO₂ gas sensors for CO detection. *Proceedings of 30th Eurosensors Conference, EUROSENSORS 2016. Procedia Engineering*, 168 : 297 – 300, 2016.

J. Krainer, M. Delcua, E. Lackner, F. Sosada, R. Wimmer-Teubenbacher, C. Gspan, J. Bekacz, A. Poenninger, K. Rohrer, E. Wachmann, M. Schrems, A. Koeck. CMOS integrated tungsten oxide nanowire networks for ppb-level hydrogen sulfide sensing. *Proceedings of IEEE SENSORS 2016*. DOI:10.1109/ICSENS.2016.7808634
awarded with Student Best Paper Award

E. Lackner, J. Krainer, R. Wimmer-Teubenbacher, F. Sosada, M. Deluca, E. Laubender, O. Yurchenko, G. Urban, J. Bekacz, K. Rohrer, E. Wachmann, A. Koeck. CMOS integrated tin dioxide gas sensors functionalized with bimetallic nanoparticles for improved carbon monoxide detection. *Proceedings of IEEE SENSORS 2016*. DOI:10.1109/ICSENS.2016.7808667

S. Steinhauer, Z. Wang, Z. Zhou, J. Krainer, A. Köck, K. Nordlund, F. Djurabekova, P. Grammatikopoulos, M. Sowwan. Probing electron beam effects with chemoresistive nanosensors during in situ environmental transmission electron microscopy. *Applied Physics Letters*, 110 : 094103, 2017.

S. Steinhauer, J. Vernieres, J. Krainer, A. Köck, P. Grammatikopoulos, M. Sowwan. In situ chemoresistive sensing in the environmental TEM: probing functional devices and their nanoscale morphology. *Nanoscale*, 2017, DOI:10.1039/C6NR09322A.

Curriculum Vitae

Personal Data

Name Johanna Krainer
Date of birth February, 19th 1989
Place of birth Leoben, Austria

Education

05/2014-present Graz University of Technology
 PhD program / Doctoral School Chemistry
04/2011-04/2014 Graz University of Technology
 Master in Technical Chemistry
09/2007-04/2011 Graz University of Technology
 Bachelor in Chemistry

Career

05/2014-present MCL Materials Center Leoben Forschung GmbH
 Research fellow
08/2011-09/2011 AT&S Leoben-Hinterberg
 Proof-of-Concept- and Reliability Laboratory
04/2011-07/2011 Graz University of Technology and Siemens AG
 Project assistance
 "Research on isolation gases for interurban
 high-voltage power lines"